ISSN: 2376-2136 (Print)
ISSN: 2376-2144 (Online)

Trends in Renewable Energy

Volume 10, Issue 2, July 2024

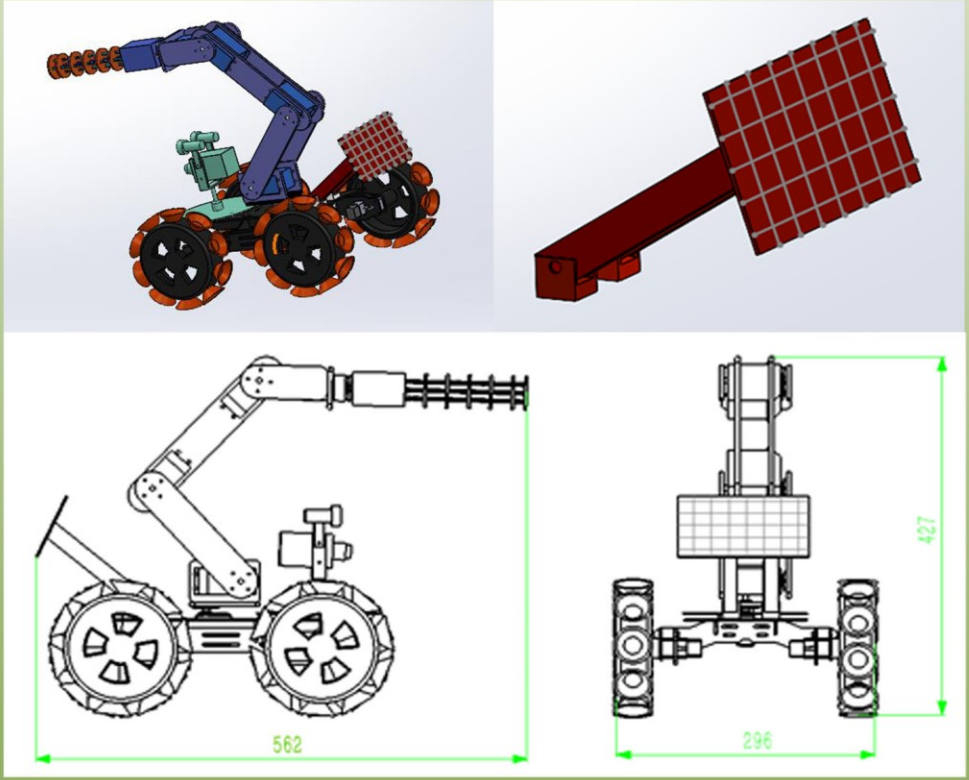

Cover image: Solar Central Air Conditioning Duct Cleaning Robot by Sun in this issue

futureenergysp.com
thefutureenergy.org

Trends in Renewable Energy

ISSN: 2376-2136 (Print) ISSN: 2376-2144 (Online)

http://futureenergysp.com/

Trends in Renewable Energy is an open accessed, peer-reviewed semi-annual journal publishing reviews and research papers in the field of renewable energy technology and science.

The aim of this journal is to provide a communication platform that is run exclusively by scientists working in the renewable energy field. Scope of the journal covers: Bioenergy, Biofuel, Biomass, Bioprocessing, Biorefinery, Biological waste treatment, Catalysis for energy generation, Energy conservation, Energy delivery, Energy resources, Energy storage, Energy transformation, Environmental impact, Feedstock utilization, Future energy development, Green chemistry, Green energy, Microbial products, Physico-chemical process for Biomass, Policy, Pollution, Renewable energy, Smart grid, Thermo-chemical processes for biomass, etc.

The Trends in Renewable Energy publishes the following article types: peer-reviewed reviews, mini-reviews, technical notes, short-form research papers, and original research papers.

The article processing charge (APC), also known as a publication fee, is fully waived for the Trends in Renewable Energy.

Editorial Team of Trends in Renewable Energy

EDITOR-IN-CHIEF

Dr. Bo Zhang	Editor, Trends in Renewable Energy, USA
Dr. Changyan Yang	Prof., School of Chemical Engineering & Pharmacy, Wuhan Institute of Technology, China

HONORARY CHAIRMEN

Dr. Yong Wang	Voiland Distinguished Professor, The Gene and Linda Voiland School of Chemical Engineering and Bioengineering, Washington State University, United States
Dr. Mahendra Singh Sodha	Professor, Lucknow University; Former Vice Chancellor of Devi Ahilya University, Lucknow University, and Barkatulla University; Professor/Dean/HOD/Deputy Director at IIT Delhi; Padma Shri Award; India
Dr. Elio Santacesaria	Professor of Industrial Chemistry, CEO of Eurochem Engineering srl, Italy

VICE CHAIRMEN

Dr. Mo Xian	Prof., Assistant Director, Qingdao Institute of BioEnergy and Bioprocess Technology, Chinese Academy of Sciences, China

EDITORS

Dr. Yiu Fai Tsang,	Associate Prof., Department of Science and Environmental Studies, The Education University of Hong Kong
Dr. Melanie Sattler	Dr. Syed Qasim Endowed Professor, Dept. of Civil Engineering, University of Texas at Arlington, United States
Dr. Attila Bai	Associate Prof., University of Debrecen, Hungary
Prof. Christophe Pierre Ménézo	University of Savoy Mont-Blanc, France
Dr. Moinuddin Sarker	MCIC, FICER, MInstP, MRSC, FARSS., VP of R & D, Head of Science/Technology Team, Natural State Research, Inc., United States
Dr. Suzana Yusup	Associate Prof., Biomass Processing Laboratory, Centre for Biofuel and Biochemical Research, Green Technology Mission Oriented Research, Universiti Teknologi PETRONAS, Malaysia
Dr. Zewei Miao	Global Technology Development, Monsanto Company, United States
Dr. Hui Wang	Pfizer Inc., United States
Dr. Shuangning Xiu	North Carolina Agricultural and Technical State University, United States
Dr. Junming XU	Associate Prof., Institute of Chemical Industry of Forest Products, China Academy of Forest, China
Dr. Hui Yang	Prof., College of Materials Science and Engineering, Nanjing Tech University, China
Dr. Ying Zhang	Associate Prof., School of Chemistry and Materials Science, University of Science and Technology of China, China
Dr. Ming-Jun Zhu	Prof., Assistant Dean, School of Bioscience & Bioengineering, South China University of Technology, China

EDITORIAL BOARD

Dr. Risahbh Dev Shukla	Dean and Associate Prof., Department of Electrical Engineering, Budge Budge Institute of Technology Kolkata, India
Dr. Neeraj Gupta	Indian Institute of Technology Roorkee, India
Dr. Elena Lucchi	Politecnico di Milano, Italy

Dr. Muhammad Mujtaba Asad	Faculty of Technical and Vocational Education, Universiti Tun Hussein Onn Malaysia, Malaysia
Dr. Afzal Sikander	Department of Instrumentation and Control Engineering, Dr. B. R. Ambedkar National Institute of Technology, India
Dr. Padmanabh Thakur	Professor and Head, Department of Electrical Engineering, Graphic Era University, India
Dr. K. DHAYALINI	Professor, Department of Electrical and Electronics Engineering, K. Ramakrishnan College of Engineering, Tamilnadu, India
Shangxian Xie	Texas A&M University, United States
Dr. Tanmoy Dutta	Sandia National Laboratories, United States
Dr. Efstathios Stefos	Pontifical Catholic University of Ecuador, Faculty of Exact and Natural Sciences, School of Physical Sciences and Mathematics, Ecuador
Dr. Xin Wang	Miami University, United States
Dr. Rami El-Emam	Assist. Prof., Faculty of Engineering, Mansoura University, Egypt
Dr. Rameshprabu Ramaraj	School of Renewable Energy, Maejo University, Thailand
Dr. ZAFER ÖMER ÖZDEMİR	Kirklareli University, Technology Faculty, Turkey
Dr. Vijay Yeul	Chandrapur Super Thermal Power Station, India
Dr. Mohanakrishna Gunda	VITO - Flemish Institute for Technological Research, Belgium
Dr. Shuai Tan	Georgia Institute of Technology, United States
Shahabaldin Rezania	Universiti Teknologi Malaysia (UTM), Malaysia
Dr. Madhu Sabnis	Contek Solutions LLC, Texas, United States
Dr. Qiangu Yan	Mississippi State University, United States
Dr. Mustafa Tolga BALTA	Associate Prof., Department of Mechanical Engineering, Faculty of Engineering, Aksaray University, Turkey
Dr. María González Alriols	Associate Prof., Chemical and Environmental Engineering Department, University of the Basque Country, Spain
Dr. Nattaporn Chaiyat	Assist. Prof., School of Renewable Energy, Maejo University, Thailand
Dr. Nguyen Duc Luong	Institute of Environmental Science and Engineering, National University of Civil Engineering, Vietnam
Mohd Lias Bin Kamal	Faculty of Applied Science, Universiti Teknologi MARA, Malaysia
Dr. N.L. Panwar	Assistant Prof., Department of Renewable Energy Engineering, College of Technology and Engineering, Maharana Pratap University of Agriculture and Technology, India
Dr. Caio Fortes	BASF, Brazil
Dr. Flavio Prattico	Department of Methods and Models for Economics, Territory and Finance, Sapienza University of Rome, Italy
Dr. Wennan ZHANG	Docent (Associate Prof.) and Senior Lecturer in Energy Engineering, Mid Sweden University, Sweden
Dr. Ing. Stamatis S. Kalligeros	Associate Prof., Hellenic Naval Academy, Greece
Carlos Rolz	Director of the Biochemical Engineering Center, Research Institute at Universidad del Valle, Guatemala
Ms. Lilias Makashini	Copperbelt University, Zambia
Dr. Ali Mostafaeipour	Associate Prof., Industrial Engineering Department, Yazd University, Iran
Dr. Camila da Silva	Prof., Maringá State University, Brazil
Dr. Anna Skorek-Osikowska	Silesian University of Technology, Poland
Dr. Shek Atiqure Rahman	Sustainable and Renewable Energy Engineering, College of Engineering, University of Sharjah, Bangladesh
Dr. Emad J Elnajjar	Associate Prof., Department of Mechanical Engineering, United Arab Emirates University, United Arab Emirates
Dr. Seyed Soheil Mousavi Ajarostaghi	Babol Noshirvani University of Technology, Babol, Iran
Dr. Dinesh K. Sharma	National Ecology and Environment Foundation, India
Dr. Lakshmana Kumar Ramasamy	Department of Corporate relations, Hindusthan College of Engineering and Technology, India
Dr. S. Venkata Ramana	SUSU/National Research University, Russian Federation
Dr. Priyanka Marathey	Department of Solar Energy, Pandit Deendayal Petroleum University, India
Osamah Siddiqui	University of Ontario Institute of Technology, Canada
Dr. Rupendra Kumar Pachauri	Assistant Prof., Electrical and Electronics Engineering Department, University

	of Petroleum and Energy Studies, India
Dr. Jun Mei	School of Chemistry and Physics, Science and Engineering Faculty, Queensland University of Technology, Australia
Dr. Valeria Di Sarli	Institute for Research on Combustion, National Research Council of Italy, Italy
Dr. Utkucan Şahin	Assistant Prof., Department of Energy Systems Engineering, Faculty of Technology, Muğla Sıtkı Koçman University, Turkey
Dr. ALIASHIM ALBANI	School of Ocean Engineering, Universiti Malaysia Terengganu, Malaysia
Dr. Ashwini Kumar	Assistant Prof., College of Engineering, HSBPVT's Parikrama Group of Institutions, India
Dr. Hasan AYDOGAN	Associate Prof., Mechanical Engineering Department, Selcuk University, Turkey
Dr. Jiekang Wu	Professor, School of Automation, Guangdong University of Technology, China
Dr. Ong Huei Ruey	DRB-HICOM University of Automotive, Malaysia
Dr. Miguel Ángel Reyes Belmonte	IMDEA Energy Institute, Spain
Dr. Chitra Venugopal	Associate Professor in Electrical Engineering, University of Trinidad and Tobago, Trinidad
Dr. Amit Kumar Singh	Assistant Prof., Instrumentation & Control Engineering Department, Dr. B.R.A. National Institute of Technology, India
Dr. Suvanjan Bhattacharyya	University of Pretoria, South Africa
Dr. Karunesh Tiwari	Babu Banarasi Das University, India
Dr. Sharadrao A. Vhanalkar	Karmaveer Hire Arts, Science, Commerce and Education College, India
Dr. Prasenjit Chatterjee	Assistant Prof. and Head, MCKV Institute of Engineering, India
Dr. S. Balamurugan	Mindnotix Technologies, India
Dr. Mohammad Nurunnabi	University of Oxford, United Kingdom
Dr. Kenneth Okedu	Caledonian College of Engineering, Oman
Dr. Cheng Zhang	Sr. Materials Engineer, Medtronic, Inc., United States
Dr. Chandani Sharma	Assistant Prof., Department of Electrical Engineering, Graphic Era University, India
Dr. Kashif Irshad	Assistant Prof., Mechanical Engineering Department, King Khalid University, Saudi Arabia
Dr. Abhijit Bhagavatula	Principal Lead Engineer, Southern Company Services, United States
Dr. S. Sathish	Associate Prof., Department of Mechanical Engineering, Hindustan University, India
Dr. Bindeshwar Singh	Assistant Prof., Kamla Nehru Institute of Technology, India
Dr. Yashar Hashemi	Tehran Regional Electric Company, Iran
Dr. Navanietha Krishnaraj R	South Dakota School of Mines and Technology, United States
Dr. SANDEEP GUPTA	JECRC University, India
Dr. Shwetank Avikal	Graphic Era Hill University, India
Dr. Xianglin Zhai	Poochon Scientific LLC, United States
Dr. Rui Li	Associate Prof., College of Engineering, China Agricultural University, China
Dr. Adam Elhag Ahmed	National Nutrition Policy Chair, Department of Community Services, College of Applied Medical Sciences, King Saud University, Saudi Arabia
Dr. Jingbo Li	Massachusetts Institute of Technology, United States
Dr. Srikanth Mutnuri	Associate Prof., Department of Biological Sciences, Associate Dean for International Programmes and Collaboration, Birla Institute of Technology & Science, India
Dr. Bashar Malkawi	Global Professor of Practice in Law, James E. Rogers College of Law, University of Arizona, United States
Dr. Simona Silvia Merola	Istituto Motori - National Research Council of Naples, Italy
Dr. Hakan Caliskan	Faculty of Engineering, Department of Mechanical Engineering, Usak University, Turkey
Dr. Umashankar Subramaniam	Associate Prof., College of Engineering, Prince Sultan University, Saudi Arabia
Dr. Tayfun GÜNDOĞDU	Faculty of Electrical and Electronic Engineering, Department of Electrical Engineering, Istanbul Technical University, Turkey
Dr. Yukesh Kannah R	Department of Civil Engineering, Anna University Regional Campus, India
Jean Bosco Mugiraneza	University of Rwanda, Rwanda
Dr. R. Parameshwaran	Assistant Prof., Dept. of Mechanical Engineering, Birla Institute of Technology

Table of Contents

Volume 10, Issue 2, July 2024

Trends in Renewable Energy
OPEN ACCESS ISSN: 2376-2144
Peer-Reviewed Article futureenergysp.com/index.php/tre

Evaluation of PV-based Buck-Boost and SEPIC Converters for EV Charging Applications

Jagadeesh K,* Ch. Chengaiah

Department of Electrical and Electronics Engineering, S.V.U College of Engineering, Sri Venkateswara University, Tirupati, Andhra Pradesh – 517 502, India.

Received January 9, 2024; Accepted March 3, 2024; Published March 14, 2024

In recent decades, environmental issues have become an area of greatest concern due to changes in global climate conditions. The transportation sector is a major contributor to carbon dioxide emissions, accounting for more than 22.9% of total carbon dioxide emissions. At present, most vehicles run on gasoline/diesel as fuel which is unsustainable and unviable as fossil fuels produce carbon emissions and fuel costs are rising. To address these issues, electric vehicles (EVs) offer an attractive solution as alternative to internal combustion engine vehicles that use electricity as an energy source. It is logical to use renewable energy to charge vehicles, which makes renewable energy an end-to-end clean energy source. In electric vehicles, energy conversion plays an important role. In the energy conversion process, alternating current (AC) can be converted to direct current (DC), or direct current can be converted to alternating current. In EV fast charging applications, DC-to-DC conversion is used, which requires DC-to-DC converters. In this paper, a detailed evaluation of the Buck-Boost and Single-Ended Primary Inductance Converters (SEPIC) with PV as input is analyzed for EV charging applications to make it end-to-end clean energy. For this purpose, a 5-by-5 PV system with a Buck-Boost, SEPIC converters with particle swarm optimization technique is considered, which is simulated in a MATLAB/SIMULINK environment. The simulation results showed that the ripples in output are minimal in SEPIC which supports the smooth and efficient charging of EV battery.

Keywords: Solar PV system; DC-DC converters; Particle Swarm Optimization (PSO); Electrical Vehicles; Optimization

Introduction

Power electronic converters play a vital in photovoltaic (PV) applications by aiding efficient conversion, control, and management of the electrical energy produced by solar panels [1, 2]. Solar modules generate different voltage and current levels depending on environmental conditions such as sunlight and temperature. Solar module power is typically in the form of direct current (DC) at low voltage levels [3]. Grid-connected inverters, or power electronic converters, convert the direct current generated by the solar modules into grid-compatible alternating current (AC) [4]. These inverters also provide synchronization, voltage regulation, and control functions to ensure safe and reliable integration of photovoltaic systems into the grid. Power electronic converters in

---

*Corresponding author: svujagadeeshk@gmail.com

Tr Ren Energy, 2024, Vol.10, No.2, 159-169. doi: 10.17737/tre.2024.10.2.00168

grid-connected PV systems can also provide reactive power control. By controlling the inverter power, you can regulate the flow of reactive power into and out of the grid [5]. Power electronic converters play a key role in photovoltaic systems that are integrated with energy storage systems such as batteries [6]. These converters allow efficient charging and discharging of batteries, voltage regulation, and synchronization with the grid [7]. Overall, power electronic converters play a critical role in PV applications by optimizing power generation, enabling grid integration, facilitating energy storage, and ensuring system protection and security [8].

Operation of Buck-Boost Converter

Buck – Boost converter is a combination of both buck and boost converters. The advantages of both buck and boost converters are embedded in the buck-boost converter. The advantage of using a buck/boost converter is that it can step up or down the input voltage, making it suitable for a wide range of applications. The buck-boost converter provides lower duty cycles and higher efficiency over a wide range of input and output voltages. Buck-boost converters are widely used in a variety of applications including battery-powered devices to extend battery life. These are also suitable for solar power systems to regulate voltage levels and maximize power output. Buck-boost converters are used in LED lighting systems to regulate voltage levels and maintain constant current. This converter can be used in applications where constant voltage is required.

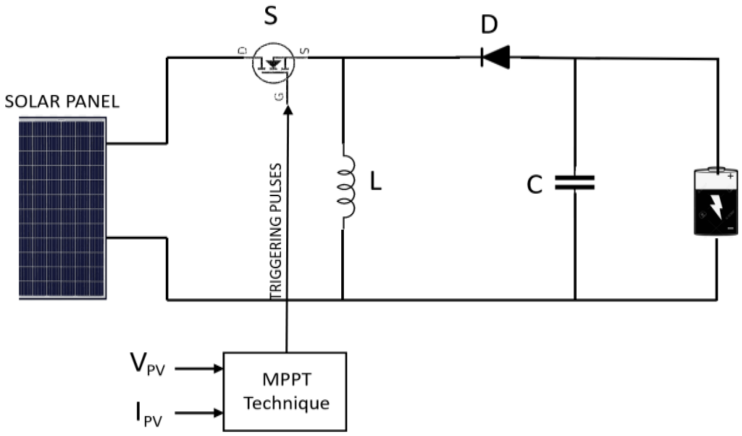

Figure 1. Basic circuit diagram of Buck-Boost converter

When the switch (MOSFET) is turned on, the power supply current begins to flow through the switch, through the inductor, and back to the power supply as shown in Fig. 1.

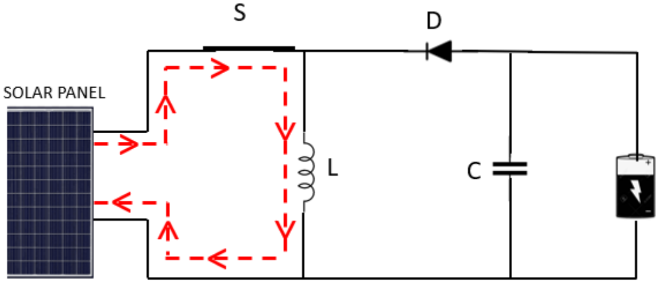

Figure 2. Mode 1 operation of Buck-Boost converter

The diode (D) is reverse-biased and acts as an open switch, isolating the load from the supply current. When the power supply energizes the inductor, the inductor starts charging with the polarity shown in Fig. 2.

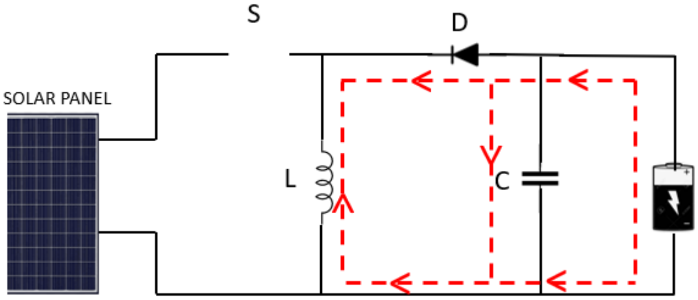

Figure 3. Mode 2 operation of Buck-Boost converter

When the switch is off, the reduction in inductor current creates a negative voltage across the inductor. The current that flowed through the switch and inductor in the previous interval flows through the inductor, capacitor, load, diode, and back to the inductor, as shown in Fig. 3. The inductor continues to discharge and the inductor current decreases until the MOSFET turns on again in the next cycle.

$$V_o = \frac{D}{1-D} V_i \tag{1}$$

Therefore, from the above equation (1), the output voltage depends on the duty cycle. If the duty cycle (D) is greater than 0.5, the circuit operates as a boost converter or boost DC converter.

Operation of SEPIC Converter

SEPIC is abbreviated as a single-ended primary inductance converter. It is a type of DC-DC converter that enables a DC voltage range on the input side and provides a stable voltage on the output side. This type of converter is very similar to buck-boost converters and Cuk converters which provide an output voltage greater than, less than, or equal to the input voltage.

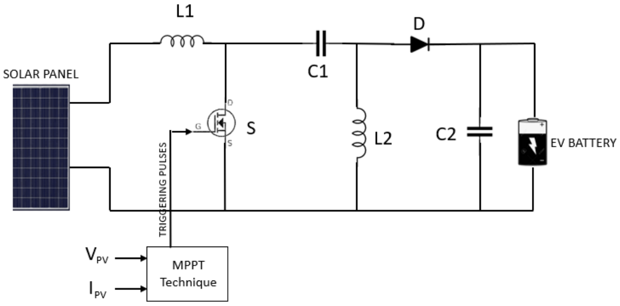

Figure 4. Basic circuit diagram of SEPIC converter

The basic circuit diagram consists of a Switch "S", two inductors (L_1, L_2), two capacitors (C_1, C_2), and one Diode. A switch is a semiconductor device, in the SEPIC converter generally a transistor (MOSFET, IGBT, or BJT) is used as shown in Fig. 4.

MOSFETs are preferred over IGBTs and BJTs in most DC/DC converters because of their high input impedance and low voltage drop.

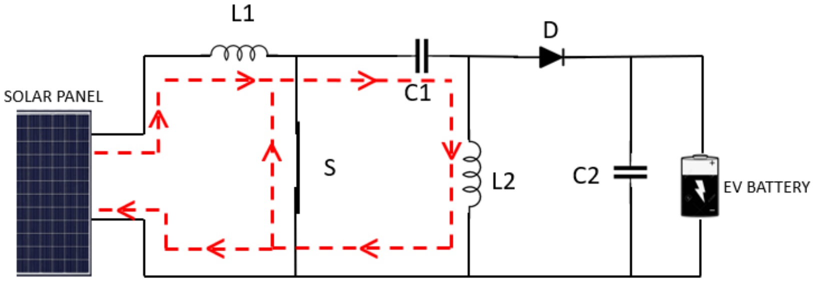

Figure 5. Mode 1 operation of SEPIC Converter

Initially the switch "S" is closed and the current from the source will pass through the switch, inductor L_1, and back to the source as shown in Fig. 5. This will cause an increase in the inductor's current, I_{L1}, which will start charging from the input source. During this charging process, the inductor's instantaneous voltage, V, will be approximately equal to the source voltage, V. Moreover, when the Switch "S" is on, the energy released by capacitor C1 will charge the inductor L_2. Through the Switch "S", the capacitor C_1 will release its energy to the inductor L_2.

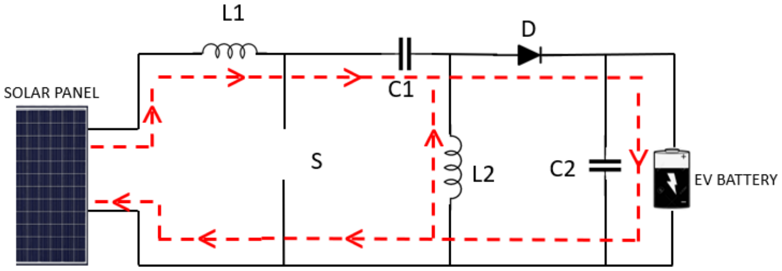

Figure 6. Mode 2 operation of SEPIC Converter

After the Switch "S" is turned off, the inductor L_1 reverses polarity and discharges to capacitor C_1. The charged inductor L_2 then discharges, forward-biasing the diode and transferring energy to the load as shown in Fig. 6. When the Switch "S" is turned on again, the cycle repeats.

The switching or triggering pulses for the switches are given through the particle swarm optimization algorithm. Population-based stochastic optimization (PSO) is a technique introduced by James Kennedy and Russell C [9]. PSO-based tracking systems do not require differential calculations, have a small number of tuning parameters, are system-independent, and have a high probability of finding an overall optimal solution with high computational efficiency [10]. The particles are randomly initialized and start to move in a given search space with a certain velocity. Then, for each iteration, a new velocity value is calculated based on the current velocity, the previous best position and the global best position. During this optimization process, the agents are spread over the search space in different directions.

$$v_i^{k+1} = wv_i^k + c_1 r_1 \left\{ P_{\text{best}\,i} - x_i^k \right\} + c_2 r_2 \left\{ G_{\text{best}} - x_i^k \right\} \tag{2}$$

and the position of i^{th} particle X_i is adjusted using the below equation.

$$x_i^{k+1} = x_i^k + v_i^{k+1} \tag{3}$$

Here, w is the inertia weight, c_1 and c_2 are the acceleration coefficients, r_1 and r_2 are random numbers in the range (0 –1), P_{besti} is the personal best position of particle i, and G_{best} is the best position of the particles. Equations 2 and 3 are called flight equations and show that the new position of each particle is affected by three terms. The first term, inertia weight ω, is the current velocity of the particle. The second term, weighted by cognitive acceleration coefficient c_1, prompts the attraction of the particle toward its own personal best (cognition influence), and the third term, weighted by social acceleration coefficient c_2, prompts the attraction of the particle toward the global best (social influence). The personal best position P_{besti} is updated using Equation 4 if the condition in Equation 5 is satisfied, that is,

$$P_{\text{best}_i} = x_i^k, \tag{4}$$

$$f(x_i^k) > f(P_{\text{best}_i}) \tag{5}$$

where f is the objective function

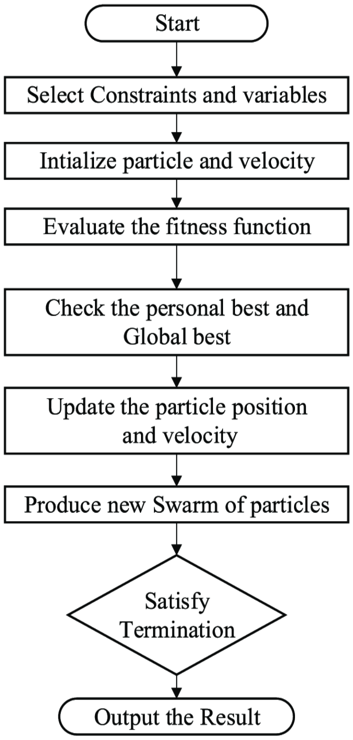

Figure 7. Flowchart of PSO method

Design of Buck-Boost and SEPIC Converters:

The operation of Buck-Boost and SEPIC are discussed in the previous section and the circuit diagram is simulated in MATLAB/Simulink environment with renewable energy as input in this case solar power as input. The triggering pulses are given to the switch by using the particle swarm optimization technique. Here a 5 by 5 PV system and the output of the PV system are connected to both the converter and the simulation diagrams are shown in Fig. 8 and 9. The output of the converters are connected to the EV battery. The simulation diagram is shown in Fig. 8.

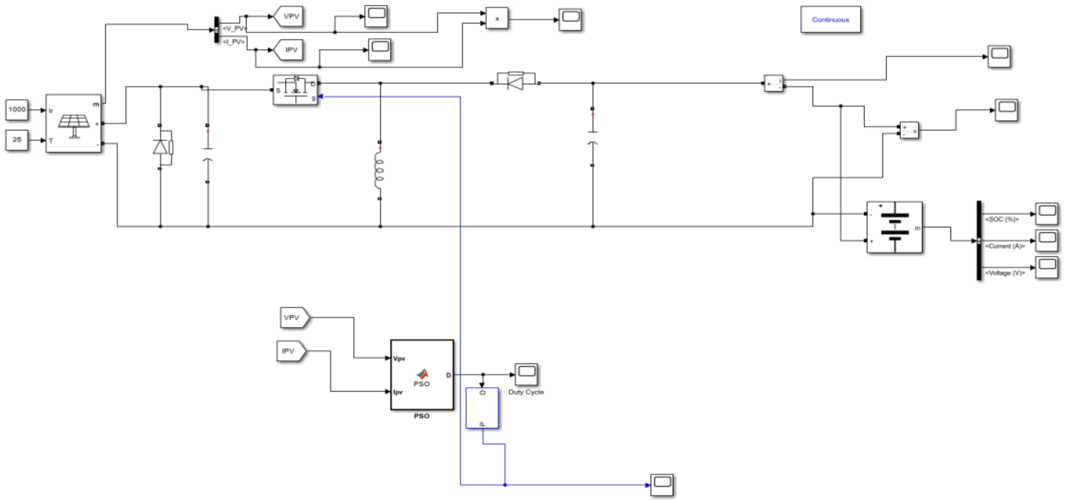

Figure 8. Simulink model of PV based Buck Boost converter

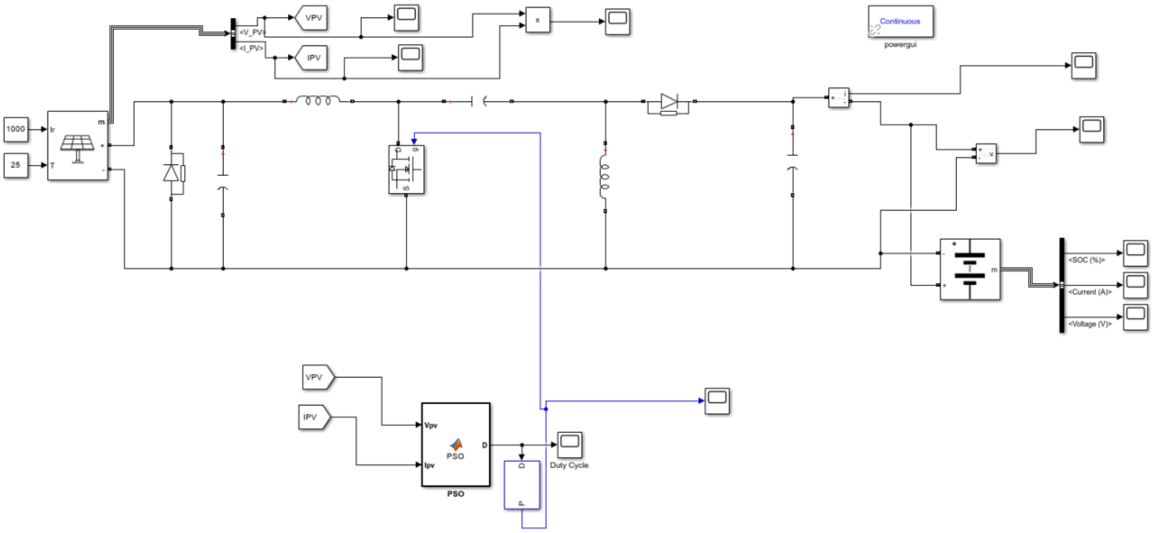

Figure 9. Simulink model of PV based SEPIC converter

The simulation parameters considered and the characteristics of the PV system are shown in Fig. 8.

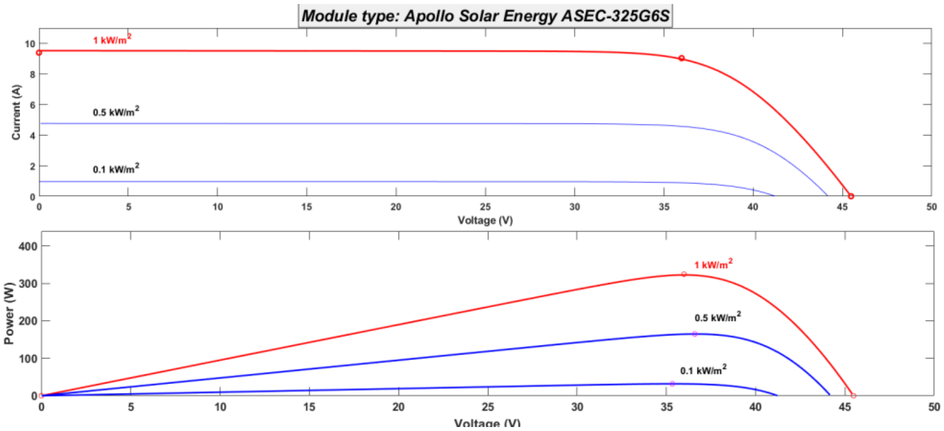

Figure 10. PV and IV characteristics of solar PV panel

and Buck-boost and SEPIC converter parameters are shown in Table 1.

Table 1. Parameter Specifications

Parameter	BUCK – BOOST	SEPIC
	Values	Values
L1	9.77mH	34.7μH
L2	-	41.04μH
C1	44.045μF	10.55μF
C2	-	44.453μF
Battery voltage	48 V	48 V
Battery SOC	50%	50%
Switching Frequency	10kHz	10kHz

The triggering pulses for buck-boost and SEPIC converters are shown in Fig.9.

Results and Discussion

Figure 11. Triggering pulses to the Buck-Boost converter

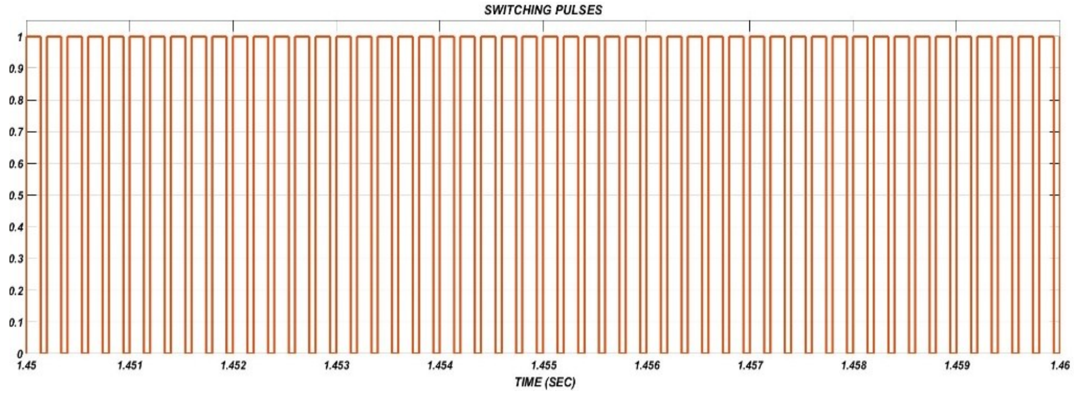

Figure 12. Triggering pulses to the SEPIC Converter

Figures 9 and 10 are the switching pulses given to the Switch ‘S’. The switching pulses are generated by using the particle swarm optimization algorithm shown in Fig. 7. The switching frequency considered for calculation is 10 kHz.

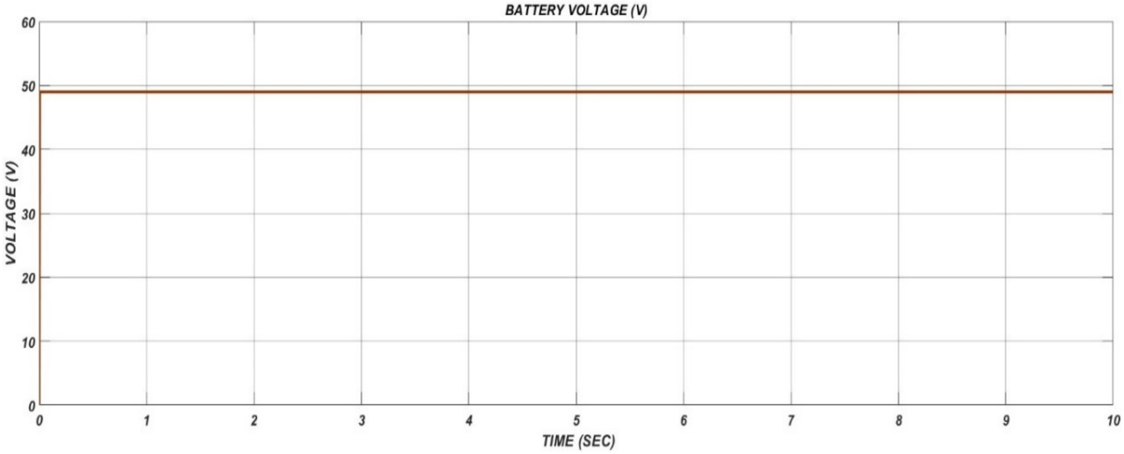

Figure 13. Battery Voltage of Buck Boost Converter

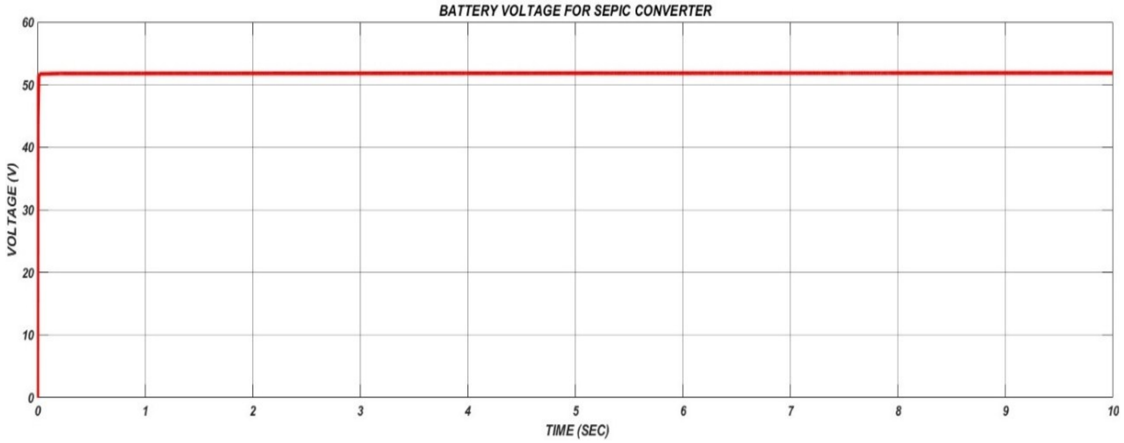

Figure 14. Battery Voltage of SEPIC Converter

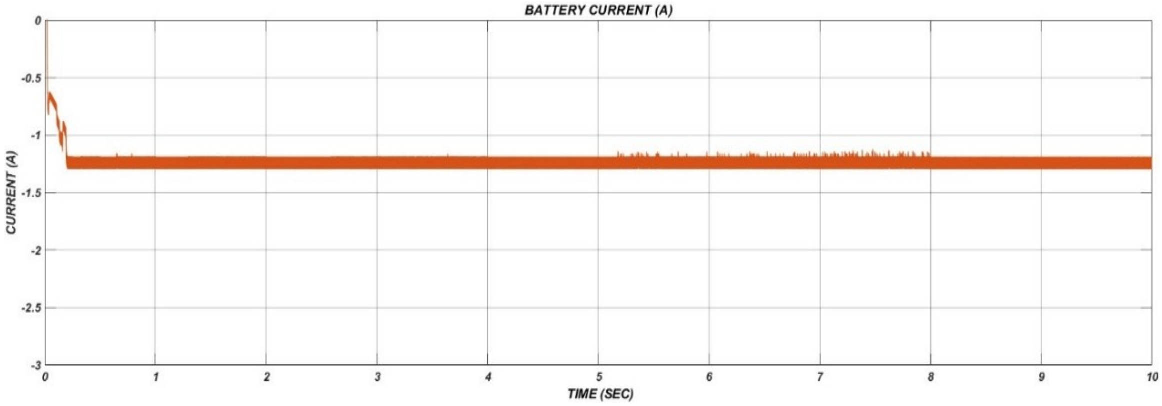

Figure 15. Battery Current in Buck Boost Converter

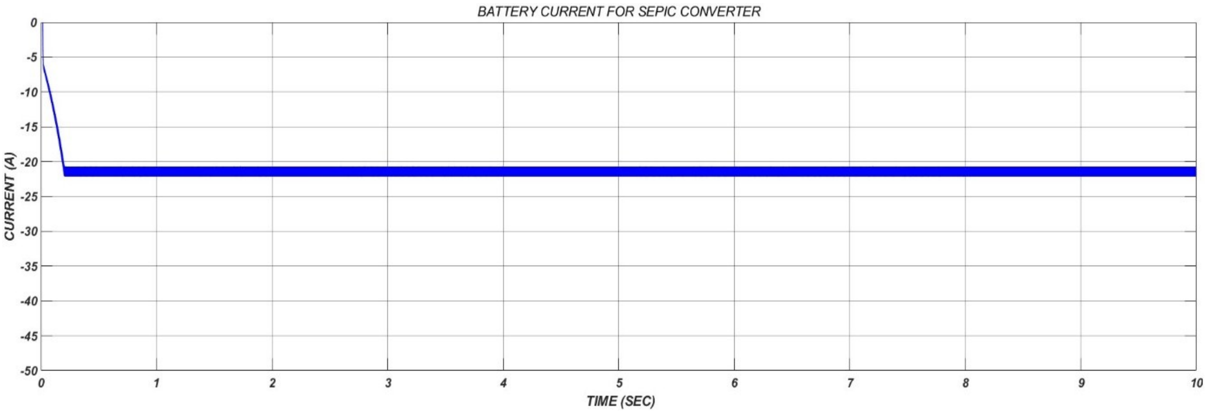

Figure 16. Battery Current in SEPIC Converter

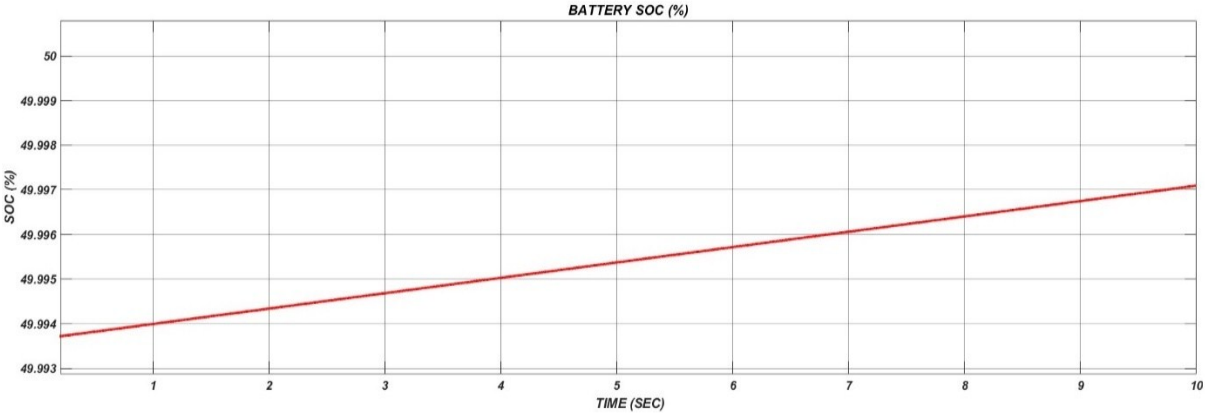

Figure 17. Battery state of charge (SOC) in Buck Boost Converter

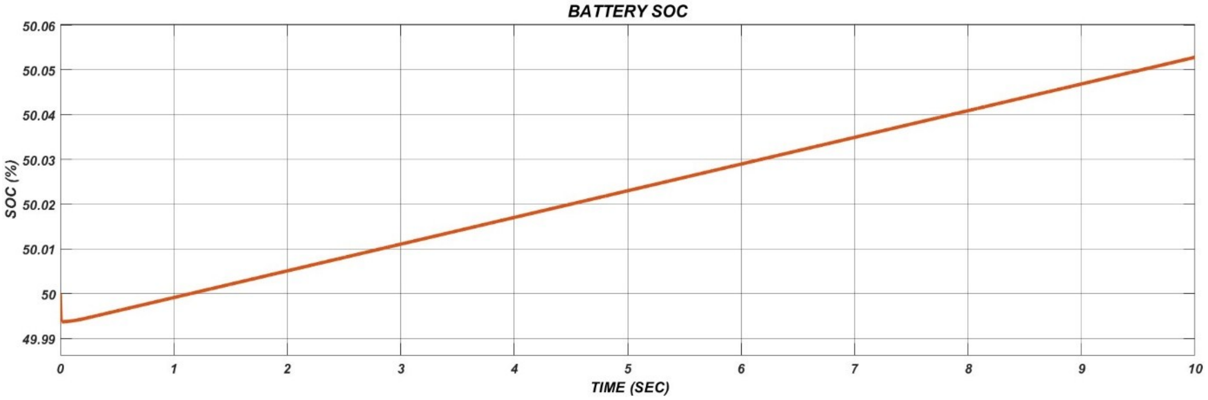

Figure 18. Battery state of charge (SOC) in SEPIC Converter

Figs. 11, 13, 15, and 17 show the battery voltage, current, and state of charge (SOC) for the buck-boost converter, while Figs. 12, 14, 16, and 18 show the same for the SEPIC converter.

Table 1. Performance Parameter

PARAMETER	Buck - Boost	SEPIC
Output Voltage (V)	48V	51V
Charging Current (A)	-1.25A	-23A
State of Charge (SOC) (%)	49.997%	50.057%

From Table 2, although the battery voltage is almost the same for both converters, the current delivered by the converters is different. The SEPIC converter delivers -23 amps of current for charging the battery, while the buck-boost converter delivers -1.35 amps. During charging, the battery draws current from the source, so the battery current is negative. The SOC of the battery gradually increases in both cases, but the charging time taken for the SEPIC converter to charge fully is approximately 8 Hrs, and for the buck-boost converter is approximately 6 Hrs. This shows that the charging is faster in the case of the SEPIC converter compared to the buck-boost converter. Based on the tabulated results, the SEPIC converter produces more current with solar power as input and is more efficient in charging the EV battery.

CONCLUSIONS

A PV-based charging mechanism for an EV using a Buck-Boost and SEPIC converters with PSO MPPT is simulated in MATLAB/ SIMULINK environment and the results are studied. From the simulation results, it is observed that SEPIC provides more current and more State of Charge (SOC) of the EV battery compared to Buck Boost. Charging time is approximately 6 hours for a SEPIC converter and approximately 8 hours for a buck-boost converter. This shows that the SEPIC converter charges faster compared to the buck-boost converter. Therefore, the SEPIC converter with solar power as input is more efficient in charging the EV battery when compared to Buck-Boost. This charging system uses solar power to charge EV batteries which makes it an end-to-end clean energy.

CONFLICTS OF INTEREST

The authors declare that there is no conflict of interests regarding the publication of this paper.

REFERENCES

[1] Suryoatmojo, H., Dilianto, I., Suwito, Mardiyanto, R., Setijadi, E., & Riawan, D. C. (2018, 11-12 May 2018). *Design and analysis of high gain modified SEPIC converter for photovoltaic applications.* Paper presented at the 2018 IEEE International Conference on Innovative Research and Development (ICIRD), pp. 1-6. doi: https://doi.org/10.1109/ICIRD.2018.8376319

[2] Azer, P., & Emadi, A. (2020). Generalized State Space Average Model for Multi-Phase Interleaved Buck, Boost and Buck-Boost DC-DC Converters: Transient, Steady-State and Switching Dynamics. *IEEE Access, 8*, 77735-77745. doi: https://doi.org/10.1109/ACCESS.2020.2987277

[3] Reddy, B. V., & Chengaiah, C. (2023, 22-24 Feb. 2023). *A Modified P&O Technique for Solar based EV Charging with SEPIC.* Paper presented at the 2023 Fifth International Conference on Electrical, Computer and Communication Technologies (ICECCT), pp. 1-4. doi: https://doi.org/10.1109/ICECCT56650.2023.10179607.

[4] Kanhav, K. A., & Chaudhari, M. A. (2017). *A bidirectional multiport dc-dc converter topology for hybrid energy system.* Paper presented at the 2017 International Conference on Energy, Communication, Data Analytics and Soft Computing (ICECDS), pp. 3427-3432. doi: https://doi.org/10.1109/ICECDS.2017.8390097.

[5] Jagadeesh, K., & Chengaiah, C. (2022). A comprehensive review-Partial shading issues in PV system. In *AIP Conference Proceedings* (Vol. 2640, No. 1). AIP Publishing. doi: https://doi.org/10.1063/5.0112913

[6] Soedibyo, Amri, B., & Ashari, M. (2015). *The comparative study of Buck-boost, Cuk, Sepic and Zeta converters for maximum power point tracking photovoltaic using P&O method.* Paper presented at the 2015 2nd International Conference on Information Technology, Computer, and Electrical Engineering (ICITACEE), pp. 327-332, doi: https://doi.org/10.1109/ICITACEE.2015.7437823

[7] Mitra, A., Bhowmik, S., Mukherjee, S., Dutta, P., Banerjee, K., & Sarkar, S. (2022). *Performance Comparison and Design of Passive Components for DC-DC Buck-Boost, Cuk and Sepic Converter.* Paper presented at the 2022 IEEE International Conference of Electron Devices Society Kolkata Chapter (EDKCON), pp. 12-17, doi: https://doi.org/10.1109/EDKCON56221.2022.10032936

[8] Kamalesh, M. S., Senthilnathan, N., Bharatiraja, C., Kumar, C., & Deepika, L. (2021). *Analysis of Ripples in SEPIC based Buck-Boost Converter for Low Power Applications.* Paper presented at the 2021 IEEE Madras Section Conference (MASCON), pp. 1-7, doi: https://doi.org/10.1109/MASCON51689.2021.9563360

[9] Hayder, W., Abid, A., Hamed, M. B., Ogliari, E., & Sbita, L. (2021). *Comparison of MPPT methods FLC & PSO for PV system under variable irradiance and temperature.* Paper presented at the 2021 18th International Multi-Conference on Systems, Signals & Devices (SSD), pp. 1247-1251, doi: https://doi.org/10.1109/SSD52085.2021.9429346

[10] Khairi, M. N. S., Bakhari, N. A. B., Samat, A. A. A., Kamarudin, N., Hussin, M. H. M., & Tajudin, A. I. (2023). *MPPT Design Using PSO Technique for Photovoltaic System.* Paper presented at the 2023 IEEE 3rd International Conference in Power Engineering Applications (ICPEA), pp. 131-136, doi: https://doi.org/10.1109/ICPEA56918.2023.10093161

Trends in Renewable Energy
OPEN ACCESS ISSN:2376-2144
Peer-Reviewed Article futureenergysp.com/index.php/tre

Trend and Variations of Surface Air Temperatures across Selected Eco-Climatic Zones in Nigeria

L.E. King,[1,*] S.O. Udo,[1] I.O. Ewona,[2] S.O. Amadi,[3] E.B. Ebong,[1] C.N. Emeka[4] and M.D. Umoh[5]

1: Dept. of Physics, Faculty of Physical Sciences, University of Calabar, Nigeria
2: Dept. of Physics, Faculty of Physical Sciences, Cross River State University of Science and Technology, Calabar, Nigeria
3:Dept. of Physics, Faculty of Physical Sciences, Alex Ekwueme Federal University, Ndufu -Alike Ikwu, Nigeria
4: Dept. of Geology, Faculty of Physical Sciences, University of Calabar, Nigeria
5: Dept. Of Research and Strategic Planning, Maritime Academy of Nigeria, Oron, Nigeria

Received April 23, 2024; Accepted May 9, 2024; Published May 29, 2024

The trends and variability in surface air temperatures over selected eco-climatic zones in Nigeria were assessed using Merra-2 datasets from 1981 to 2018. A total of 15 stations spread across the eco-climatic zones in Nigeria were used for this study. The Mann-Kendall, linear trend and Sen's slope trend test, time series plots and descriptive statistics were used. The coefficient of variation of the surface air maximum temperature showed a low variability for the Mangrove-swamp rainforest and a moderate variability for the Guinea-wooded, Sudan and Sahel savannas. Similarly, the coefficient of variation of the surface air minimum temperature showed a moderate variation for all the selected eco-climatic zones. The M-K trend test showed that 14 stations showed an upward trend, 1 station showed a downward trend, and the trends of the maximum atmospheric surface temperature at 13 stations were statistically significant. The minimum surface air temperature at all stations showed a clear upward trend. The maximum and minimum surface air temperatures are estimated to increase by about 0.035°C and 0.036°C per year on average, respectively. For Nigeria, the estimated average surface air temperature increase is about 0.036°C per year, while the average surface temperature over 38 years is estimated to have increased by about 1.4°C. This study gave a linear trend projection of an expected increase in the mean surface air temperature of about 4.3°C in Nigeria by 2100.

Keywords: Trend; Maximum temperature; Minimum temperature; Radiative forcing; Nigeria

Introduction

Surface air temperature is essentially an invaluable weather and climate element and an important indicator of climate change and variability. Assessing its character is very paramount towards having a clear insight about climate change and variability, which may be different at local, regional and global scales. The Inter-Governmental Panel on Climate Change report [1] and Malhi & Wright [2] have pointed out that worldwide, the earth's global atmosphere is experiencing a swift and human-driven change, with no previous antecedent in both its absolute potential magnitude and change

**Corresponding author:* lewisking72@yahoo.com,lewisking659@gmail.com

Tr Ren Energy, 2024, Vol.10, No.2, 170-209. doi: 10.17737/tre.2024.10.2.00172

rate. Globally, the mean surface air temperature has increased by about 0.74°C and anticipated increase is projected to range between 1.6°C and 4.5°C by 2100 with its change rate being considerably different amongst regions [3].

In the last few decades, climate change has been adjudged as perhaps, a serious debilitating and unending environmental concern to the global community, especially in low- and medium-income nations of the world, where majority of their economic activities are seriously vulnerable to climate change. Rising ambient surface air temperatures has triggered off an increased frequency, intensity and duration of heat-related events, including heat waves in quite a number of regions. The rate and intensity of droughts have increased in some regions, and the intensity of heavy precipitation events has increased globally [4]. In recent decades, the global surface temperature rise has been very common, and the temperature rise in the high latitudes of the Northern Hemisphere has been more obvious. Heterogeneous land surface types and surface albedo, changing evapotranspiration rates, and carbon cycle influence climate in diverse ways and have been suggested to be culpable for the variations in the spatial distribution of surface air temperature [5-7].

The global energy budget of the earth is being influenced by variations in some factors, including but not limited to the concentrations of greenhouse gases (GHG's) and atmospheric aerosols, as well as by land surface properties changes. Radiative forcing expresses these changes as a pointer to the impact that a factor wields in changing the net balance of radiative flux between the down welling solar and the upwelling thermal infrared radiation from the earth's surface and lower atmosphere [3]. A radiative forcing of +2.30 W/m^2 has been pointed out to be due to the combined increases in carbon IV oxide, methane, and nitrous oxide, a radiative forcing of about –0.5W/m^2 due to atmospheric aerosols and a forcing of –0.7 W/m^2 due to indirect cloud albedo. A radiative forcing of about +0.35 W/m^2, +0.34 W/m^2, -0.2 and +0.1 W/m^2,+0.12 W/m^2 are due to changes in atmospheric concentrations of tropospheric ozone and halocarbons, changes in surface albedo as a result of land cover changes and deposition of carbon black on snow as well as solar irradiance changes, respectively [3].

Increased emission of greenhouse gases (GHG) through anthropogenic activities such as industrial activities, burning of fossil fuels, deforestation and urbanization are quite contributory to increase in surface air temperatures [3]. Greenhouse gases absorb some of the thermal infrared radiation given off by the earth's surface, and subsequently emit them back to the earth's surface, resulting in the increasing surface air temperature known as the greenhouse effect. Human activities have led to an increase in the concentration of greenhouse gases in the atmosphere, causing the Earth's surface to warm rapidly. In addition, greenhouse gases absorb thermal infrared radiation emitted by the Earth's surface and lower atmosphere, thereby exacerbating the greenhouse effect.

Verma *et al.* [8] has pointed out that the amount of radiation that can be altered by atmospheric aerosols depends primarily on the concentration, particle size distribution and composition of the atmospheric aerosols. Direct radiative forcing (DRF) results from perturbations to the Earth's atmosphere system due to direct interaction of atmospheric aerosols with the scattering or absorption of incident solar radiation. Fawole *et al.* [9] notes that emission of absorbed radiation by atmospheric aerosols alters the lifetime and micro-physical properties of clouds and this may eventually affect precipitation. Increasing population and industrialization has been pointed out to be culpable for the considerable increase in anthropogenic emissions of aerosols and gaseous pollutants in West Africa and a pattern expected to continue up to year 2030 [10]. Despite growing evidence that human-generated atmospheric aerosols have an impact on regional radiation budgets, there appear to be no strict regulations for emission standards in major African cities, and where they do exist, implementation and/or enforcement appear to be very weak [11].

The Earth-atmosphere system can be very responsive to land surface properties changes. Mounting evidence shows that land-use and land cover (LULC) changes may pose important climatic implications locally, regionally, and globally. The climate response to LULC changes in some instances may far outweigh the contribution from increasing greenhouse gases [12]. Natural and anthropogenic land use (*i.e.,* deforestation) and land cover changes (*i.e.*, desertification) can have a substantial impact on climate. Snyder *et al.* [6], notes that deforestation and desertification brings about an increase in sensible heat given off at the surface, with a reduced latent cooling compensating for the net radiation loss at the earth's surface resulting in a rise in surface air temperature, as the air is warmed by the sensible heat being convected and conducted from the surface.

Detection of trend in the time series of hydro climatic parameters has become the most sought-after technique to detect climate change and variability at local, regional and global basis and there appears to be no uniformity in the changes in the climatic parameters spatially or temporarily. Yue & Hashino [13] pointed out those considerable and significant temporal and spatial variations could exist amongst regions having different climates. Several statistical methods are been employed to evaluate trends in parameters of climatic interest [14-19]. They include but not limited to the Mann-Kendall's, least square linear regression and the Sen's slope trend tests etc. With a synergistic use of these methods, the possible trends in observed data can be adequately analyzed with respect to the direction, significance, Kendall's tau b and trend magnitude.

Many research studies have attempted to analyze surface air temperatures chronologically ordered observations (*i.e.*, time-series) from various climate change perspectives across a wider range of temporal and spatial scales. Their study indicated a significant increase of surface air temperatures in different parts of the world [20-22]. Climate change scenarios for Nigeria as examined by Abiodun *et al.* [20], using a 30-year data distribution that spanned from 1971-2000, reported upwards trends in surface air maximum and minimum temperatures. Many studies have shown positive trends in surface air temperatures although the changes vary variously amongst regions [23-26]. Analysis of 30 years' data for temperature and rainfall variability in Nigeria spanning from 1971-2000 conducted by Akinsanola & Ogunjobi [27], indicated surface air temperatures and rainfall significant increase in quite a number of stations they studied. Their results further suggested a sequence of alternately upward and downward trends in the two parameters. Oguntunde *et al.* [28] conducted a study to assess the possible occurrence of trends in surface air temperature across Nigeria from 1901-2000. Their results indicated that surface air minimum temperatures changes are higher than changes in surface air maximum temperatures. Amadi *et al.* [17] conducted a trend and variation study of basic Atmospheric parameters including but not limited to mean annual surface air temperatures. Their findings showed trends in the parameters across Nigeria from 1950-2012. Some trend studies in Nigeria focused on individual towns for relatively short periods [16, 29-32]. Most of these studies carried out in Nigeria focused on the last century, while others focused on small spatial scales, mostly using in-situ meteorological data.

Applied climate science attempts to embolden knowledge at local, regional and global scale. The more limited the scale at which such information is made available, the more important its relevance to users for most applications. The study of the trend and variability of weather and climate elements of a region is vital for sustainable agriculture, water resources management, power generation, marine and aviation safety etc. Most communities in Nigeria are vulnerable to the vagaries of climate change and variability, since they are exposed to several environmental hazards associated with climate change and variability. The effective use of weather and climate information to manage climate-related risks and prepare adaptive and mitigation measures to face future challenges is very vital. According to the IPCC report [3], after the high temperature, there will be a heat wave. High temperatures can trigger off incidences of diseases linked to high temperatures such as Cerebra-spinal meningitis and heat stroke. Also, changes in surface air temperatures influence quite a number of hydrological processes, including precipitation.

The need then arises to study the current trend and variations in mean annual surface air temperatures across the representative stations of the selected eco-climatic zones in Nigeria with the Integrated Earth System Analysis (IESA) approach using a multi-decadal, global reanalysis data. Reanalysis is a process in which a data assimilation system provides a consistent reprocessing of meteorological observations, typically covering an extended period of the historical data record.

The objectives of this study are:

1. To analyze the trend and variations in the historical records of the chosen parameters for the stations and period under study
2. To analyze the possible causes of the trend and variations of the chosen parameters.

Location and Brief Geography of the Study Area

Nigeria is located between latitudes 4° and 14°N and between longitudes 3° and 15°E of the Equator and Greenwich Meridian, respectively. The climate of Nigeria is typified by various ecotypes and climate zones and is influenced by the interplay of the Tropical Maritime and the Tropical Continental air masses and their associated Planetary Winds (the South-east and the North-east trade winds, respectively) [33]. The Tropical Maritime air mass originates from the Sub-tropical High Pressure belt, centered about 30°S of the equator, and off the coast of Namibia, while the Tropical Continental air mass emanates from the Sub-tropical High pressure belt., centered about 30°N, north of the equator and over the Sahara Desert [20]. The interactions of these two air masses defines the Wet and Dry season pattern in Nigeria. Teleconnection influences on the Nigerian landscape are imposed by the strong North Atlantic Oscillation (NAO) during the dry season and the El Nino- Southern Oscillation (ENSO) during the wet season [28].

Adefolalu [34] has pointed out that Nigeria may be divided into five eco-climatic zones - the Mangrove-swamp rainforest, the Tropical rainforest, the Guinea, Sudan and the Sahel Savannas (Figure 1). The characteristic of the eco-climatic zones is essentially defined by the vegetation pattern. Other factors such as rainfall, relief, soil type and human activity, may have significant impacts.

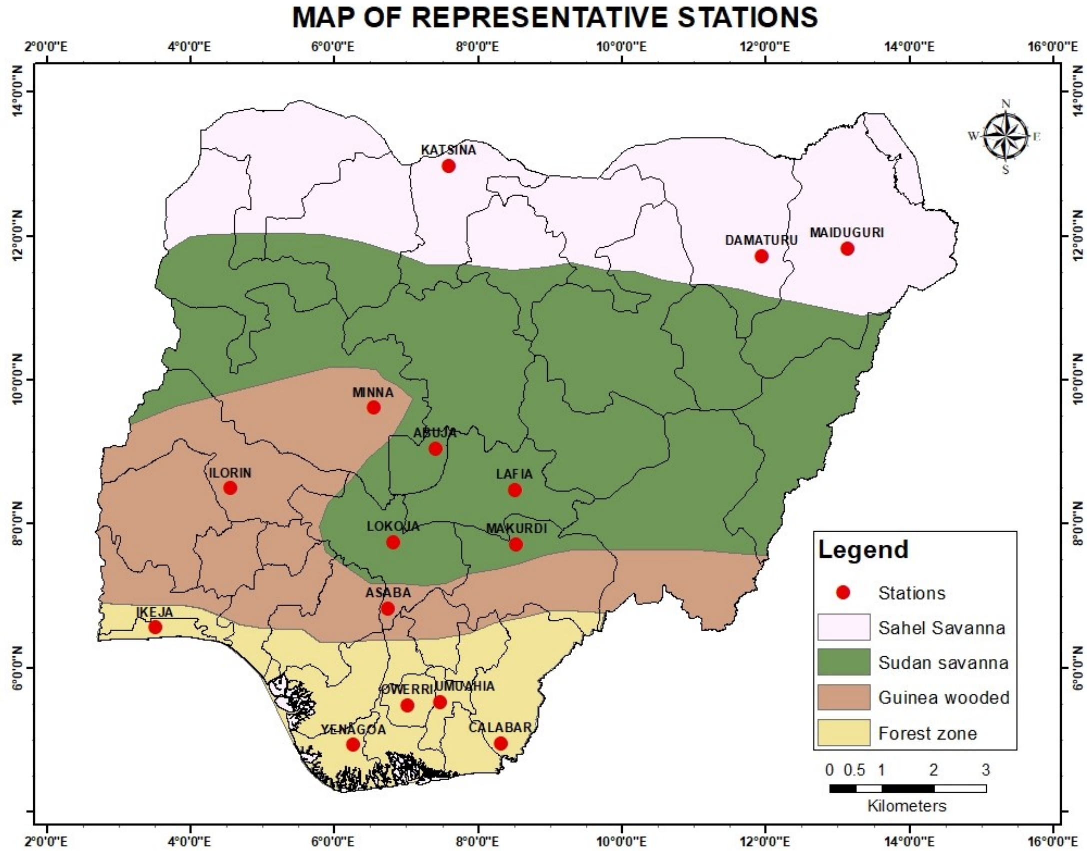

Fig. 1. The meteorological stations for the study and the eco-climatic zones

Data and Methodology

Dataset

The data for the analysis of mean annual surface air temperatures for trends across some representative stations of the selected eco-climatic zones in Nigeria is MERRA-2, obtained from the National Aeronautics and Space Administration (NASA) database. The GEOS Atmospheric model and the Grid Point Statistical Interpolation analysis scheme are considered important components of this system [36-38]. According to Gelaro *et al.* [35], reanalysis products are becoming increasingly used for climate monitoring.

The stations are the representative stations of the selected eco-climatic zones and the data represents the mean monthly values of surface air temperatures across Nigeria, spanning from 1981 to 2018. The parameters of interest are the surface air maximum and minimum temperatures. Detailed information on the stations, meteorological variables measured at the representative stations are presented in Table 1

Data Check and Smoothening

Data was checked for missing data, outliers and in homogeneities. The data had no missing values. Quality checks helps to remove outliers and their biases. Longobardi & Villani [39] pointed out that long-term climate analysis should be based on homogenous data, since there is large variability in space and time of climate variables. A homogeneous climate dataset is one having fluctuations/variations caused only by changes in weather and climate. Non-climatic factors introduce fluctuations/in homogeneities that produce gradual bias in the data distribution [17]. Thus, normality and homogeneity tests were conducted on the datasets.

Table 1. Summary information on the meteorological stations [20, 34, 35]

Station name	Latitude(°N)	Longitude(°E)	Altitude(m)	Eco-climatic Zones
Katsina	12.98	7.60	163.91	Sahel savanna
Maiduguri	11.83	13.15	331.51	
Damaturu	11.73	11.95	388.54	
Abuja	9.05	7.41	404.65	Sudan savanna
Lafia	8.48	8.52	163.91	
Lokoja	7.75	6.82	198.15	
Minna	9.62	6.55	346.62	Guinea-wooded savanna
Ilorin	8.50	4.55	283.03	
Makurdi	7.72	8.53	139.21	
Asaba	6.83	6.75	136.69	Tropical rainforest
Umuahia	5.53	7.48	92.84	
Owerri	5.48	7.02	60.61	
Ikeja	6.56	3.51	55.68	Mangrove-swamp rainforest
Calabar	4.95	8.32	34.68	
Yenagoa	4.93	6.26	13.06	

Methodology

The mean monthly datasets were converted to mean annual datasets. This study synergistically embraced the parametric linear trend test, the non-parametric Mann-Kendall (M-K), Sen’s slope trend tests and descriptive statistics. The literature [40, 41] has pointed out that more than one statistical test should be used to arrive at accurate interpretation of data and tests assumptions as each statistical test addresses a specific question.

The descriptive statistics showed the statistical characteristics of the mean annual values. The M-K trend test evaluated the trend direction, significance of the trend and the M-K tau b. The linear regression model using the least squares method and the Sen’s slope trend tests estimated the magnitudes of the trend. According to many authors [42-45], nonparametric tests have statistical advantages over parametric tests because they are insensitive to the presence of outliers and incomplete data and exhibit a degree of monotonic dependence. The results of the nonparametric tests differed from those of the parametric linear trend test, while the results of the M-K and Sen slope trend tests were better than those of the parametric tests.

The Mann-Kendall (M-K) Trend Test

According to Houghton [46], the M-K trend test statistics is evaluated using the sign of differences between successive values rather than on the values of the randomly selected variables. This non-parametric statistical tool has been variously used to analyze trends in hydro- climatic data [47, 48]. Hence it was adopted in this study.

Given a time series of n-size dataset, such that, the M-K test statistic (S) is evaluated with the formula [44, 49]:

$$S = \sum_{k=1}^{n-1} \quad \sum_{j=k+1}^{n} sgn\left(x_j - x_k\right) \qquad 1$$

where x_j and x_k are the sequential data values for the j^{th} and k^{th} terms, and j > k.

$$\mathrm{Sgn}(x_j - x_k) = \begin{cases} 1\ if\ x_j - x_k > 0 \\ 0\ if\ x_j - x_k = 0 \\ -1\ if\ x_j - x_k < 0 \end{cases} \qquad 2$$

An upward trend (later values exceeding earlier values) is denoted by a large positive value of test statistic (*S*). A downward trend (later values not exceeding earlier values) is denoted by a large negative value of the test statistic (*S*). A small absolute M-K test statistic(S) value connotes that a trend does not exist.

The variance of *S, VAR(S)* (σ^2) where ties are not present (*i.e.*, j=k does not exist) is denoted by

$$VAR(S) = \frac{n(n-1)(2n+5)}{18} \qquad 3$$

where ties are present, the variance of *S* is defined as

$$VAR(S) = \frac{1}{18}\left[n(n-1)(2n+5) - \sum_{p=1}^{q} t_p\ (t_p - 1)(2t_p + 5)\right] \qquad 4$$

From Eqn. 4, q denotes the number of tied groups (where j=k), and t_p denotes the number of data values in the p^{th} group.

Computation of Z test statistic is done using the values of M-K test statistic(*S)* and the variance of the M-K test statistic, *AR*(*S*) as follows:

$$Z = \begin{cases} \frac{S-1}{\sqrt{VAR(S)}} if\ S > 0 \\ 0 \quad if\ S = 0 \\ \frac{S+1}{\sqrt{VAR(S)}}\ if\ S < 0 \end{cases} \qquad 5$$

An upward or downward trend is indicated by a positive or negative value of *Z,* respectively. For a two-tailed test, the null hypothesis *Ho* implies that a linear trend does not exist and that the data distribution is randomly ordered and independent. An alternative hypothesis H_1 implies that a linear trend does exist. For the null hypothesis H_0 to be rejected, the absolute value of *Z* evaluated using Eqn. 5 must be greater than the critical value $Z_{\alpha/2}$, at the selected significance level, for the null hypothesis H_0 to e rejected. Other than that, the null hypothesis is accepted.

The Linear Trend Test

The linear trend and Sen's slope trend tests were used in estimating the trend magnitudes. A test for linear trend is denoted by the linear regression of y on time t.

$$y = \beta_0 + \beta_1 x + \varepsilon \qquad 6$$

The slope is denoted by β_1. The intercept on y is denoted by β_0, which is the value of y at x = 0. The dependent variable is y, the independent variable is x, and ε is the error, residual or deviation which may be positive, negative or zero and are caused by random effects. The dependent variable y value corresponding to a given independent variable x value is estimated by finding the value of y from the least-squares line that fits the data.

The null hypothesis is that slope coefficient, $\beta_1 = 0$ (*i.e.,* lack of linear dependence) and the alternative hypothesis is that slope coefficient $\beta_1 \neq 0$ (linear dependence exists). A significant slope different from zero is the condition for rejection of the null hypothesis and the alternative hypothesis that there is a linear trend in y over time with the rate equal to β_1 is accepted.

The Sen's Slope Trend Test

Determination of trend magnitude in hydro-meteorological time series has been variously executed using the Sen's slope trend test [13, 44].

The presence of a monotonic trend and the linearity of the trend allow for the estimation of the trend magnitude using the Sen's line. How the median data changes linearly with time is modeled by the non-parametric Sen's line. The trend magnitude for the time interval covered by the study is obtained by multiplying the estimated slope per year by the total number of years covered by the study.

According to Sen [49], the slope magnitude can be obtained as follows:

$$b_{sen} = Median\left[\frac{Y_i - Y_J}{(i-j)}\right] \text{for all j < i} \qquad 7$$

where Y_i and Y_j are data at time points i and j, respectively.

If the total number of data points in the series is *n,* then the corresponding slope estimates will be $\frac{n(n-1)}{2}$ and the test statistic b_{sen} will be the median of all slope estimates. Increasing or decreasing trend is shown by a positive or negative value of the test statistic, respectively.

The p-value

The p-value delineates a region in the tail of a probability distribution beyond the noticeable values of the selected test statistic. When the p-value is small, the corresponding selected test statistic value will be seen to be particularly high and when the p-value is large, the corresponding selected test statistic will be seen to be very small. When the p-value is smaller than the selected significance level, the null hypothesis is rejected on the assumption that the data is not consistent with the null hypothesis at the selected significance level and vice versa.

Results

Results of Mean Annual Surface Air Temperatures

Spatial Variability of Mean Annual Surface Air Temperatures

Table 2 shows that the mean annual surface air maximum temperature ranges from 28.15°C to 35.70°C. The highest value of the mean annual surface air maximum temperatures is noticeable in Maiduguri in the Sahel Savanna eco-climatic zone, while the lowest value is noticeable in Calabar in the Mangrove-Swamp rainforest eco-climatic zone. Table 3 shows that the mean annual surface air minimum temperature ranges from 19.84°C to 24.33°C. The highest value is observed in Calabar in the Mangrove-swamp rainforest eco-climatic zone, while the lowest value is observed in Katsina in the Sahel savanna eco-climatic zone.

The coefficient of variation for both mean annual surface air maximum and minimum temperatures are shown in Tables 2 and 3.The coefficient of variation for mean annual surface air maximum temperature range from 1.868 to 3.670. The highest value of coefficient of variation in mean annual surface air maximum temperature is noticeable in Abuja in the Sudan savanna eco-climatic zone, while the lowest value is noticeable in Calabar in the Mangrove-swamp rainforest eco-climatic zone. The coefficient of variation of mean annual surface air minimum temperature range from 1.563 to 3.367. The highest value in coefficient of variation of mean annual surface air minimum temperature is noticeable in Minna in the Guinea-wooded savanna eco-climatic zone and the lowest value in Calabar in the Mangrove-swamp rainforest eco-climatic zone.

For the mean annual surface air maximum temperature, all the 15 stations have positively valued coefficients of skewness. Thirteen (13) stations have negatively valued and two (2) stations positively valued coefficients of kurtosis (Table 2). For the mean annual surface air minimum temperature, ten (10) stations have negatively valued and five (5) stations positively valued coefficients of skewness and all the stations have negatively valued coefficients of kurtosis (Table 3)

Seasonal Variability of Mean Annual Surface Air Temperatures

Figures 2~6 show the variability of mean annual surface air maximum temperature across the representative stations. Figures 7~11 show the variability of mean annual surface air minimum temperatures across the representative stations.

Trend in Mean Annual Surface Air Temperatures

Tables 4 and 5 show the trend of mean annual surface air maximum temperatures. The Mann-Kendall's test statistic(S) ranges from -113 to 398, the coefficients of time trends range from -0.161 to 566, and the trend magnitude increase ranges from 0.015° to 0.073 °C/year for mean annual surface air maximum temperatures across the selected eco-climatic zones in Nigeria. The highest trend magnitude in mean annual surface air maximum temperature is noticeable in the Lafia (*i.e.,* 0.073 °C/year), while the lowest value is observed in the Yenagoa (*i.e.,* 0.015 °C/year) (Table 4).

Tables 6 and 7 show the trend of mean annual surface air minimum temperatures. The Mann-Kendall's test statistic(S) ranges from 280 to 446, the coefficients of time trends (*i.e.*, the Kendall's tau b) range from 0.398 to 0.634, and the trend magnitude increase ranges from 0.024° to 0.069 °C/year for mean annual surface air minimum temperatures across the selected eco-climatic zones in Nigeria. The highest trend magnitude in mean annual surface air minimum temperature is noticeable in Abuja (*i.e.*, 0.069 °C/year), while the lowest value is noticeable in Katsina and Ikeja (*i.e.,* 0.024 °C/year) (Table 6).

Figs. 12~16 are the normalized time series anomaly plots for mean annual surface air maximum temperature, showing monotonic upward trends in the plots of 14 stations. A monotonic downward trend is shown by one station (*i.e.,* Ikeja). Figs. 17~21 are the normalized time series anomaly plots for mean annual surface air minimum temperature showing monotonic upward trends in all the 15 stations.

Table 2. Descriptive statistics for mean annual surface air maximum temperature

Station name	Number of years	Mean (°C)	Standard deviation	Coefficients Of variation	Coefficients Of skewness	Coefficients Of Kurtosis
Maiduguri	*38*	**35.70**	0.8078	2.263	0.120	- 0.860
Damaturu	*38*	**34.57**	0.8997	2.603	0.113	-0.580
Katsina	*38*	**33.90**	0.6331	1.868	0.375	-0.589
Ilorin	*38*	**31.98**	0.6962	2.177	0.196	-1.199
Lafia	*38*	**31.41**	1.0487	3.339	0.219	-1.169
Lokoja	*38*	**30.97**	0.9301	3.003	0.473	-0.191
Minna	*38*	**30.68**	1.0802	3.521	0.531	-0.387
Abuja	*38*	**30.59**	1.1228	3.670	0.396	-0.862
Makurdi	*38*	**30.53**	0.8467	2.773	0.310	-0.893
Asaba	*38*	**29.61**	0.5884	1.987	0.446	-0.452
Owerri	*38*	**29.17**	0.3152	1.081	0.244	-0.231
Umuahia	*38*	**29.10**	0.3397	1.167	0.258	-0.335
Ikeja	*38*	**28.88**	0.2936	1.017	0.708	1.023
Yenagoa	*38*	**28.73**	0.2794	0.973	0.154	-0.257
Calabar	*38*	**28.15**	0.3097	1.100	0.172	0.795

Table 3. Descriptive statistics for mean annual surface air minimum temperature

Station name	Number of Years	Mean (°C)	Standard deviation	Coefficient of variation	Coefficient of skewness	Coefficient of Kurtosis
Katsina	38	19.84	0.468	2.358	0.020	-O.497
Minna	38	20.32	0.684	3.367	0.433	-0.445
Abuja	38	20.34	0.661	3.249	0.220	-0.996
Damaturu	38	20.65	0.523	2.533	-0.274	-0.337
Maiduguri	38	21.19	0.493	2.327	-0.422	-0.180
Ilorin	38	21.48	0.472	2.197	-0.082	-0.957
Makurdi	38	21.59	0.567	2.626	0.035	-1.207
Lafia	38	21.79	0.648	2.973	0.135	-1.287
Lokoja	38	21.86	0.609	2.786	-0.008	-1.051
Asaba	38	21.86	0.499	2.283	-0.187	-0.875
Umuahia	38	22.15	0.472	2.131	-0.270	-0.974
Owerri	38	22.40	0.472	2.107	-0.276	-0.932
Yenagoa	38	23.38	0.446	1.908	-0.393	-0.715
Ikeja	38	23.51	0.391	1.663	-0.551	-0.323
Calabar	38	24.33	0.385	1.583	-0.273	-0.958

Table 4. Results of Mann-Kendall's and Sen's slope trend tests for mean annual surface air maximum temperatures

Station name	S	Kendall's tau b	Z	Sen's slope estimates (°C/year)	p-value
Maiduguri	255	0.363**	3.1938	0.039**	1.404E-03
Damaturu	284	0.404**	3.5587	0.043**	3.727E-04
Katsina	196	0.279*	2.4529	0.020*	1.417E-02
Ilorin	129	0.184	1.6098	0.019	0.1074420
Lafia	398	0.566**	4.9914	0.073**	5.993E-07
Lokoja	320	0.455**	4.0114	0.051**	6.036E-05
Minna	365	0.519**	4.5762	0.065**	4.736E-06
Abuja	364	0.518**	4.5640	0.069**	5.019E-06
Makurdi	388	0.552**	4.8665	0.058**	1.136E-06
Owerri	316	0.450**	3.9632	0.019**	2.925E-04
Asaba	269	0.383**	3.3698	0.028**	7.522E-04

Ikeja	-113	-161	4.6035	-0.006	0.1587637
Umuahia	318	0.452**	3.9869	0.020**	6.695E-05
Yenagoa	284	0.404**	3.5594	0.015**	8.041E-03
Calabar	345	0.491**	4.3270	0.017**	1.511E-05

**Kendall’s tau b is significant at the 0.01 level (2-tailed)
*Kendall’s tau b is significant at the 0.05 level (1-tailed)
**Slope is significant at the 0.01 level (2-tailed)
*Slope is significant at the 0.05 level (1-tailed)

Table 5. Results of linear trend estimation for mean annual surface air maximum temperature

Station name	**Parameters**	**Slope estimates (°C/year)**	**Standard error**	**Students t-test**	**p-value**
Maiduguri	Slope	0.039**	0.011	3.5862	4.77E-04
	Intercept	34.933	0.131	272..412	4.36E-02
Damaturu	Slope	0.048**	0.011	4.3837	8.50E-05
	Intercept	33.628	0.146	236.828	7.46E-03
Katsina	Slope	0.022*	0.009	2.4022	1.60E-02
	Intercept	33.465	0.103	330.044	5.58E-01
Ilorin	Slope	0.016	0.011	1.2883	1.25E-01
	Intercept	31.674	0.113	283.215	9.90E-01
Lafia	Slope	0.0075**	0.010	7.8234	2.01E-09
	Intercept	29.939	0.170	184.621	2.92E-07
Lokoja	Slope	0.052**	0.012	4.5241	3.71E-05
	Intercept	29.96	0.151	205.252	2.23E-03
Minna	Slope	0.069**	0.012	5.8302	6.22E-07
	Intercept	29.331	0.175	175.050	3.83E-05
Abuja	Slope	0.073**	0.012	6.0492	2.68E-07
	Intercept	29.157	0.182	167.914	1.54E-05
Makurdi	Slope	0..059**	0.008	7.1710	1.54E-08
	Intercept	29.384	0.137	222.263	4.90E-06
Asaba	Slope	0.028**	0.004	3.4982	6.87E-04
	Intercept	29.069	0.096	310.227	9.02E-02
Owerri	Slope	0.018**	0.004	4.7703	2.03E-05
	Intercept	28.3323	0.051	570.588	3.66E-01
Umuahia	Slope	0.020**	0.004	4.8984	1.21E-05
	Intercept	228.72	0.055	528.139	1.92E-01
Ikeja	Slope	-0.0069	0.044	-1.7697	1.11E-01
	Intercept	29.017	0.048	606.314	1.37E-07
Yenagoa	Slope	0.014**	0.004	3.8055	5.30E-04
	Intercept	28.468	0.045	633.952	8.00E-01
Calabar	Slope	0.018**	0.004	4.1381	8.17E-06
	Intercept	27.79	0.050	560.224	7.46E-01

**Slope is significant at the 0.01 level (2-tailed)
*Slope is significant at the 0.05 level (1-tailed)

Table 6. Mann-Kendall and Sen's slope trend tests for mean annual surface air minimum temperatures

Station name	S	Kendall's tau b	Z	Sen slope (°C/year)	p-value
Maiduguri	289	0.411**	3.6219	0.027**	2.925E-04
Damaturu	345	0.491**	4.3261	0.031**	1.518E-06
Katsina	280	0.398**	3,5089	0.024**	4.499E-04
Ilorin	366	0.521**	4.5906	0.029**	4.421E-06
Lafia	415	0.590**	5.2056	0.048**	1.934E-07
Lokoja	385	0.548**	4.8284	0.043**	1.132E-06
Minna	407	0.579**	5.1050	0.045**	2.735E-07
Abuja	364	0.518**	4.5640	0.069**	1.285E-07
Makurdi	388	0.552**	4.8673	0.038**	1.132E-06
Asaba	394	0.560**	4.9419	0.033**	7.735E-07
Owerri	410	0.583**	5.1439	0.033**	1.323E-04
Umuahia	391	0.556**	4.9038	0.033**	9.399E-07
Yenagoa	414	0.589**	5.1953	0.031**	2.043E-07
Calabar	446	0.634**	5.6340	0.030**	1.761E-08
Ikeja	348	0.495**	4.3651	0.024**	1.271E-05

**Kendall's tau b is significant at the 0.01 level (2-tailed)

**Slope is significant at the 0.01 level (2-tailed)

Table 7. Results of linear trend estimation for mean annual surface air minimum temperature

Station name	Parameters	Slope estimates (°C/year)	Standard error	Students t-test	p-value
Maiduguri	Slope	0.027**	0.006	4.2017	7.65E-05
	Intercept	20.671	0.08005	264.667	1.10E-02
Damaturu	Slope	0.031**	0.006	5.1639	6.93E-06
	Intercept	20.044	0.08490	243.210	1.25E-03
Katsina	Slope	0.024**	0.006	4.0525	1.33E-04
	Intercept	19.368	0.07586	261.603	1.32E-04
Ilorin	Slope	0.031**	0.005	5.49899	1.11E-06
	Intercept	20.903	0.07665	280.258	6.55E-04
Lafia	Slope	0.047**	0.006	7.9952	8.95E-10
	Intercept	20.876	0.10506	207.447	2.66E-07
Lokoja	Slope	0.041**	0.006	6.6786	4.39E-08
	Intercept	21.05	0.09876	221.315	1.18E-05
Minna	Slope	0.046**	0.007	6.5024	6.69E-08
	Intercept	19.418	0.11102	183.002	6.51E-06
Abuja	Slope	0.046**	0.006	7.0835	8.86E-09
	Intercept	19.44	0.10720	189.767	1.28E-06
Makurdi	Slope	0.039**	0.006	6.8273	3.24E-08
	Intercept	20.834	0.09194	234.822	1.28E-08
Asaba	Slope	0.034**	0.005	6.6422	5.06E-08
	Intercept	21.20	0.08097	269.966	4.5E-05
Owerri	Slope	0.033**	0.044	7.3927	6.52E-09
	Intercept	21.753	0.07659	292.493	1.51E-05
Umuahia	Slope	0.032**	0.005	6.8802	2.93E-08
	Intercept	21.52	0.07664	289.009	4.66E-05
Ikeja	Slope	0.025**	0.004	5.7450	1.23E-06
	Intercept	23.035	0.06338	370.915	4.62E-03
Yenagoa	Slope	0.031**	0.0042	7.4115	8.71E-09
	Intercept	22.768	0.0724	322.836	4.23E-05
Calabar	Slope	0.029**	0.004	8.8284	1.35E-10
	Intercept	23.767	0.6238	389.961	1.08E-05

**Slope is significant at the 0.01 level (2-tailed)

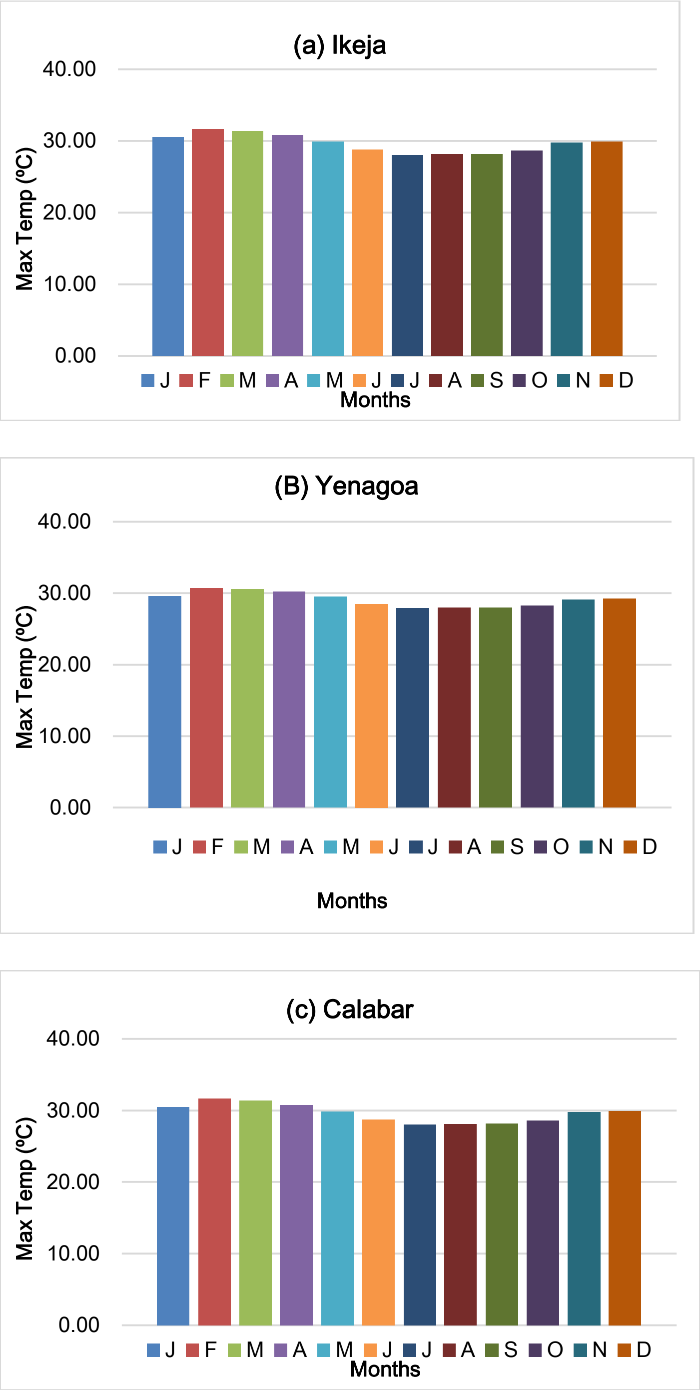

Fig. 2. Seasonal variation of mean annual surface air maximum temperature for representative stations (a: Ikeja, b: Yenagoa, and c: Calabar) of the Mangrove-swamp rainforest eco-climatic zone

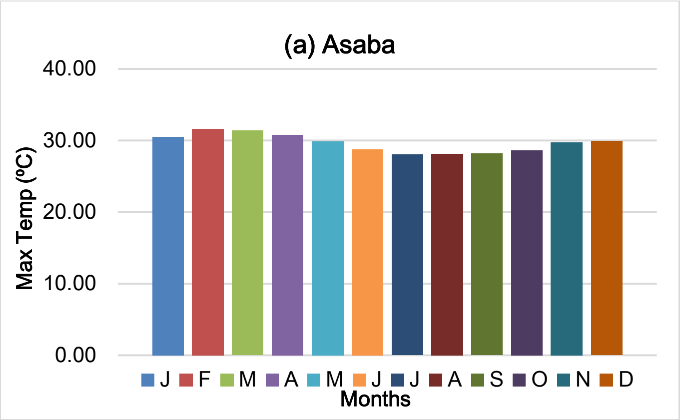

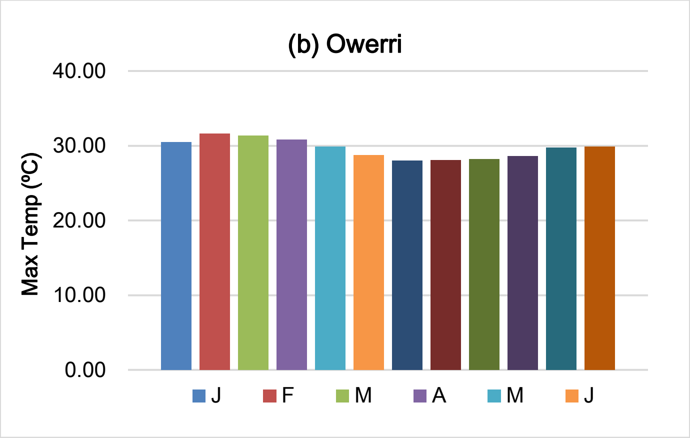

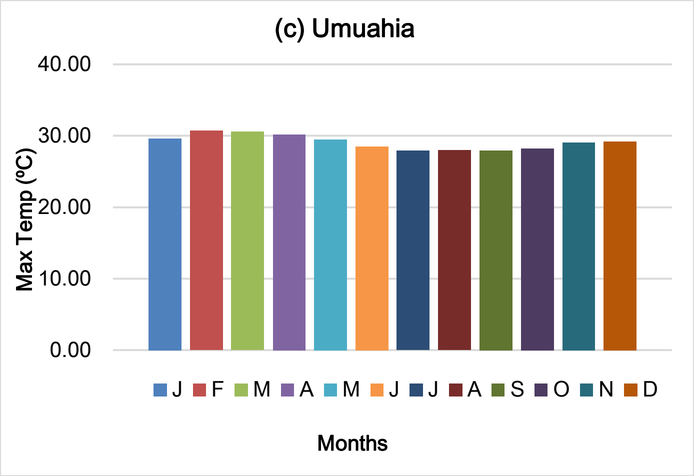

Fig. 3. Seasonal variation of mean annual surface air maximum temperature for representative stations (a: Owerri, b: Asaba and c: Umuahia) of the Tropical rainforest eco-climatic zone

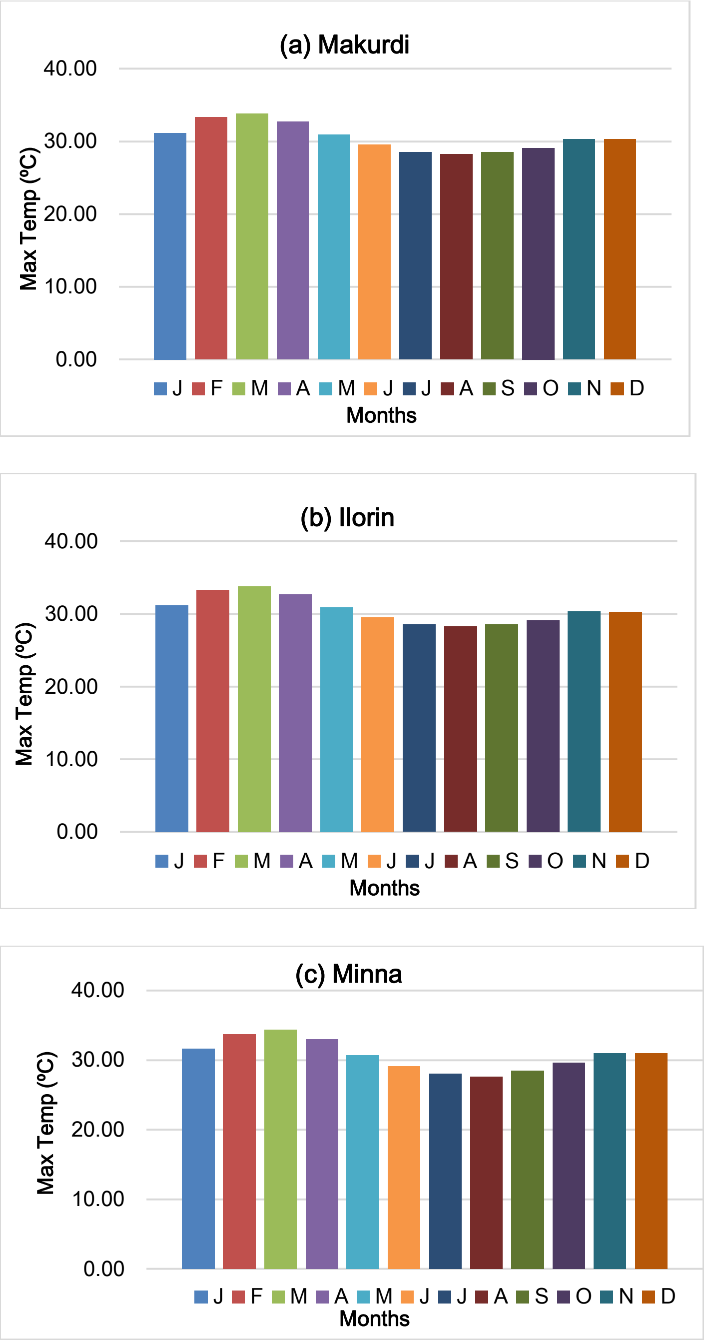

Fig. 4. Seasonal variation of mean annual surface air maximum temperature for representative stations (a: Makurdi, b: Ilorin and c: Minna) of the Guinea-wooded savanna eco-climatic zone

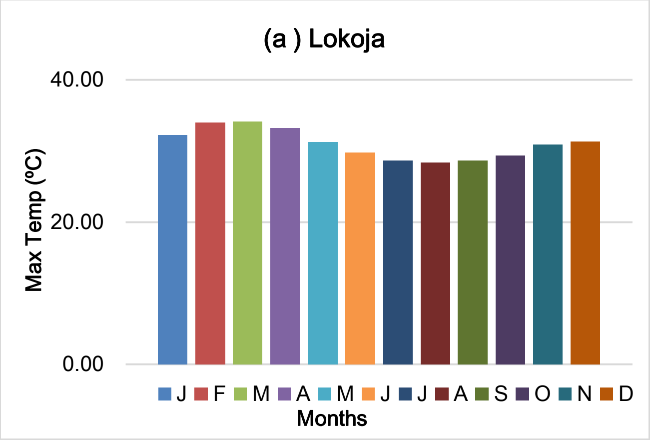

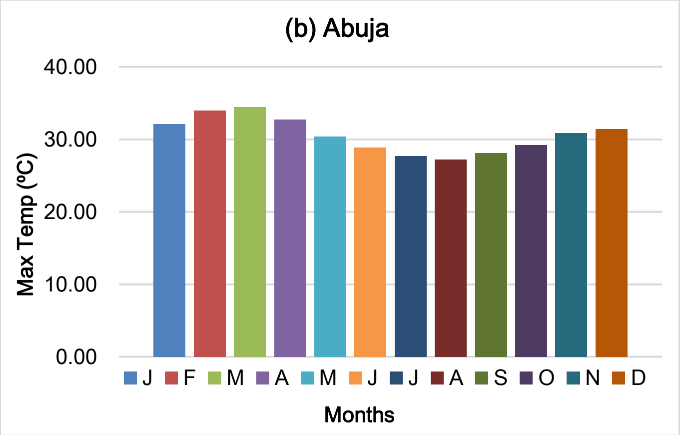

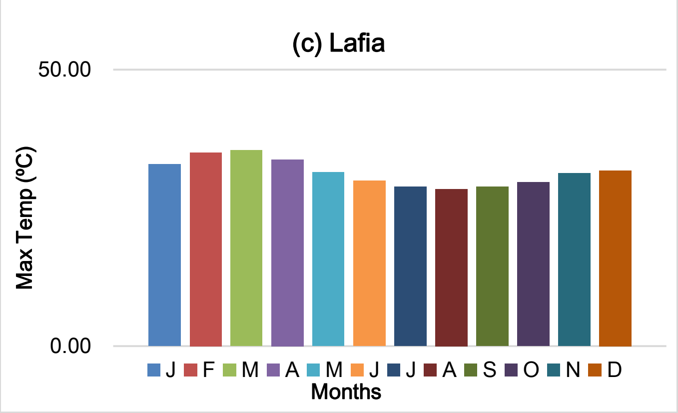

Fig. 5. Seasonal variation of mean surface air maximum temperature for representative stations (a: Lokoja, b: Abuja and c: Lafia) of the Sudan savanna eco-climatic zone

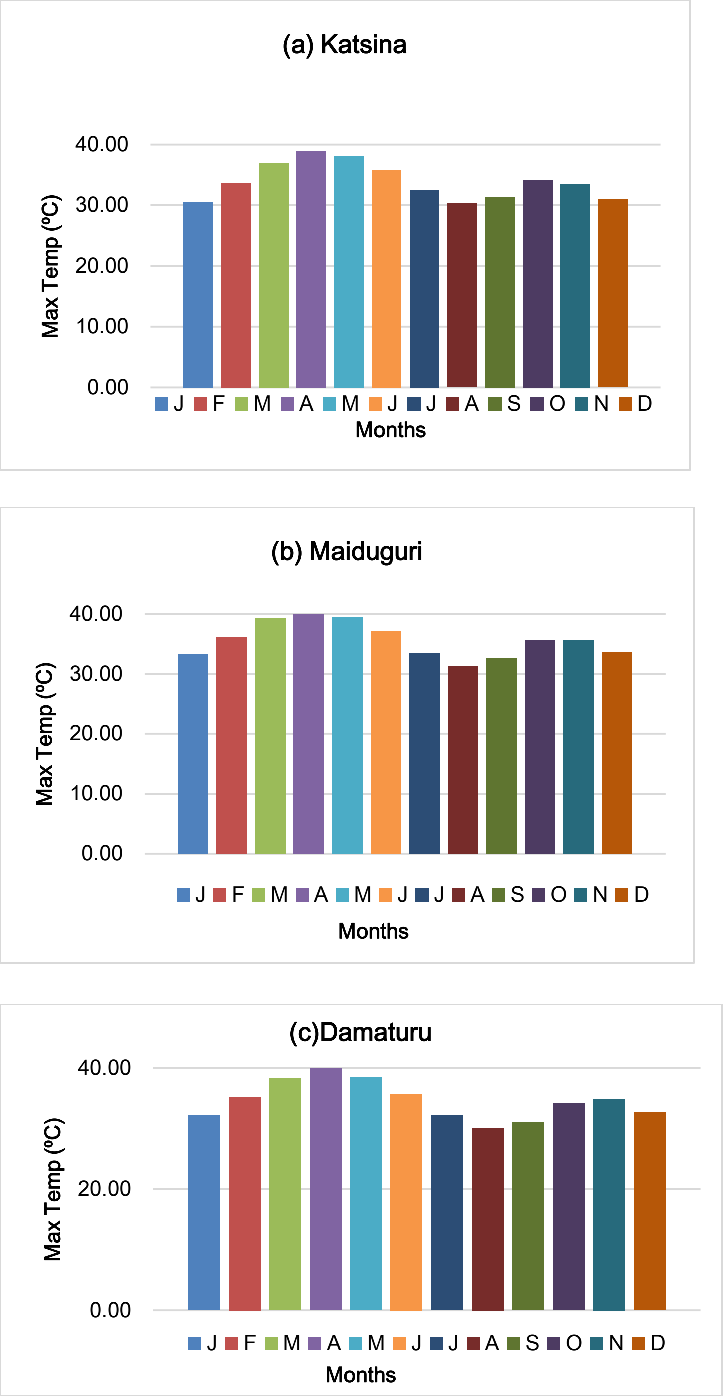

Fig. 6. Seasonal variation of mean surface airmaximum temperature for representative stations (a:Katsina, b:Maiduguri and c:Damaturu) of the Sahel savanna eco-climatic zone

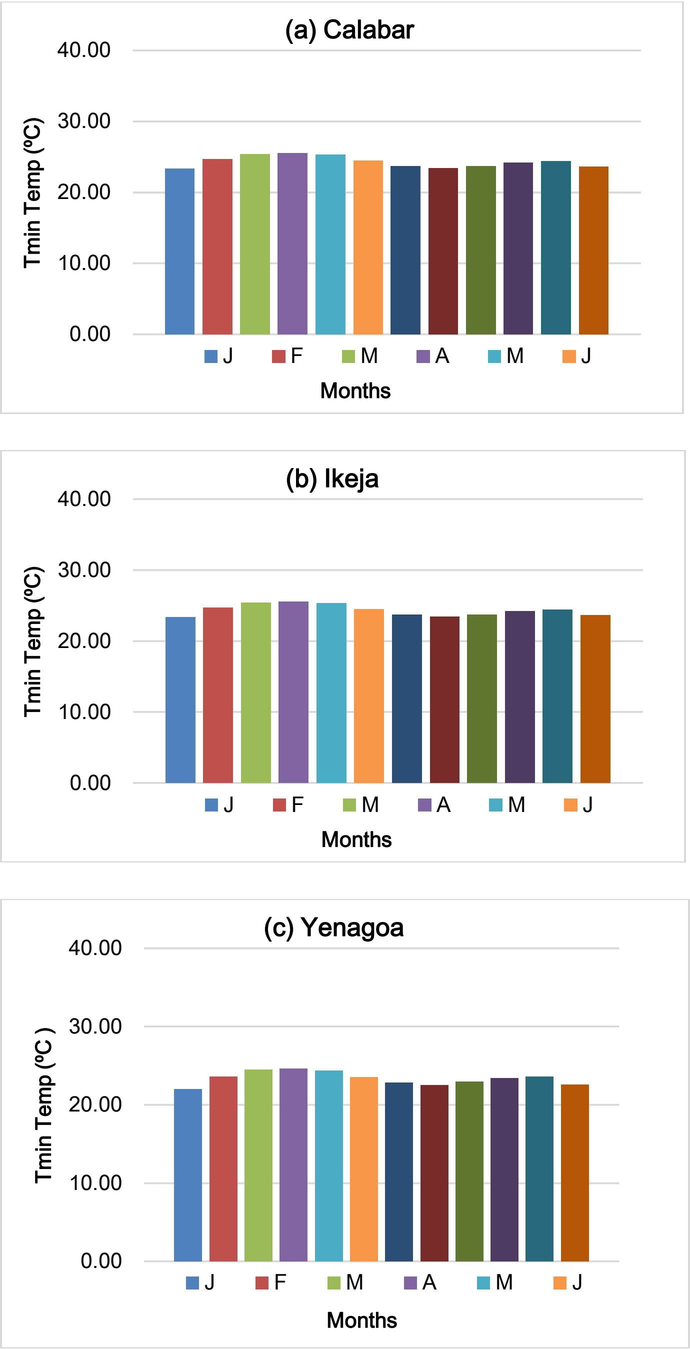

Fig. 7. Seasonal variation of mean surface air minimum temperature for representative stations (a: Calabar, b: Ikeja and c: Yenagoa) of the Mangrove-swamp rainforest eco-climatic zone

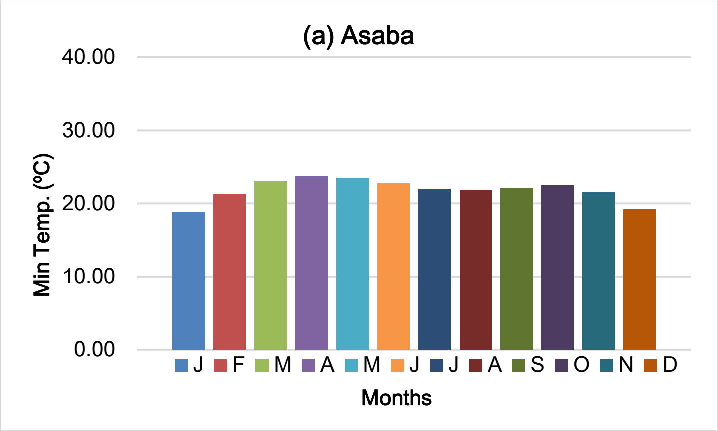

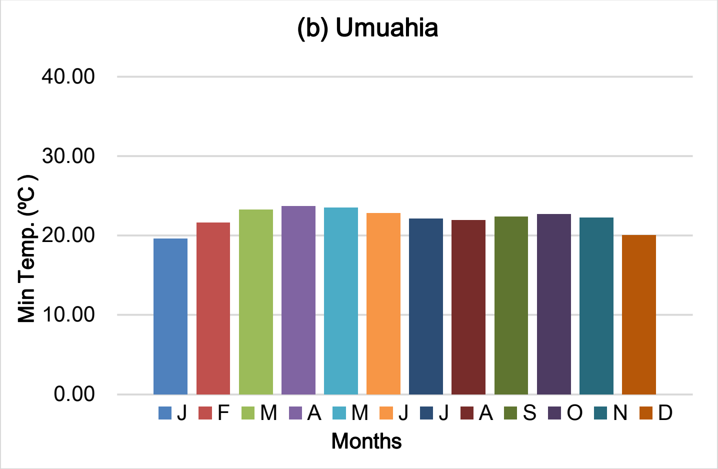

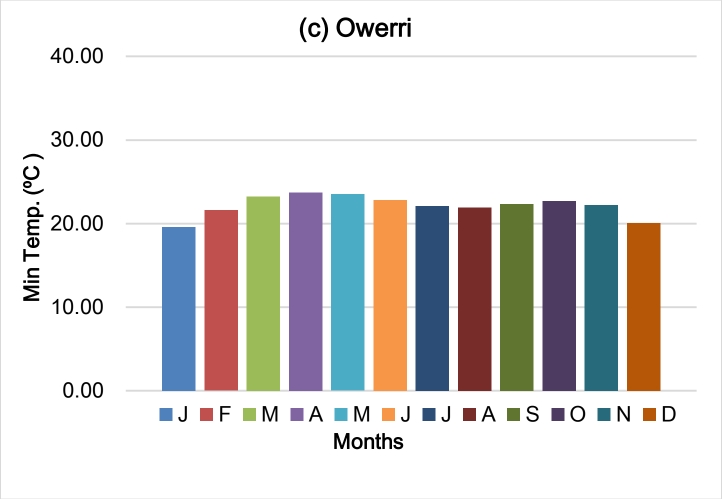

Fig. 8. Seasonal variation of mean annual surface air minimum temperature for representative stations (a: Asaba, b: Umuahia, and c: Owerri) of the Tropical rainforest eco-climatic zone

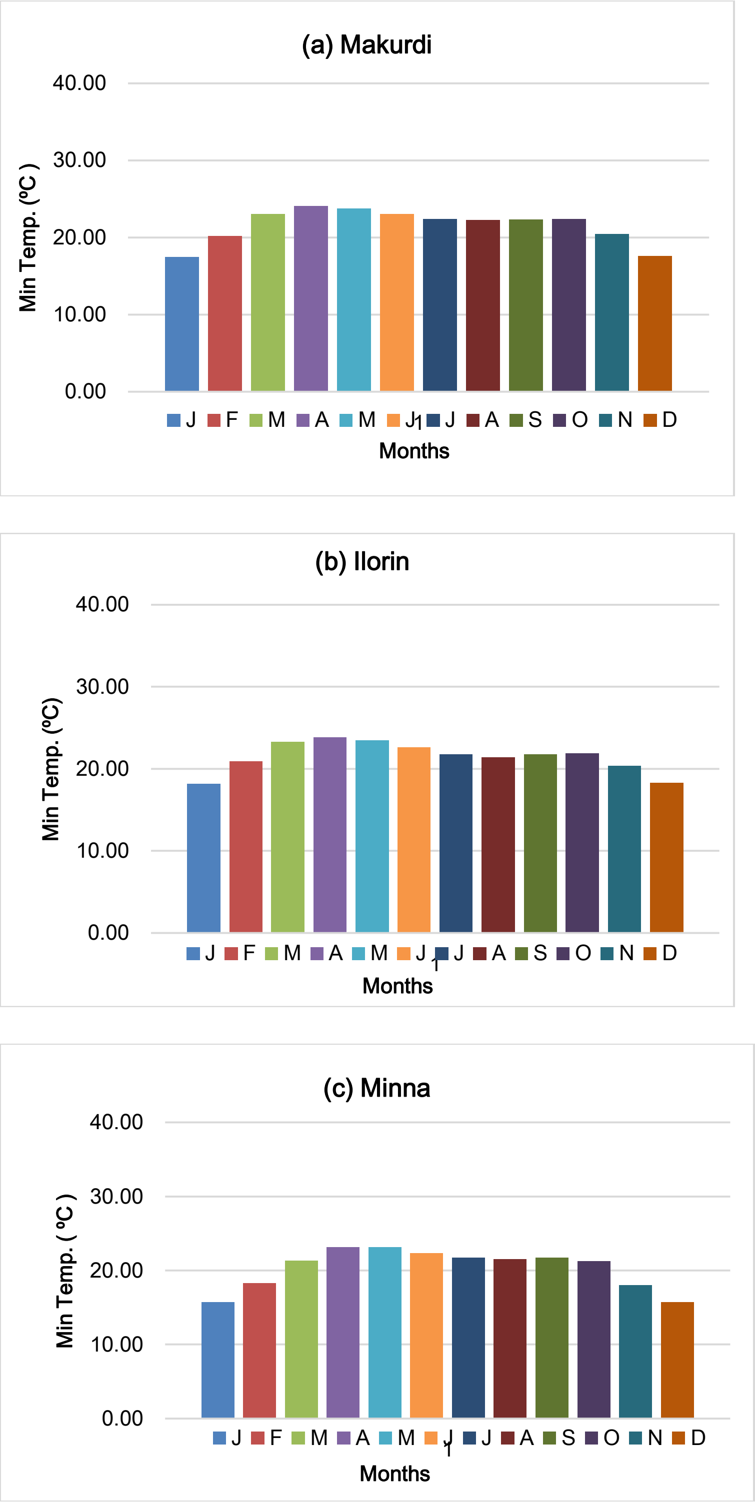

Fig. 9. Seasonal variation of mean annual surface air minimum temperature for representative stations (a: Makurdi, b: Ilorin and c: Minna) of the Guinea-wooded savanna eco-climatic zone

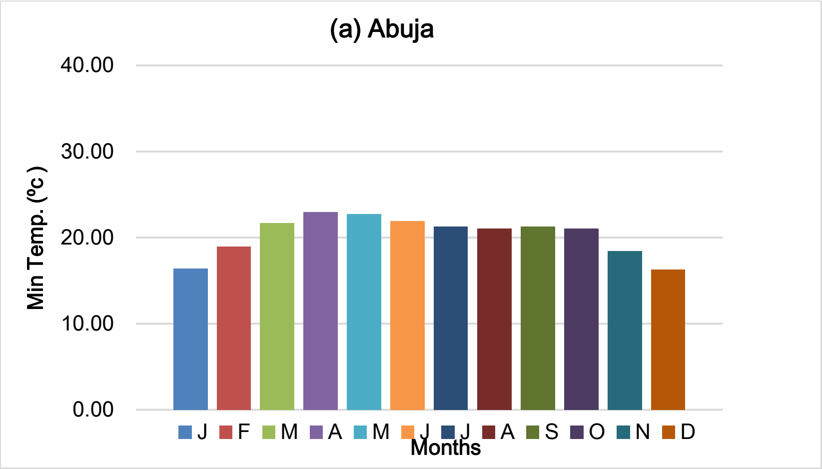

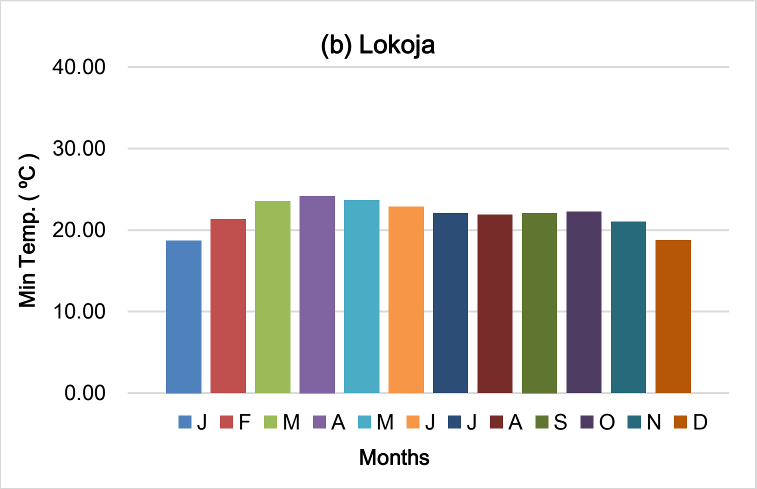

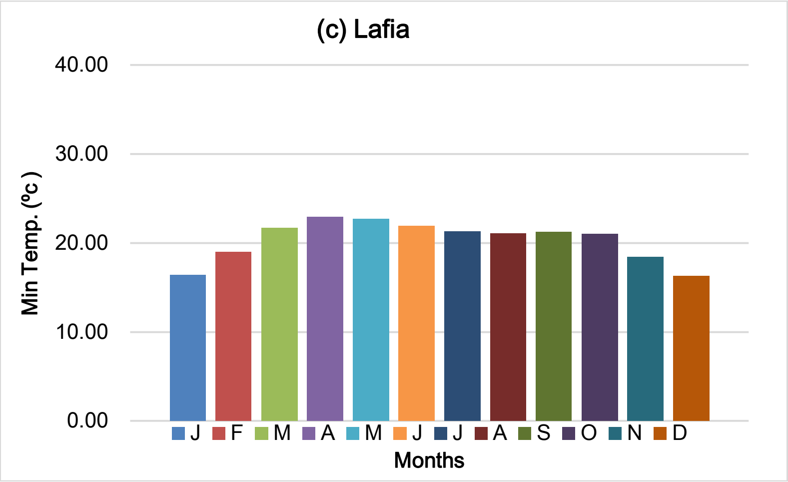

Fig. 10. Seasonal variation of mean annual surface air minimum temperature for representative stations (a: Abuja, b: Lokoja and c: Lafia) of the Sudan Savanna eco-climatic zone

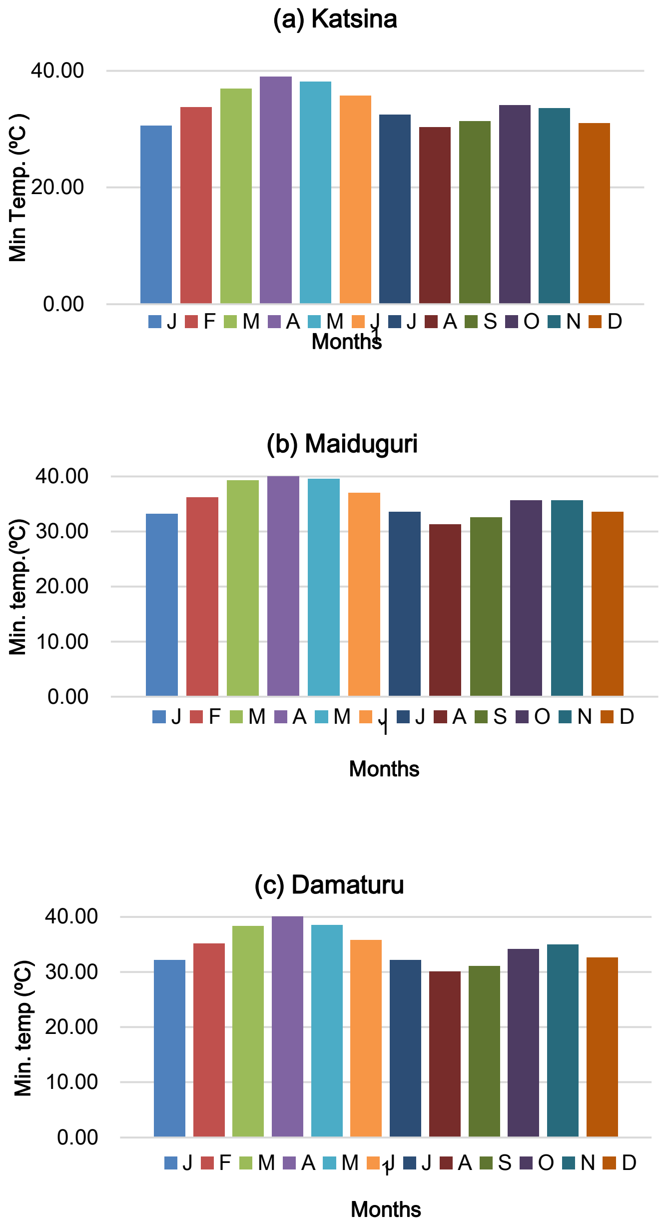

Fig. 11. Seasonal variation of mean annual surface air minimum temperature for representative stations (a: Katsina, b: Maiduguri and c: Damaturu) of the Sahel savanna eco-climatic zone

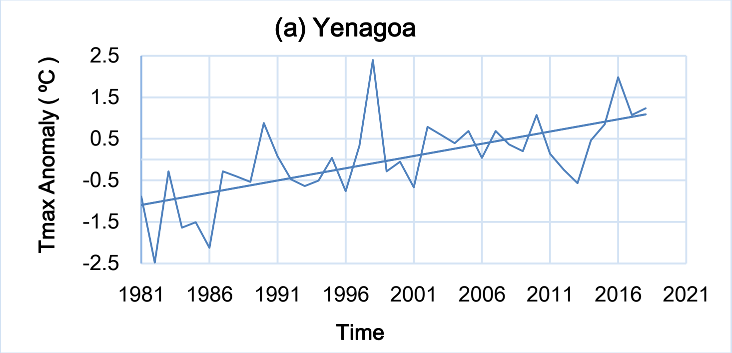

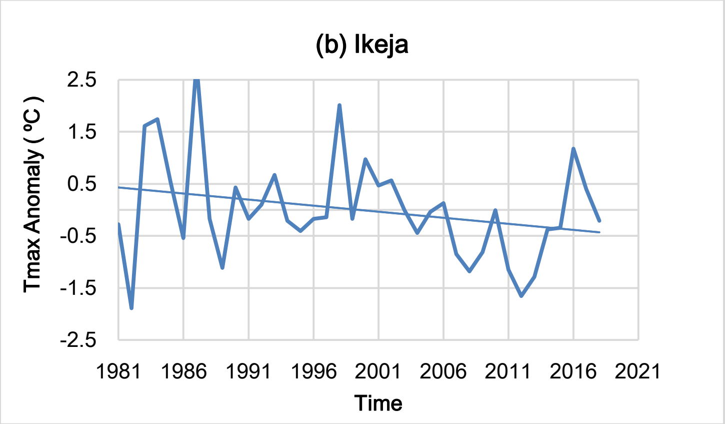

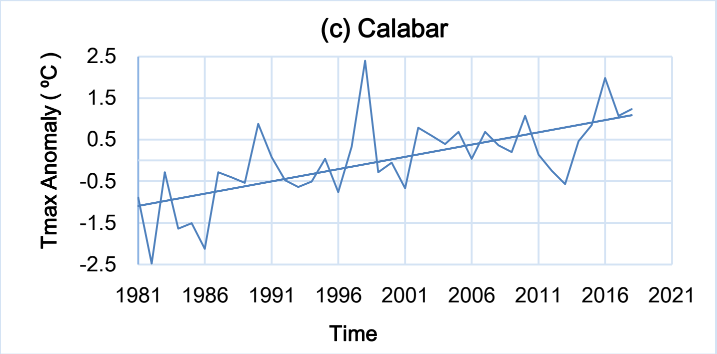

Fig. 12. Normalized time series anomaly plots for mean annual surface air maximum temperatures for representative stations (a: Yenagoa, b: Ikeja and c: Calabar) of the Mangrove-swamp rainforest eco-climatic zone

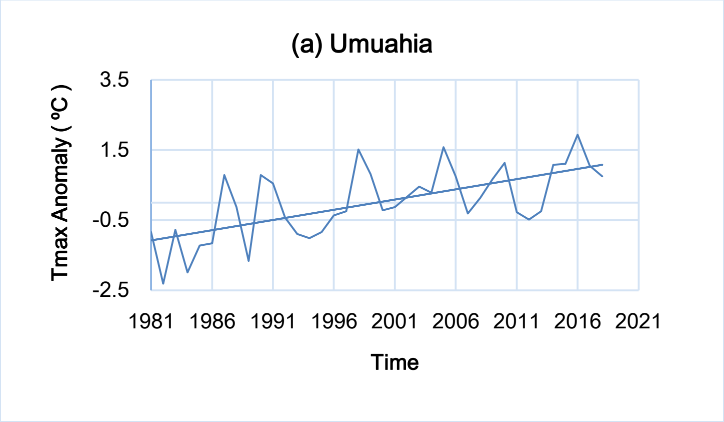

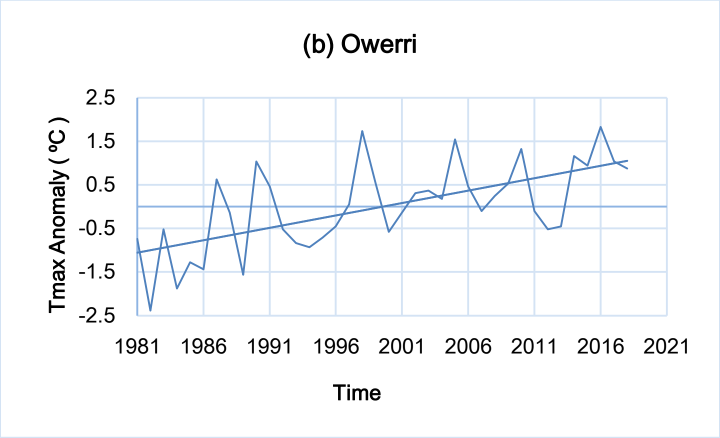

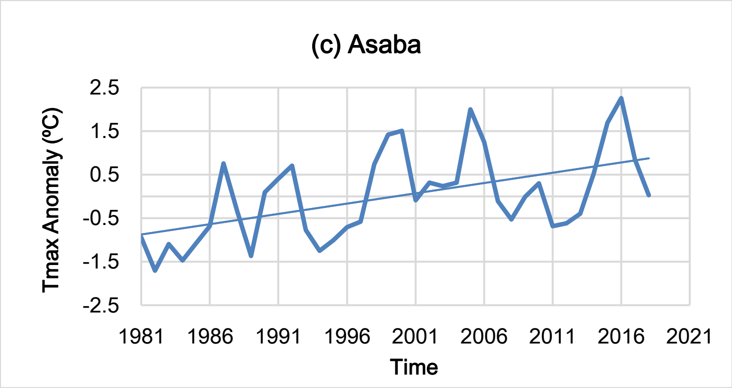

Fig. 13. Normalized time series anomaly plots for mean annual surface air maximum temperatures for representative stations (a: Umuahia, b: Owerri and c: Asaba) of the Tropical rainforest eco-climatic zone

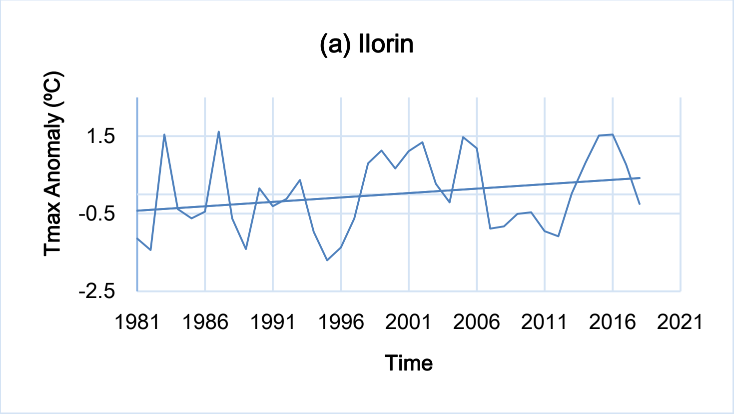

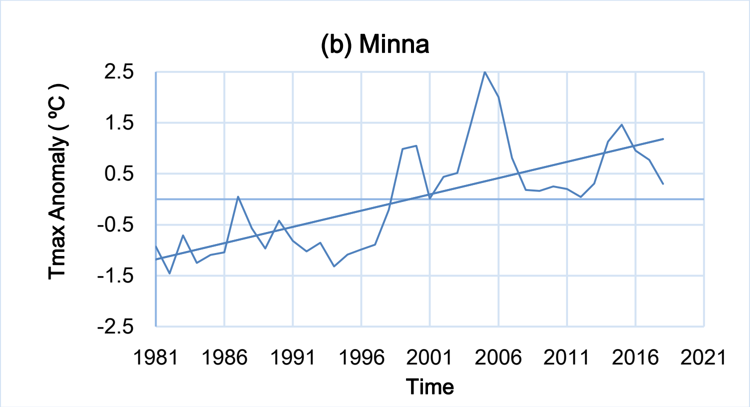

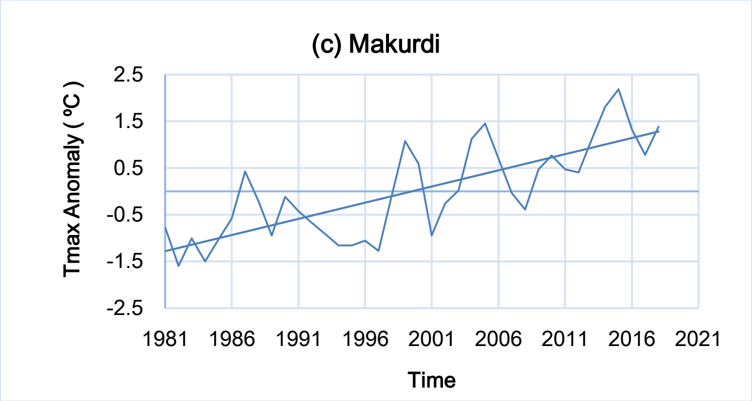

Fig. 14. Normalized time series anomaly plots for mean annual surface air maximum temperatures for representative stations (a: Ilorin, b: Minna and c: Makurdi) of the Guinea-wooded savanna eco-climatic zone

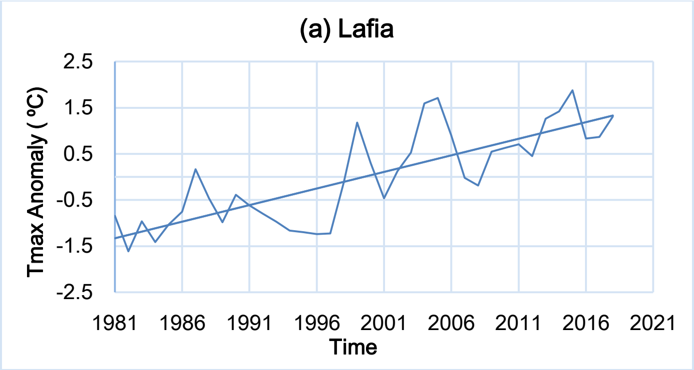

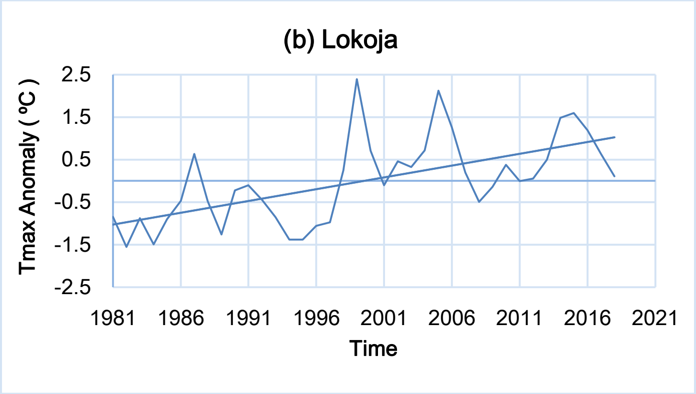

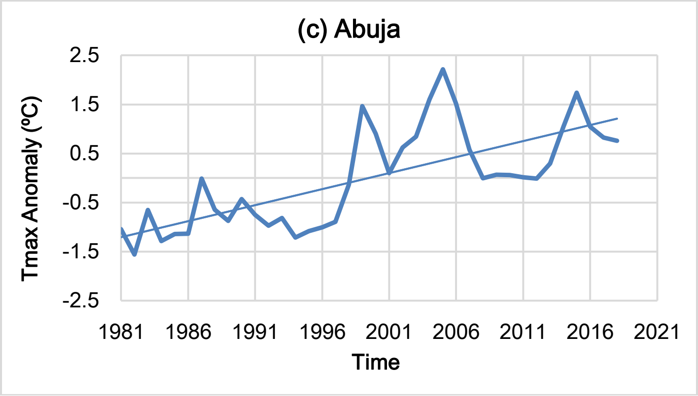

Fig. 15. Normalized time series anomaly plots for mean annual surface air maximum temperatures for representative stations (a: Lafia, b: Lokoja and c: Abuja) of the Sudan savanna eco-climatic zone

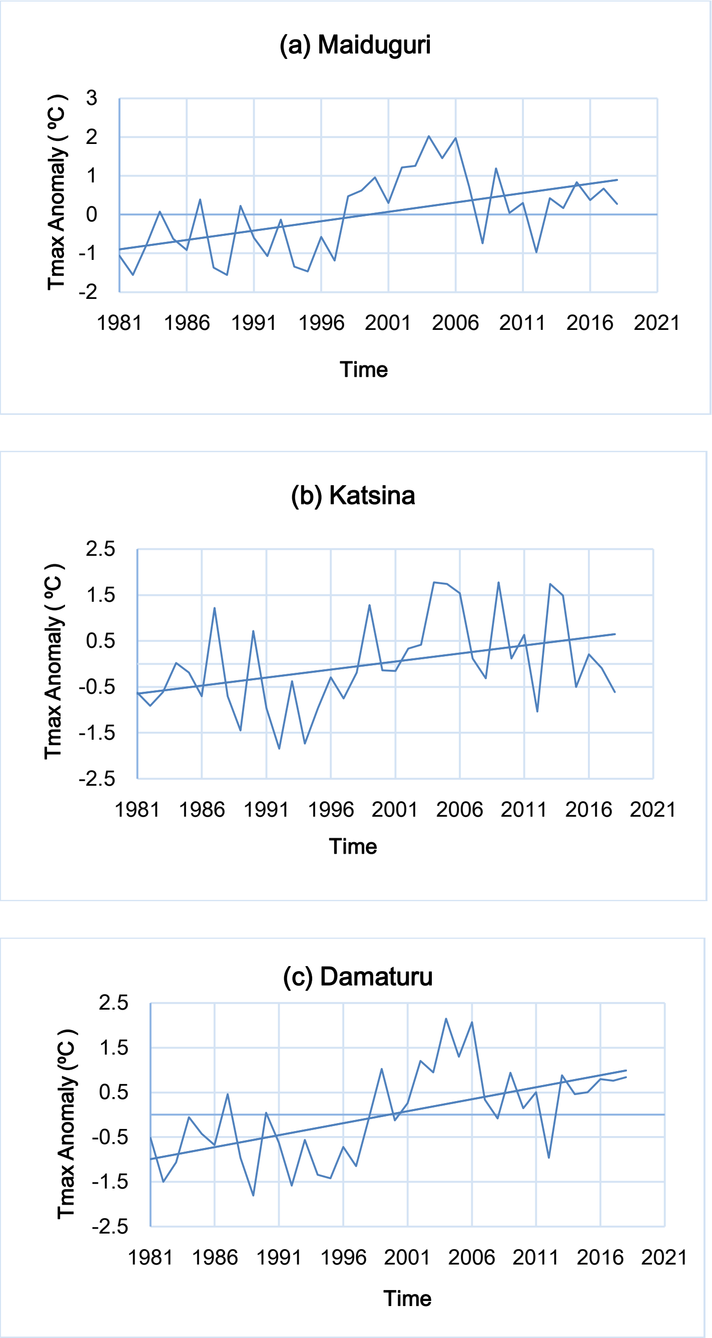

Fig. 16. Normalized time series anomaly plots for mean annual surface air maximum temperatures for representative stations (a: Maiduguri, b: Katsina and c: Damaturu) of the Sahel savanna eco-climatic zone

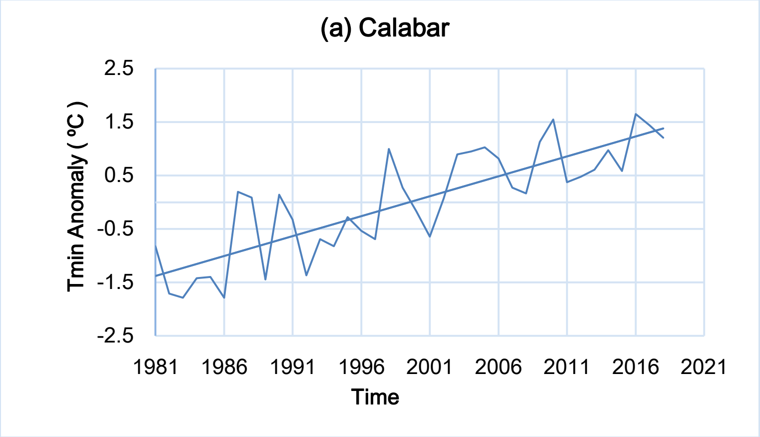
(a) Calabar

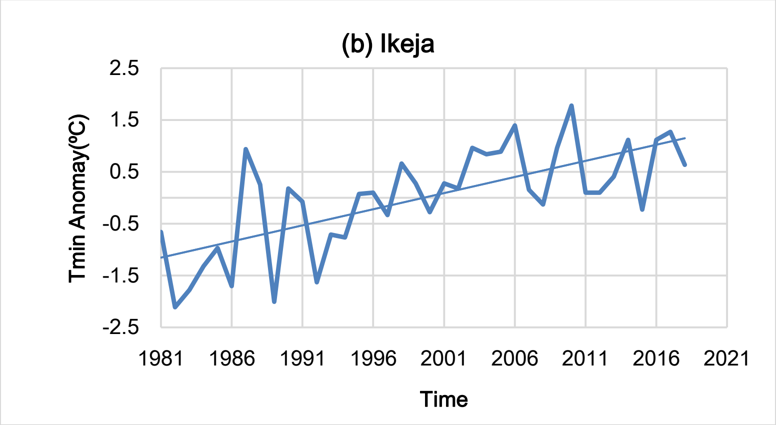
(b) Ikeja

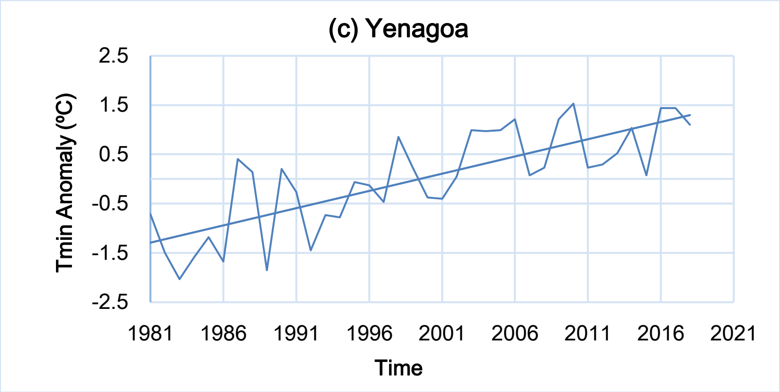
(c) Yenagoa

Fig. 17. Normalized time series anomaly plots for mean annual surface air minimum temperatures for representative stations (a: Calabar, b: Ikeja and c: Yenagoa) of the Mangrove-swamp rainforest eco-climatic zone

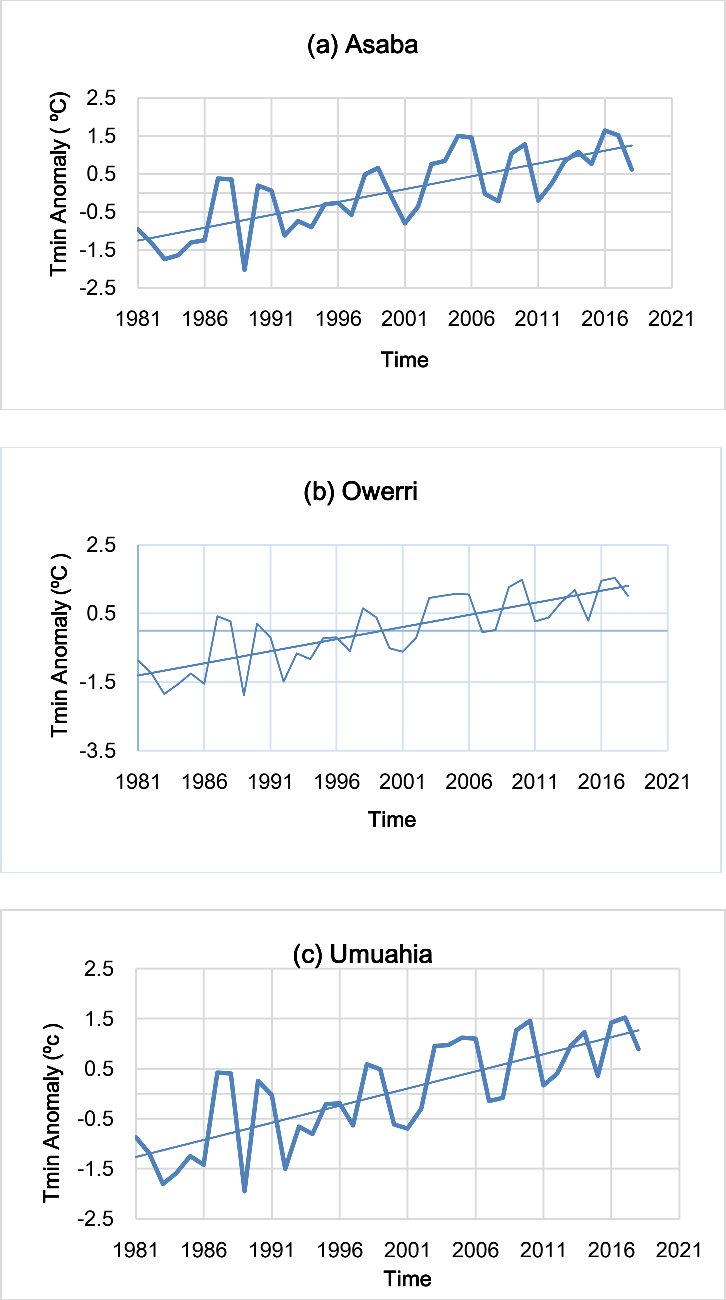

Fig. 18. Normalized time series anomaly plots for mean annual surface air minimum temperatures for representative stations (a: Asaba, b: Owerri and c: Umuahia) of the Tropical rainforest eco-climatic zone

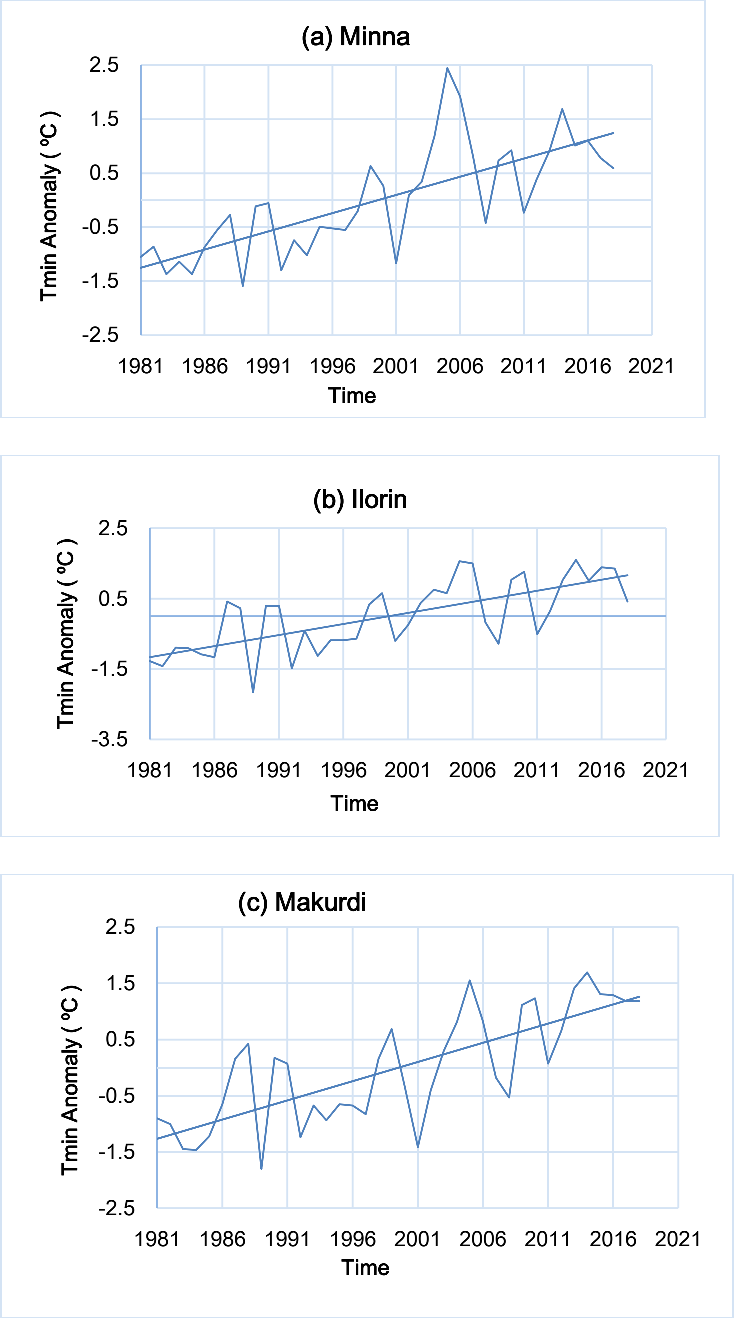

Fig. 19. Normalized time series anomaly plots for mean annual surface air minimum temperatures for representative stations (a: Minna, b: Ilorin and c: Makurdi) of the Guinea-wooded savanna eco-climatic zone

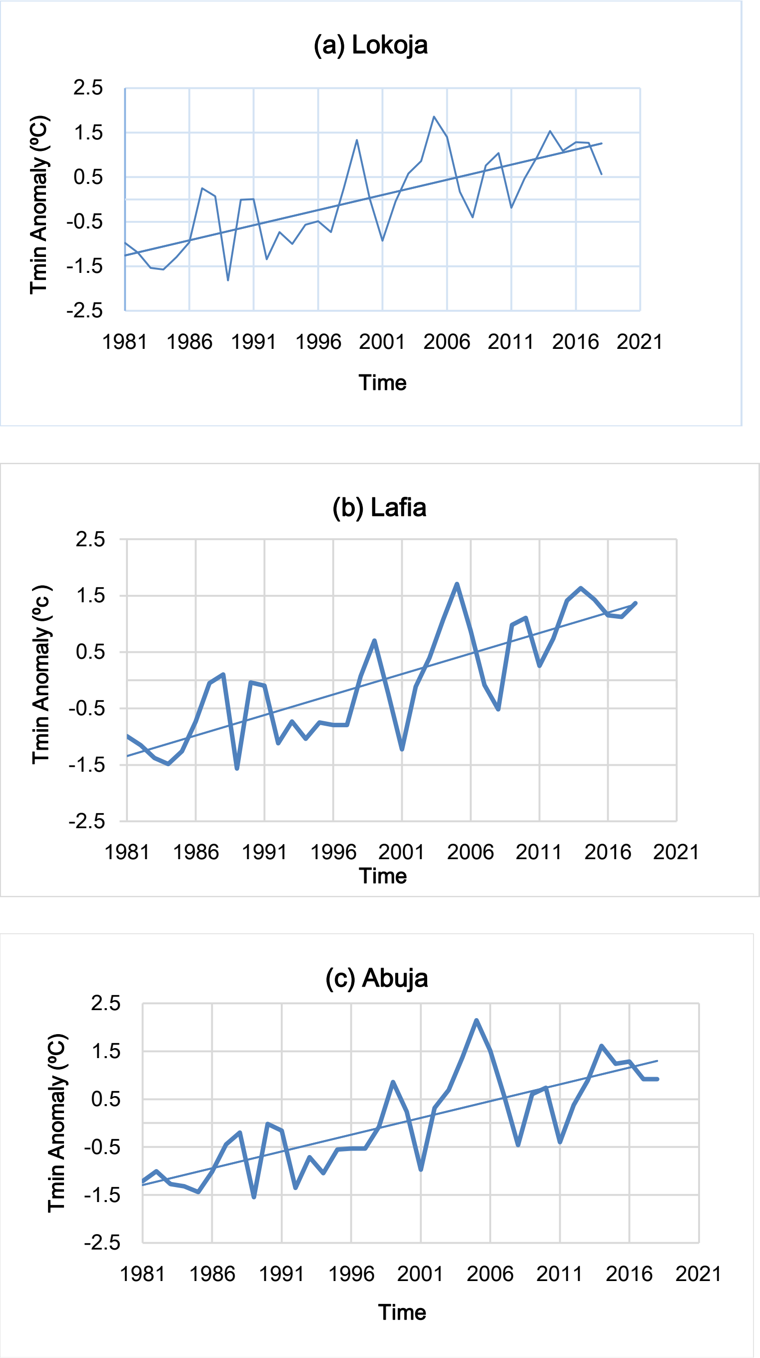

Fig. 20. Normalized time series anomaly plots for mean annual surface air minimum temperatures for representative stations (a: Lokoja, b: Lafia and c: Abuja) of the Sudan savanna eco-climatic zone

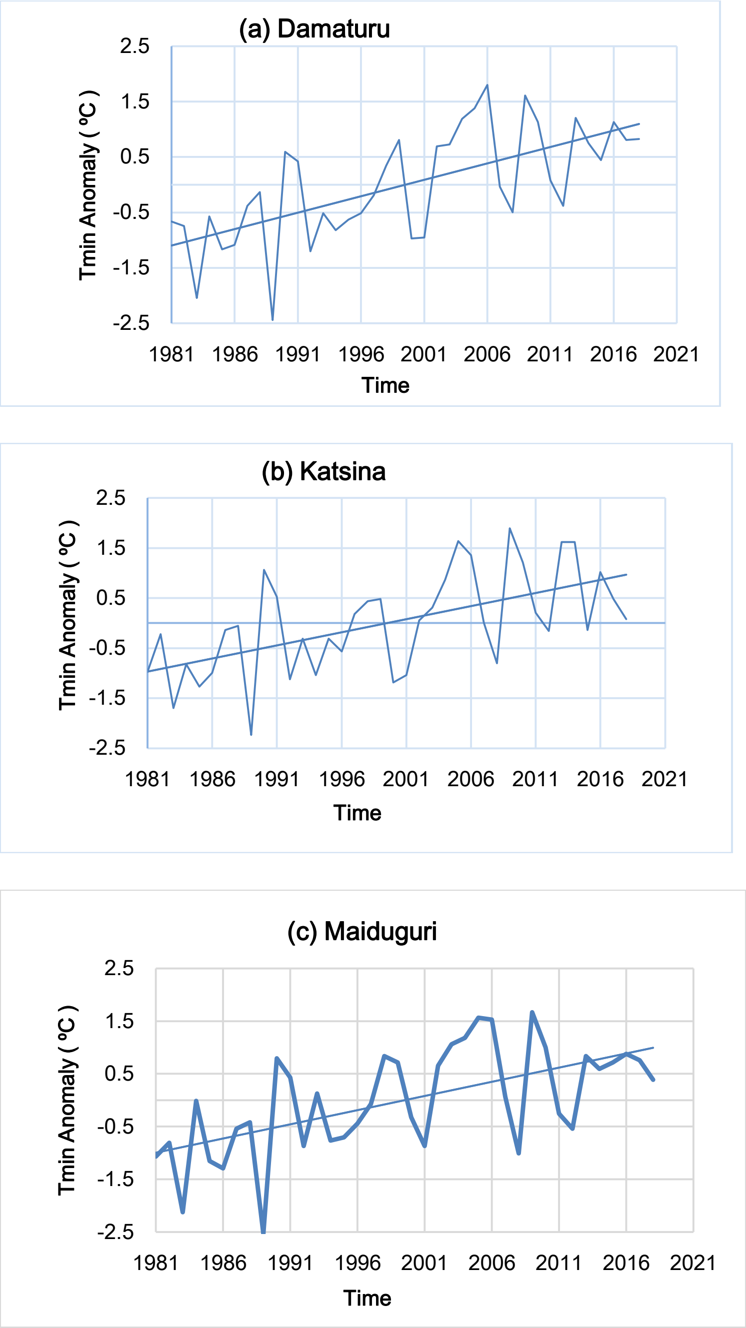

Fig. 21. Normalized time series anomaly plots for mean annual surface air minimum temperatures for representative stations (a: Damaturu, b: Katsina and c: Maiduguri) of the Sahel savanna eco-climatic zone

Discussion

The historical records of the studied variables showed long-term monotonic trends. The highlights of the findings are hereby presented.

Results of the analysis of the descriptive statistical features of surface air maximum and minimum temperatures are shown in Tables 2 and 3, respectively.

According to Durdu [50], the surface air temperature having a coefficient of variation (CV) of about <=0.1 (or 10%) indicates low variability. A CV of 0.1<CV<0.4 indicates moderate variability, and a high variability has a CV>0.4 (or 40%). Analysis of the coefficients of variation in Table 2 shows that mean annual surface air maximum temperatures in the Mangrove-swamp rainforest showed low variability, while that of the Tropical rainforest and the savannas (the Guinea-wooded, Sudan and the Sahel) showed moderate variability. Similarly, analysis of the coefficients of variation in Table 3 shows that mean annual surface air minimum temperature showed moderate variability in the eco-climatic zones in Nigeria covered by this study.

The variability of mean annual surface air maximum and minimum temperatures across the representative stations follow a well-defined pattern. Mean annual surface air maximum temperatures showed latitudinal dependence and are generally higher in the north and decreases towards the South in Nigeria (Table 2). Similarly, mean annual surface air minimum temperatures also showed latitudinal dependence, and are generally lower in the north, increasing towards the south in Nigeria (Table 3). This result is consistent with the findings of Aiyelabagan [51] that the maximum surface air temperature increases towards the north while the minimum surface air temperature decreases towards the north in Nigeria. This pattern of higher north-south coefficient of variation infers that surface air temperatures are more stable in the south than in the north. The nighttime cooling in the humid south is minimal due to radiative forcing from clouds, whereas the nighttime cooling in the drier north is substantial under cloudless skies.

Analysis of the coefficients of skewness in Table 2 shows that the mean annual values of surface air maximum temperatures for the 15 stations are above the central maximum for the data distribution. Similarly, analysis of the coefficients of skewness in Table 3 shows that the mean annual values of surface air minimum temperatures for 10 stations are below the central maximum and the mean annual values for 5 stations are above the central maximum for the data distribution.

Analysis of Figures 2~6 shows that mean monthly surface air maximum temperature varies seasonally along a well-defined pattern. Moving northward, the monthly mean maximum surface temperature begins to rise in January, reaches a maximum in March or April, and then gradually decreases, reaching a minimum in August. A rise to maximum values in October or November is observed again after August, dropping gently to a minimum value in December. In the South, the mean monthly surface air maximum temperature increases from January to peak at maximum values in February or March. During July or August, the values drop to their lowest values and then rise again to their maximum values during November or December. The maximum values observed around March is a consequence of increased surface air temperatures due to the arrival of insolation rather than in June to August when the on-set of the cool monsoon air lowers surface air temperatures. Similarly, the analysis of Figures 7~11 shows that the variation of mean monthly surface air minimum temperatures across the representative stations also follows a well-defined trend. The highest values in mean monthly surface air minimum temperatures are seen in April and May in the northern parts of Nigeria. In the South, the highest values in mean monthly surface air minimum temperatures are observed in March and April. Both sides of latitude 9°N, the lowest values in mean monthly surface air minimum temperatures record are observed in December and January. About this time, the Nigerian landscape is majorly under the influence of the Northeast trade wind and its associated air mass (*i.e.*, the Tropical Continental Air mass). Amadi *et al.* [17] notes that weather phenomena (such as early morning fog and mist) are associated with the dynamic processes of the trade wind due to radiation cooling at night under clear skies. Hence, low night temperatures characterize this period.

According to King *et al.* [33], the trend analysis of mean annual surface air maximum temperatures in Tables 4 and 5 reveals that 14 stations have monotonic upward trends in mean annual surface air maximum temperature. However, Ikeja shows a monotonic downward trend as observed by the negative value of the Mann-Kendall's test statistic (S). The highest value in the M-K test statistic for mean annual surface air maximum temperature was observed in Lafia, while the lowest value was observed in Ilorin. The M-K coefficients of time trend (*i.e.,* Kendall's tau b) for mean annual surface air maximum temperature for 12 stations are statistically significant at the 99% confidence interval (*i.e.,* 0.01 significance level) and one station (*i.e.*, Katsina) is statistically at the 0.05 significance level.

The trend analysis of mean annual surface air minimum temperatures in Tables 6 and 7 shows that all the stations have monotonic upward trends in mean annual surface air minimum temperature [33]. The highest value was observed in Calabar, while Katsina revealed the lowest value. The trends for all the stations are statistically significant at the 0.01 significance level as revealed by the coefficients of time trends values. Comparing data in Table 4 with Table 6, it was observed that mean annual surface air minimum temperature has a higher change rate than the mean annual surface air maximum temperature.

The findings of this study's trend analysis agree with the findings of Oguntunde *et al.* [28] that the mean annual surface air minimum temperature has a higher rate of change than the mean annual surface air maximum temperature. Majority of the stations in the Guinea-wooded (*i.e.,* Makurdi and Minna), Sudan (Abuja, Lafia and Lokoja) and Sahel savanna (*i.e.,* Maiduguri and Damaturu) zones have higher trend magnitudes. The highest trend magnitude in mean annual surface air maximum temperature is noticeable in Lafia (*i.e.,* 0.073 °C/year), while the lowest value was noticeable in Yenagoa (*i.e.,* 0.015 °C/year). The highest trend magnitude in mean annual surface air minimum temperature was noticeable in Abuja (*i.e.,* 0.069 °C/year) while the lowest value is noticeable in Katsina and Ikeja (*i.e.,* 0.024 °C/year).

According to King *et al.* [33], the mean estimated trend magnitude increase for mean annual surface air maximum temperature in Nigeria is about 0.035 °C/year and about 0.036 °C/year for the mean annual surface air minimum temperature. Thus, this study gives an estimated mean trend magnitude increase in mean annual surface air temperature of about 0.036 °C/year (*i.e.,*0.36 °C/decade) and an estimated mean annual surface air temperature increase in Nigeria of about 1.4°C from 1981-2018.

The normalized chronologically ordered anomaly plots for mean annual surface air maximum temperature show monotonic upward trends in 14 stations (Figures 12~ 16). Extreme temperature events (such as that of 1998) are shown in some of the standardized anomaly time series plots (*i.e.,* Calabar, Owerri, Umuahia and Yenagoa). No significant long-term trends were observed in Ikeja (Figure 12b) and Ilorin (Figure 14a). The results of the plots align with the M-K and the linear trend tests results (Tables 4 and 5, respectively).

Similarly, the normalized chronologically ordered anomaly plots for the mean annual surface air minimum temperature showing monotonic upward trends in all the 15 stations were observed (Figure 17~21). The standardized anomaly time series plots also display the years with records of extreme events in mean annual surface air minimum temperatures during the period of this study. All the station's time series plots depict monotonic trends that align with the results of the M-K and the linear trend tests (Tables 6 and 7, respectively). The plots for the mean annual surface air temperatures depict chronologically ordered meteorological observations of surface air temperatures for the period covered by this study. The increasing trend in the annual mean maximum and minimum surface temperatures is shown by the Sen's slope (Tables 4 and 6) and the linear trend tests (Tables 5 and 7).

The combined use of more than one method to analyze the trends in mean annual surface air temperatures in Nigeria from 1981 to 2018 aligns with the findings of [40, 41]. According to them, proper care should be taken to arrive at correct interpretation of data and test assumptions during trend analysis using statistical tests. Those conclusions should be made by using more than one statistical test, as each statistical test addresses a specific question.

According to King *et al*. [33], increasing population, urbanization, increased evapotranspiration rates, severe drought, deforestation and desertification may be culpable for the high trend magnitudes in surface air temperature observed in the Guinea-wooded, Sudan and Sahel savannas. The study also pointed out that the trend magnitude and direction is in line with that of Akinsanola & Ogunjobi [27], who reported an increase of about 0.036 °C/year in mean surface air temperatures and upward trends in most stations in Nigeria, a decreasing g trend of about -0.02°C in Jos over the period 1971-2000 and a decreasing mean surface air temperature trend in Ikeja and Oshodi from 1991-2000. The same authors pointed out that the trend aligns with the result of Abiodun *et al.* [20], who found a trend in rising surface air temperature in Nigeria which are statistically significant at the 0.05 level of significance from 1971 to 2000.

King *et al.* [33] also pointed out that the trends observed in this study are partially consistent with the findings of [17]. They found that the annual mean surface maximum and minimum temperatures in Nigeria showed an increasing trend, which was statistically significant at the 0.05 and 0.01 significance levels. In most of the stations included in this study, the trend was statistically monotonic. The annual mean surface maximum temperature in Ilorin showed a decreasing trend, but the trend was not significant, while the annual mean surface maximum and minimum temperatures in Ikeja showed a significant monotonic increasing trend. The authors note that the difference in the maximum surface temperature results for Ilorin may be due to the difference in data length, while the difference in the annual average maximum surface temperature results for Ikeja may be due to the accumulation of a layer of air in the atmosphere over Ikeja, which tends to weaken the intensity of solar radiation reaching the Earth's surface but captures thermal infrared radiation emitted from the Earth's surface at night. The authors suggested that this may be culpable for the reducing surface air maximum temperature but increasing surface air minimum temperature observed in Ikeja. Therefore, further studies should be carried out to unravel the cause of the downward trend in surface air maximum temperature observed in Ikeja

CONCLUSIONS

This study aimed at analyzing the trend and variations in mean annual surface air temperatures across selected representative stations of some eco-climatic zones in Nigeria and the possible causes of the trend and variations. Mean annual surface air maximum temperatures in the Mangrove-swamp rainforest showed low variability, while that of the Tropical rainforest and the savannas (the Guinea-wooded, Sudan and the Sahel) showed moderate variability. Similarly, mean annual surface air minimum temperature showed moderate variability in the eco-climatic zones in Nigeria covered by this study. Surface air maximum and minimum temperatures mean annual conditions showed strong latitudinal dependence. The study revealed monotonic upward trends significant at the 99% and 95% confidence intervals across the representative stations whose estimated mean trend magnitude increase over the 38-year period is 1.3°C and 1.4°C for mean annual surface air maximum and minimum temperatures respectively. The estimated mean trend magnitude increases for mean annual surface air temperature in Nigeria is about 1.4°C for the period 1981-2018.

With an estimated increase in mean trend magnitude of about 0.035 °C/year for mean annual surface air maximum temperature and an estimated increase in mean trend magnitude in mean annual surface air minimum temperature of about 0.036 °C/year, the estimated mean magnitude increase for both mean annual surface air maximum and minimum temperatures is about 0.036 °C/year. This study, also gives a projected estimated mean linear trend magnitude increase of about 4.3°C in mean surface air temperature by year 2100 in Nigeria.

The observed trend and variations in this study indicates changes in the net balance between the incoming solar and the outgoing thermal infrared radiation from the earth's surface and the lower atmosphere due to the radiative forcing caused by increasing concentrations of greenhouse gases (GHG's) and aerosols, land surface properties changes, urbanization and increasing population.

The significant long-term trends in the mean annual surface air temperatures at 0.01 and 0.05 significance levels over the period covered by this study provides a strong evidence that the climate of Nigeria is witnessing a possible human-induced climate change and a strong tendency for the on-set of climate-related hazards and their resulting adverse impacts. The results have serious implications for Nigeria. There is cogent need to devise appropriate and adequate mitigation and adaptive strategies by the relevant authorities; so that potential problems could be tackled before they become critical.

ACKNOWLEDGMENTS

The authors acknowledge the positive contribution of the National Aeronautics and Space Administration (NASA) for providing the reanalysis data.

CONFLICTS OF INTEREST

The authors declare that they have no known competing financial interests or personal relationships that could have appeared to influence the work reported in this paper.

REFERENCES

1. IPCC, (2002). *Climate Change 2001: The Scientific basis*, Cambridge. Cambridge University Press.
2. Malhi, Y. & Wright, J. (2004). Spatial patterns and recent trends in the climate of tropical rainforest regions. *Philosophical Transactions of Royal Society of London, (4), 359*, 311 – 329.
3. IPCC, (2007). Summary for Policymakers. In: *Climate Change 2007: The Physical Science Basis. Contribution of Working Group I to the Fourth Assessment Report of the Intergovernmental Panel on Climate Change*. Cambridge University Press, Cambridge.
4. IPCC, (2019). Summary for Policymakers. In: *Climate Change and Land: an IPCC special report on climate change, desertification, land degradation, sustainable land management, food security, and greenhouse gas fluxes in terrestrial ecosystems.* Cambridge University Press, Cambridge.
5. Meissner, K. J., Weaver, A. J., Matthews, H. D. & Cox, P. M. (2003). The role of land surface dynamics in glacial inception: A study with the UVic Earth System Model. *Climate Dynamics*, *21*(7–8), 515–537. https://doi.org/10.1007/s00382-003-0352-2
6. Snyder, P. K., Delire, C. & Foley, J. A. (2004). Evaluating the influence of different vegetation biomes on the global climate. *Climate Dynamics*, *23*(3–4), 279–302.
7. Dang, H., Gillett, N. P., Weaver, A. J., & Zwiers, F. W. (2007). Climate change detection over different land surface vegetation classes. *International Journal of Climatology*, *27*(2), 211–220.
8. Verma, S., Prakash, D., Srivastava, A. K. & Payra, S. (2017). Radiative forcing estimation of aerosols at an urban site near the thar desert using ground-based remote sensing measurements. *Aerosol Air Quality Research, 17:* 1294–1304.
9. Fawole, O. G., Cai, X., Pinker, R. T. & Mackenzie, A. R. (2019). Analysis of radiative properties and direct radiative forcing estimates of dominant aerosol clusters over an urban-desert region in West Africa. *Aerosol and Air Quality Research*, *19*(1), 38–48.
10. Liousse, C., Assamoi, E., Criqui, P., Granier, C. & Rosset, R. (2014). Explosive growth in African combustion emissions from 2005 to 2030. *Environmental Research Letter, 9,* 035003.
11. Liousse, C., Galy-Lacaux, C., Ndiaye, S. A., Diop, B., Ouafo, M., Assamoi, E. M., Gardrat, E., Castera, P., Rosset, R. & Akpo, A. (2012). Real time black carbon measurements in West and Central Africa urban sites. *Atmos. Environ. 54,* 529–537.
12. Mahmood, R., Pielke, R. A. & Hubbard, K. G. (2013). Land cover changes and their biogeophysical effects on climate. *International Journal of Climatology*, *34*(4), 929–953.
13. Yue, S. & Hashino, M. (2003). Long term trends of annual and monthly precipitation in Japan. *Journal of American Water Resources Association, 39*(3), 587 – 596.
14. De Luís, M., Raventós, J., González-Hidalgo, J. C., Sánchez, J. R. & Cortina, J. (2000). Spatial analysis of rainfall trends in the region of valencia (East Spain). *International Journal of Climatology*, *20*(12), 1451–1469.

15. Vincente-Serrano, S. M. (2006). Spatial and temporal analysis of droughts in the Iberian Peninsula, (1910-2000). *Hydrological Sciences Journal, 51(*1), 83-97.
16. Ewona, I. O. & Udo, S. O. (2008). Trend studies of some meteorological parameters in Calabar, Nigeria. *Nigerian Journal of Physics, 20*(2)*,* 283-289.
17. Amadi, S. O., Udo, S. O. & Ewona, I. O. (2014). Trend and Variation of Monthly Mean Minimum and Maximum temperature data over Nigeria for the period 1950-2012. *International Journal of Pure and Applied Physics, 2*(4), 1-27.
18. Subarna, D. (2017). Analysis of Long-Term Temperature Trend as an Urban Climate Change Indicator. *Forum Geografi*, *31*(2), 196–208.
19. Wang, J., Xu, C., Hu, M., Li, Q., Yan, Z., & Jones, P. (2018). Global land surface air temperature dynamics since 1880. *International Journal of Climatology, 38*(S1), e466-e474. doi:https://doi.org/10.1002/joc.5384
20. Abiodun, B. J., Salami, A. T. & Tadross, M. (2011). *Climate Change Scenarios for Nigeria: Understanding the Biophysical lmpacts.* A Report by the Climate Systems Analysis Group, Cape Town, for Building Nigeria's Response to Climate Change (BNRCC) Project, lbadan, Nigeria.
21. Thomas, T., Sudheer, K. P., Ghosh, N. C. & Gunte, S. S. (2013). Spatio-temporal variation of temperature characteristics over Narmada basin - is the consistent warming trend a possible climate change signal? *Proceedings - 20th International Congress on Modelling and Simulation, MODSIM 2013*, *December*, 2416–2422.
22. Magawata, U. Z., & Yahaya, A. A. (2019). Trends and Variations of Monthly Solar Radiation, Temperature and Rainfall Data over Birnin Kebbi Metropolis for the Period of 2014-2016. *Journal of Geography, Environment and Earth Science International*, *21*(4), 1–10.
23. Peterson, T. C &Vose, R. S. (1997). An overview of the global historical climatology network temperature database. Bull. *American Met. Soc., 78*(12), 2837 – 2849.
24. Abatzoglou, J. T., Redmond, K. T., & Edwards, L. M. (2009). Classification of regional climate variability in the state of California. *Journal of Applied Meteorology and Climatology*, *48*(8), 1527–1541.
25. Liu, X., Yin, Z. Y., Shao, X., & Qin, N. (2006). Temporal trends and variability of daily maximum and minimum, extreme temperature events, and growing season length over the eastern and central Tibetan Plateau during 1961-2003. *Journal of Geophysical Research Atmospheres*, *111*(19), 1–19. https://doi.org/10.1029/2005JD006915
26. Abudaya, M. (2013). Seasonal & Spatial Variation in Sea Surface temperature in the South-East Mediterranean Sea. *Journal of Environmental and Earth Science, 3*(2), 42 – 52.
27. Akinsanola, A. A. & Ogunjobi, K. O. (2014). Analysis of rainfall and temperatures variability over Nigeria, 1971-2000. *Global Journal of Human-Social Science B Geography, Geo-sciences, Environmental Disaster Management, 14(3)*, 1-18.
28. Oguntunde, P. G., Abiodun, B. J. & Lischeid, G. (2012). Spatial and temporal temperature trends in Nigeria, 1901-2000. *Meteorology and Atmospheric Physics*, *118*(1–2), 95–105. https://doi.org/10.1007/s00703-012-0199-3
29. Ogolo, E. O. & Adeyemi, B. (2009). Variation and trends of some meteorological parameters at lbadan, Nigeria. *The Pacific Journal of Science and Technology, 10*(2), 981 – 989.

30. Ewona, I. O. & Udo, S. O. (2011). Climatic parameters of Calabar as typified by some meteorological parameters. *Global Journal of Pure and Applied Sciences, 17(*1), 81-86.
31. Oruoye, E. D. (2014). An assessment of the trends of climatic variables in Taraba State, Nigeria. *Global Journal of Science Frontier Research: H Environment & Earth Science, 14*(4), 1-13.
32. Agbo, E. P., & Ekpo, C. M. (2021). Trend Analysis of the Variations of Ambient Temperature Using Mann-Kendall Test and Sen's Estimate in Calabar, Southern Nigeria. *Journal of Physics: Conference Series, 1734*(1), 012016. doi:10.1088/1742-6596/1734/1/012016
33. King, L. E., Udo, S. O., Ewona, I. O., Amadi, S. O., Ebong, E. D., & Umoh, M. D. (2024). Assessment of Temporal Trend in Surface Air Temperatures across Some Selected Eco-Climatic Zones in Nigeria. *Trends in Renewable Energy, 10*, 132-158. doi: http://dx.doi.org/10.17737/tre.2024.10.1.00169
34. Adefolalu, A. D. (2002). Climate of Nigeria. *In Atlas of Nigeria, (65)*, Paris: Les Editions J.A.
35. Gelaro, R., McCarty, W., Suárez, M. J., Todling, R., Molod, A., Takacs, L., Randles, C. A., Darmenov, A., Bosilovich, M. G., Reichle, R., Wargan, K., Coy, L., Cullather, R., Draper, C., Akella, S., Buchard, V., Conaty, A., da Silva, A. M., Gu, W. & Zhao, B. (2017). The modern-era retrospective analysis for research and applications, version 2 (MERRA-2). *Journal of Climate*, *30*(14), 5419–5454.
36. Rienecker, M. M. & Coauthors, G. (2008). *The GEOS-5 Data Assimilation System-Documentation of versions 5.0.1,5.1.0 and 5.2.0.T technical Report series on Global Modeling and Data Assimilation, vol.27,* NASA TECH REP. NASA/TM-2008-104606,118pp.
37. Molod, A., Takacs, L., Suarez, M., & Bacmeister, J. (2015). Development of the GEOS-5 atmospheric general circulation model: evolution from MERRA to MERRA2. *Geosci. Model Dev., 8*(5), 1339-1356. doi: http://dx.doi.org/10.5194/gmd-8-1339-2015
38. Wu, W. S., Purser, R. J., & Parrish, D. F. (2002). Three-dimensional variational analysis with spatially inhomogeneous covariances. *Monthly Weather Review, 130*(12), 2905-2916.
39. Longobardi, A. & Villani, P. (2009). Trend analysis of annual and seasonal rainfall time series in the Mediterranean area. *International Journal of Climatology, 12*(4), 23-31.
40. Kundzewicz, Z. W., & Robson, A. J. (2004). Change detection in hydrological records - A review of the methodology. *Hydrological Sciences Journal*, *49*(1), 7–19. https://doi.org/10.1623/hysj.49.1.7.53993
41. Sonali, P., & Nagesh Kumar, D. (2013). Review of trend detection methods and their application to detect temperature changes in India. *Journal of Hydrology, 476*, 212-227. doi:https://doi.org/10.1016/j.jhydrol.2012.10.034
42. Rossi, R. E., Mulla, D. J., Journel, A. G., & Franz, E. H. (1992). Geostatistical tools for modeling and interpreting ecological spatial dependence. *Ecological Monographs*, *62*(2), 277–314. https://doi.org/10.2307/2937096
43. Turkes, M. (1999). Vulnerability of Turkey to desertification with respect to precipitation and aridity conditions. *Tr. Journal of Engineering and Environmental Sciences, 23,* 363 – 380.
44. Helsel, D. R., Hirsch, R. M., Ryberg, K. R., Archfield, S. A., & Gilroy, E. J.

(2020). Statistical methods in water resources techniques and methods 4 – A3. *USGS Techniques and Methods, 1*(13), 15-25.
45. Houghton, R. A. (2003). Revised estimates of the annual net flux of carbon to the atmosphere from changes in land use and land management 1850-2000. *Tellus, Series B: Chemical and Physical Meteorology*, *55*(2), 378–390.
46. Yue, S. & Wang, C.Y. (2004). The Mann-Kendall test modified by effective sample size to detect trend in serially correlated hydrological series. *Water Resources Management, 3*, 201-218.
47. Wang, H., Zhang, M., Zhu, H., Dang, X., Yang, Z. & Yin, L. (2012). Hydro-climatic trends in the last 50 years in the lower reach of the Shiyang River Basin, NW China. *Catena*, *95*(51509001), 33–41.
48. Rai, R. K., Upadhhyay, A. & Ojha, C. S. P. (2010). Temporal variability of climatic parameters of Yumuna River Basin: Spatial analysis of persistence, trend and periodicity. *The Open Hydrology Journal, 4,* 184-210.
49. Sen, P. K. (1968). Estimates of the regression coefficient based on Kendall's tau. *Journal of American Statistic Association, 63*, 1379–1389.
50. Durdu, O. F. (2009): Effects of Climate Change on Water Resources of the Buyuk Menderes River Basin; WesternTurkey. *Turkish. Journal of Agriculture. 34,* 319–332.
51. Aiyelabagan, A. T. (2014). Latitudinal dependence of some meteorological parameters in Nigeria. *International Journal of Technical Research and Application, 2(*6), 7-10.

Trends in Renewable Energy
OPEN ACCESS ISSN: 2376-2144
Peer-Reviewed Review Article futureenergysp.com/index.php/tre

A Review of Nanofluid Boiling Heat Transfer and Its Applications in Heat Pipes

Xinyu Wang*, Ya Li

School of Mechanical Engineering, North China University of Water Resources and Electric Power, Zhengzhou, Henan 450045, CHINA

Received May 9, 2024; Accepted May 29, 2024; Published June 6, 2024

Nanofluid is a new type of heat transfer medium formed by adding metal or non-metal in liquid medium in a certain proportion and manner, which has many advantages over the traditional working fluid. Combining heat pipes with nanofluids and using nanofluids as the working material of heat pipes can reduce thermal resistance and effectively improve the heat transfer performance of heat pipes. This paper provides a relevant overview of heat pipes and nanofluids, and introduces the relevant classifications of heat pipes, the working principle and the relevant research on nanofluid-enhanced boiling heat transfer. It conducts a literature review on the application of nanofluids in heat pipes, and finally proposes possible future research directions.

Key Words: Boiling heat exchange; Heat pipe; Nanofluid; Classification; Working principle

Introduction

Heat pipe (HP) is an efficient heat transfer device, where the high thermal conductivity of a heat pipe allows it to transfer a higher amount of heat compared to conventional materials for the same area. Since the theory of the heat pipe principle was first proposed in 1944 by Gaugler [1] of General Motors, Ohio, USA. It was not until 1964 that Grover *et al.* [2] first introduced the concept of the heat pipe, made a simple heat pipe, and experimentally proved that the thermal conductivity of the heat pipe far exceeded that of any known metal. Since then, the research of heat pipe technology has attracted a large number of researchers, and the theory and application of heat pipes have shown a high-speed development trend. Immediately after, Cotter [3] proposed a simplified heat pipe model and conducted experimental research on the velocity of steam and liquid in the heat pipe, which greatly improved the consistency of heat management theory between the heat transfer limit part and the workpiece pressure. In 1967, American scientists first successfully applied heat pipes to spacecraft cooling [4]. Since then, countries around the world have increased their investment in heat pipe research, and heat pipe technology has made great progress. Nowadays, heat pipes have many applications in the fields of computers, automotive engineering, medicine, aerospace engineering, traffic engineering, etc., and have become one of the main energy-saving and emission-reduction utilization tools.

Heat pipe (HP) is a passive cooling device that, in most cases, does not consume any external energy [5]. In addition to being widely used in various fields due to its high thermal conductivity and excellent isothermal properties, the heat pipe also has unique features such as compact structure, low mass, low noise, and no transmission element.

**Corresponding author:* 1278792329@qq.com

Tr Ren Energy, 2024, Vol.10, No.2, 210-228. doi: 10.17737/tre.2024.10.2.00174

Factors affecting the heat transfer performance of the heat pipe include the inner and outer diameter size of the heat pipe, the heat pipe material, the length of the evaporation section, the adiabatic section and the condensation section, the thermal properties of the working fluid, the liquid filling rate, etc. [6].

A heat pipe is an element that utilizes a phase change for efficient heat transfer, and usually consists of a shell, a suction core, and an internal working fluid. The suction core portion (a porous capillary material immediately adjacent to the tube wall), which is the core component that facilitates antigravity heat transfer, is available in sintered, grooved, and reticulated types. It provides a capillary force to drive the closed circulation of the working fluid and also serves as an interface for use in liquid-gas phase changes [7]. As can be seen from the working principle diagrams of axial flat plate heat pipe in Fig. 1 and radial flat plate heat pipe in Fig. 2, according to the construction of the heat pipe, the working part of the heat pipe can be divided into three parts: evaporation section, condensation section and adiabatic section. The evaporation section is generally in direct contact with the heat source, the wall and the heat source through the role of thermal conductivity between the heat transfer to the tube mass, so that the temperature of the mass increases to reach the boiling point of evaporation. Adiabatic section has two roles, first of all, with the evaporation of the mass of heat from the evaporation section to the condensing section for the transfer of heat, and secondly, the adiabatic section can be in contact with the evaporation section of the heat source and the condensing section of the cold source of isolation, which makes the heat pipe can be made into the various types of shapes that we need to meet a variety of working conditions. There is no heat exchange between the working fluid and the outside world in the adiabatic section, so the adiabatic section, as a mass transport path, is also called the transport section [8]. After the evaporation, the workpiece flows to the condensing section. The condensation section dissipates the heat carried by the workpiece through cooling paths such as convection heat transfer. The workpiece in the tube changes from gas to liquid, and the heat in the tube is also taken away. After the workpiece in the tube is liquefied, it flows along the tube wall and condenses into water droplets, which flow back to the evaporation section under the action of capillary pressure [9]. The normal operation of the heat pipe will have a closed cycle of evaporation of liquid, flow of high temperature vapor, condensation of vapor, and condensation of the work mass into a liquid reflux, which is the reason why the heat pipe can be regarded as a superconductor of heat [10].

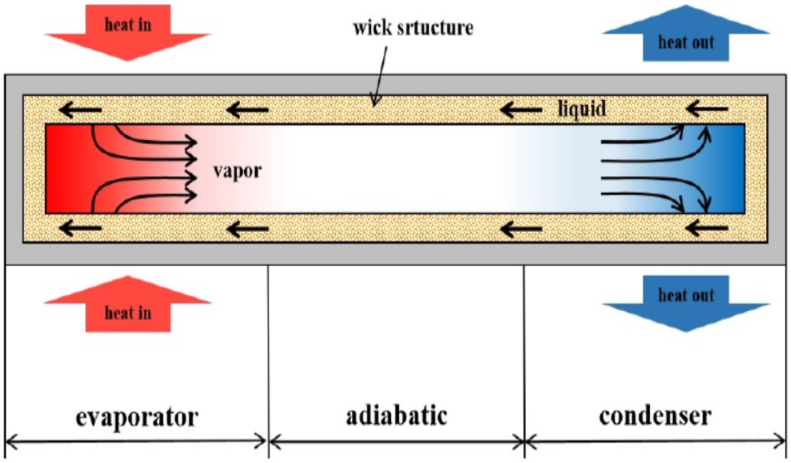

Fig. 1. Working principle diagram of axial flat heat pipe

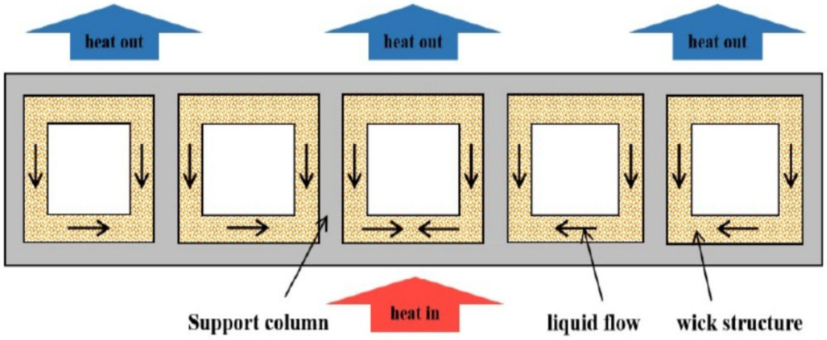

Fig. 2. Schematic Diagram of Working Principle of Radial Flat Heat Pipe

Nanofluid is a colloidal nanoscale suspended liquid formed by adding metallic or non-metallic nanoparticles with an average diameter of less than 100 nm, dispersed in a certain proportion into liquid media such as water, motor oil or ethylene glycol [11]. The thermal conductivity of metal and non-metal nanoparticles can reach dozens or even hundreds of thousands times that of pure liquid materials. According to the comparison table of thermal conductivity of common substances (Table 1), it can be seen that at room temperature, the thermal conductivity of carbon nanotubes is about 7.5 times that of copper, 37.5 times that of iron, 4,893 times that of pure water, and 11,718 times that of ethylene glycol. Therefore, adding nanoparticles to pure liquid to form nanofluid can significantly improve the thermal conductivity of the liquid, and it is not easy to wear and clog the instrument. These excellent properties have made a large number of scholars at home and abroad have invested in the study of nanofluids. Nanofluid technology has gradually been used in the fields of chemical industry, energy, aerospace, shipbuilding, automobile, air conditioning and refrigeration, electronics, computers and so on. Especially, nanofluids show broad application prospects in the field of enhanced heat transfer [12].

Table 1. Comparison table of thermal conductivity of common substances.

Materialistic	**Densities (g/cm^3)**	**Thermal conductivity (W/(m·K))**
Carbon nanotube	1.2	3000
Purified water	0.998	0.613
Ethylene glycol	1.11	0.256
Oil	0.88	0.145
Iron	7.86	80
Copper	8.92	401

Advantages of nanofluidic media over other media include: 1. Compared with millimetre and micrometre particles, nanoparticles are smaller in size and lighter in mass. Due to the small size effect of nanoparticles and their strong Brownian motion, their behaviour is closer to that of liquid molecules and less prone to wear and clogging. Therefore compared to liquids with millimetre or micron sized particles added, nanofluids have more potential for practical applications [13]. 2. The small size of nanoparticles can be used in microelectronics and micro heat pipes and other micro heat exchangers. 3. Nanofluids make the flow boundaries of the flow layer disrupted due to inter-particle, particle-liquid, particle-wall interactions, which results in a reduction of the thermal resistance and an enhancement of the heat transfer. 4. The surface area and heat capacity of nanoparticles are much larger than that of millimetre or micron-sized particles when the same volume share of solids is added to the fluid. Accordingly, the available heat transfer surface area of nanoparticles is larger and the thermal conductivity is greater.

For enhanced heat transfer in heat pipe, since the main heat transfer mechanism of heat pipe is boiling heat transfer, the improvement of boiling performance will improve the heat transfer performance of heat pipe [14]. It has been shown that the thermal conductivity of nanofluids is much larger than that of pure fluids, while nanofluids are outstanding in improving the performance of boiling heat transfer. Therefore, the application of nanofluids to heat pipes to improve the heat transfer efficiency of the heat pipe also came into being, nanofluids, a new type of work material combined with heat pipes can significantly improve the heat transfer efficiency of the heat pipe. Nanofluid heat pipe combines the advantages of both, and has a broader application prospect in the field of heat transfer, which is of great significance [15].

Boiling Heat Transfer Theory

The heat transfer process when the liquid boils on the heating surface is a two-phase flow heat transfer characterized by a phase change. The latent heat generated by the internal phase change of the liquid carries away a large amount of heat [16]. Boiling heat transfer mainly consists of two forms: 1. Large vessel boiling (also known as pool boiling) refers to boiling above the saturation temperature of the hot wall immersed in a liquid with a free surface [17]. 2. Flow boiling is also known as boiling in the tube, in which the fluid is heated by the hot wall in the process of flow. The flow of fluid can be a natural circulation, or the forced circulation by the pump drive [18].

Flow boiling differs from pool boiling in that the fluid is heated while it is flowing. The heat transfer zones of flow boiling in tubes mainly include single-phase liquid convection zone, nucleate boiling zone, liquid film forced convection zone and single-phase steam convection zone. Figure 3 shows the schematic diagram of the pipeline flow boiling bubble formation process: The single-phase liquid convection zone is when the fluid just enters the pipe. The fluid is heated by the hot wall of the pipe but has not yet reached the saturation temperature. The bubbles generated are difficult to break away from the pipe wall, but grow by sliding along the pipe wall. The nucleate boiling zone refers to the period when the mainstream temperature of the fluid reaches the saturation temperature and the bubbles generated no longer condense and disappear. After the nucleate boiling zone is the liquid film forced convection zone. The characteristic of this zone is that no bubbles are generated on the wall and a liquid film is formed on the wall. In the nucleate boiling region and the liquid film forced convection region, the wall temperature remains basically unchanged, and the fluid is always at the saturation temperature. As the liquid film attached to the wall evaporates, all the liquid turns into steam. After the fluid temperature leaves the saturation temperature, it begins to rise rapidly. At this time, the wall temperature in the single-phase steam convection zone also rises accordingly [19].

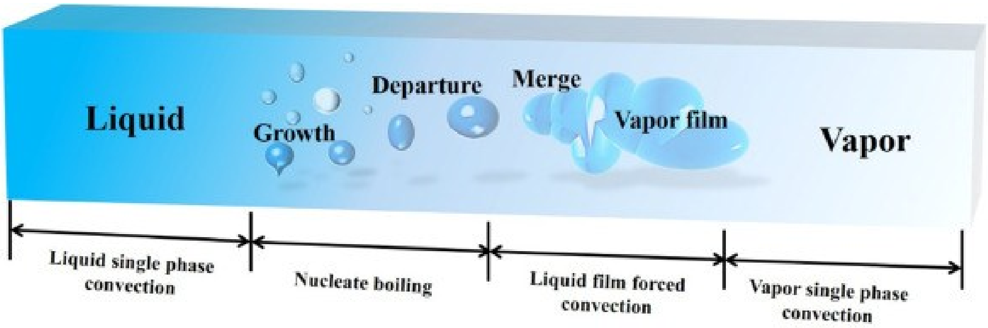

Fig. 3. Flow boiling bubble formation process diagram in the pipeline [16]

To study pool boiling, it is first necessary to analyze the heat transfer curves related to pool boiling. It can be seen from the pool boiling heat transfer curve in Figure 4 that the pool boiling process mainly includes four heat transfer zones: natural convection zone, nucleate boiling zone, transition boiling zone and film boiling zone. Point A is the boiling start point (ONB). Before point A, there are no bubbles on the heating surface, and heat transfer is carried out in the form of thermal conduction. The heat transfer performance is weak, and this area is the natural convection zone. Later, point A is the nucleate boiling area, and bubbles begin to form on the heated surface. The generation and detachment of bubbles cause strong disturbances, which greatly improves the convective heat transfer coefficient. At this time, it can be seen from Figure 4 that the heat flux density begins to rise rapidly, but the wall temperature does not increase much. The maximum value of the heat flux at point C is the critical heat flux (CHF), also known as the burnout heat flux. In actual work, in order to prevent the equipment wall temperature from rising rapidly and burning after reaching the critical heat flux density, the deviation from nucleate boiling point (DNB) is often used as the maximum heat flux density point. After point C, when the wall temperature continues to rise, the bubbles cannot fall off in time, resulting in a layer of steam film covering the heating surface. Due to the relatively low thermal conductivity of steam, the heat transfer resistance increases and the heat flux density is in a decreasing state. Due to the low thermal conductivity of steam, the heat transfer resistance increases and the heat flux density is in a reduced state. This area is the transition boiling zone. When the heating surface is completely covered by the steam film, the heat flux reaches the q_{min} point. As the wall temperature further increases, the radiation heat transfer is enhanced, the heat flux rises again, and then enters the stable film boiling zone [20].

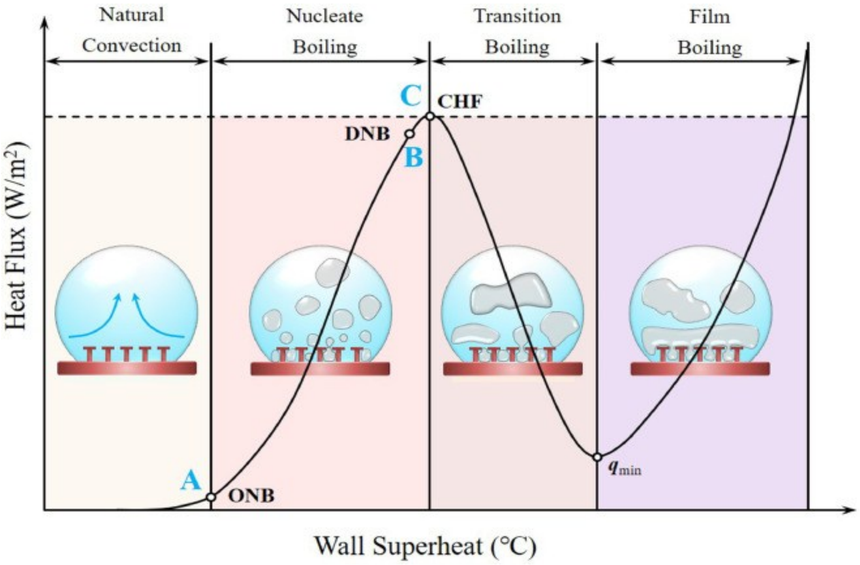

Fig. 4. Pool boiling curve [16]

Case Studies of Nanofluid-Based Boiling Heat Transfer

He *et al.* [21] conducted a boiling heat transfer study on two nanofluids made of zinc oxide (ZnO) nanoparticles dissolved in deionized water and ethylene glycol, respectively, in a cylindrical vessel. The results showed that the increase in heat flux leads to a significant increase in the heat transfer coefficient of the nanofluids.

Sharma & Unune [22] enhanced pool boiling performance by using silver (Ag)/zinc oxide (ZnO) nanofluids at concentrations of 0.02%, 0.06% and 0.1% on three heater surfaces by using the electro discharge machining (EDM) method. The results showed that the critical heat flow density (CHF) and heat transfer coefficient of the surfaces containing silver/ZnO nanofluids at a concentration of 0.1% increased by 80.43% and 252.98%, respectively, compared to the combination of deionized water and normal surfaces. It can also be concluded that the EDM method increased the nucleation sites, and the deposition of the nanoparticles lowered the contact angle of the surfaces, and the performance of pool boiling was enhanced.

Ramakrishna *et al.* [23] compared the pool boiling critical heat flow density (CHF) of nanofluids with copper oxide (CuO) nanoparticles with deionized water. The results showed that the optimum volume fraction of copper oxide nanoparticles was 0.2%, while the critical heat flow density of copper oxide nanofluids with volume fractions ranging from 0.01% to 0.5% were elevated higher than 60% compared to deionized water.

Karimzadehkhouei *et al.* [24] conducted pool boiling heat transfer experiments on a flat plate using different concentrations of TiO_2 and CuO nanofluids and found that the enhancement effect of TiO_2 nanofluids on the boiling heat transfer decreases with the increase in concentration, but not with CuO nanofluids.

Xing *et al.* [25] experimentally investigated the pool boiling heat transfer coefficients of covalently and non-covalently functionalized multi-walled carbon nanotube nanofluids at different volumetric concentrations on a flat plate surface. The results showed that the maximum pool boiling heat transfer coefficient of covalently functionalized nanofluids increased up to 53.4% compared to conventional fluids.

The pool boiling phenomenon of aluminium trioxide (Al_2O_3) nanofluids with an average particle size of 10 nm on the surface of a copper sheet was investigated by Manetti *et al.* [26]. They investigated the pool boiling of aluminum oxide (Al_2O_3) nanofluid on a smooth surface with a surface roughness of Ra = 0.05 μm using aqueous Al_2O_3 nanofluids with volume concentrations of 0.0007% and 0.007%, respectively, and compared it with the pool boiling on a smooth surface with a surface roughness of Ra = 0.23 μm on a rough copper surface. The results show that the pool boiling heat transfer coefficients on smooth and rough copper surfaces increased by 75% and 15%, respectively, compared to deionized water for heat fluxes ranging from 100 to 800 kW/m^2.

Suriyawong & Wongwises [27] experimentally investigated the pool boiling heat transfer of titanium dioxide (TiO_2)-water (H_2O) nanofluids with volume concentrations of 0.00005%, 0.0001%, 0.0005%, 0.005%, and 0.01%, respectively, under two types of heating surfaces (*i.e.*, copper and aluminum tubes with different surface roughness). The results show that at a concentration of 0.0001 vol%, the heat transfer coefficient decreases for aluminum tubes as the heating surface and increases for copper tubes.

The flow boiling heat transfer of refrigerant nanofluid in a horizontal smooth tube was experimentally investigated by Hao *et al.* [28]. They used CuO nanofluid based on R113 refrigerant in which the mass fraction of CuO nanoparticles was 0~0.5 wt%. The results showed that the maximum enhancement in heat transfer coefficient of the refrigerant-based nanofluid was about 29.7% compared to the pure refrigerant.

Kim *et al.* [29] investigated the critical heat flow density (CHF) of aluminum trioxide (Al_2O_3) nanoparticles and reduced graphene oxide (RGO) nanofluids at atmospheric pressure using pool boiling experiments and compared it with deionized water. The results show that the CHF increases with concentration up to 54% for Al_2O_3 nanofluids at concentrations above 0.001 vol%. In RGO nanofluids with a concentration of 0.00005-0.005 vol%, the CHF enhancement ranges from 10%~37% with increasing concentration.

Wang & Su [30] investigated the flow-boiling heat transfer of γ-Al_2O_3/H_2O nanofluids in a vertical tube. The results show that for γ-Al_2O_3/H_2O nanofluids with an average particle size of 20 nm and volume concentrations of 0.1% and 0.5%, the flow boiling Nusselt number increases with the increase of surface heat flux, nanoparticle volume concentration and pressure, and the average Nusselt number of the two concentrations of nanofluids increases by 23% and 45%, respectively. Compared with deionized water, γ-Al_2O_3/H_2O nanofluids have an enhancing effect on flow boiling heat transfer, and the maximum enhancement rate can reach about 86%.

Current Research Status of Nanofluidic Heat Pipes

There are many ways to classify the heat pipe. According to the working temperature, the heat pipe can be divided into: low-temperature heat pipe (-273 ~ 0 °C), room temperature heat pipe (0 ~ 250 °C), medium-temperature heat pipe (250 ~ 450 °C), high-temperature heat pipe (450 ~ 1,000 °C) and so on. According to the structure form, it can be divided into traditional heat pipe, gravity heat pipe, loop heat pipe, pulsating heat pipe, flat plate heat pipe and so on. According to the different flow modes of the working fluid in the pipe, the heat pipe can be divided into thermal siphon heat pipe, oscillating heat pipe, and core heat pipe (mesh core heat pipe, sintered core heat pipe, and channel heat pipe) [31]. Combining the application and research of heat pipes by a large number of scholars, this article will mainly illustrate the four major types of heat pipes, namely loop heat pipes, gravity heat pipes, slot channel heat pipes and pulsating heat pipes, as relevant research examples.

Loop Heat Pipe

As shown in Figure 5, Loop Heat Pipe (LHP) refers to a loop closed-loop type heat pipe. It generally consists of an evaporator, condenser, vapor piping, liquid piping and a compensation chamber. The main driving force to induce liquid reflux is capillary force.

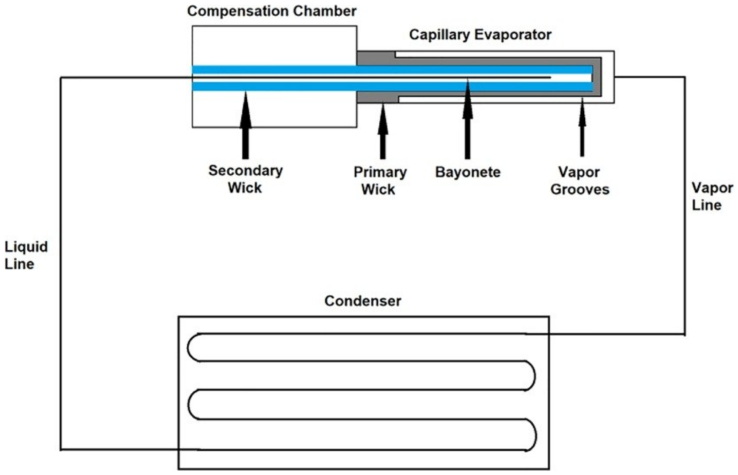

Fig. 5. Schematic Diagram of Loop Heat Pipe [32]

Tharayil *et al.* [33] applied nanofluids mixed with graphene and water to loop heat pipes. The results show that as the volume concentration of graphene nanofluid increases from 0.006 vol%, the thermal resistance of the loop heat pipe gradually decreases. Compared with pure water, at a concentration of 0.006 vol% and a heating power of 380 W, the thermal resistance of the loop heat pipe is reduced by 30.4% and the thermal efficiency is increased by 93%. Veeramachaneni *et al.* [34] applied graphene and water nanofluid to a copper loop heat pipe with a thermal load of 4~320 W and fluid filling ratio of 0.1-0.2% were experimentally investigated for copper and graphene hybrid nanofluid loop heat pipe. It has been shown that the thermal resistance reduction and thermal conductivity enhancement using 0.02 vol% (30% (Cu) + 70% (graphene)) hybrid nanofluidic phase is 24.42% and 32.4%, respectively, compared to deionized water. As shown in Figure 6, through experiments they concluded that in addition to the enhancement of the thermal conductivity of the fluid, the deposition of nanoparticles on the inner surface of the evaporator increases the effective heat transfer area of the evaporator and increases the boiling heat transfer nucleation sites, which is the main reason for the enhancement of the heat transfer performance of the loop heat pipe.

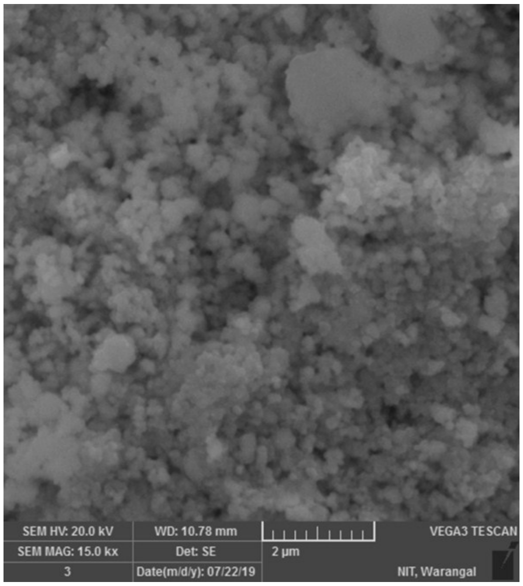

Fig. 6. The SEM image of Copper–GnP nanoparticles [34]

Thermosyphon Heat Pipe

Gravity heat pipes are also called thermosyphon heat pipes (THP). As shown in Figure 7, unlike traditional heat pipes, gravity acceleration needs to be applied, that is, the condensation section is placed directly below the condensate, and the condensate is refluxed by gravity. Therefore, gravity heat pipes do not require capillary structures, have a simpler structure, and have relatively low processing costs.

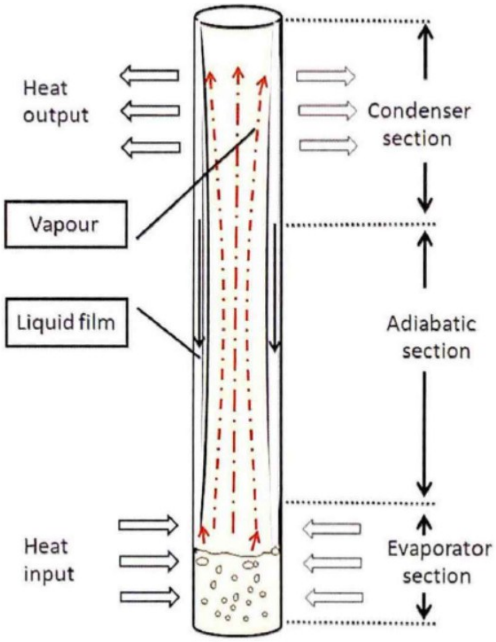

Fig. 7. Schematic Diagram of Gravity Heat Pipe

Çiftçi [35] conducted an experimental study on the heat transfer performance of gravity heat pipe with 2.0 vol% aluminum nitride and zinc oxide hybrid nanofluid in the range of 150-450 W heat load and the experimental setup is shown in Figure 8. The results show that (50% (Aluminium Nitride) + 50% (Zinc Oxide)) hybrid nanofluid has the best heat transfer performance at a thermal load of 150 W. The maximum thermal resistance is reduced by about 40.79%. The main reason for the improvement of heat transfer performance of heat pipes is that the suspended nanoparticles reduce the contact angle of the solid-liquid interface and the suspended nanoparticles perform Brownian motion in nucleation boiling and collide with large bubbles formed in the working fluid, causing a reduction in thermal resistance.

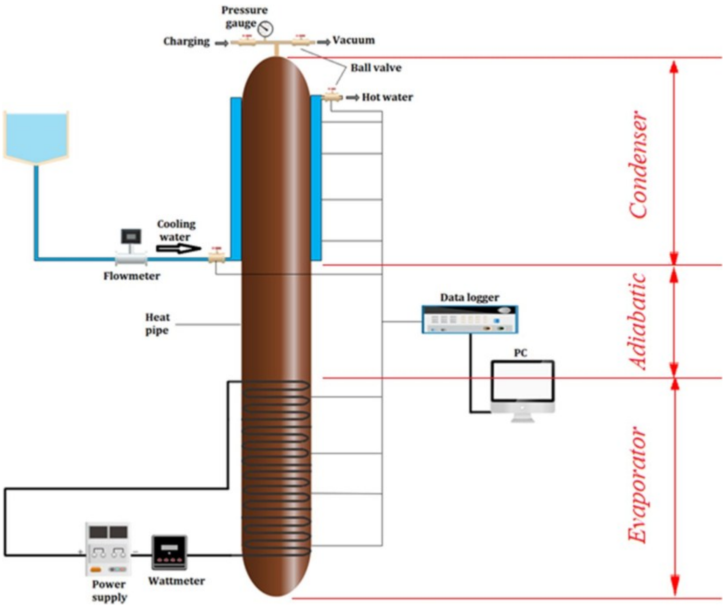

Fig. 8. Schematics of the heat pipe test rig [35]

Herrera *et al.* [36] visualized the boiling heat transfer performance of graphene nanofluid ring siphon heat pipes using inflated aluminum plates at 70% filling ratio, different heating powers (30 W, 60 W, 90 W), and concentrations (0.3 wt%, 0.5 wt%, 1 wt%). The results show that graphene nanofluid with a concentration of 0.5 wt% has a lower nucleation site for boiling heat transfer compared to pure water, indicating that the temperature reaches the boiling point faster. Furthermore, a portion of the graphene is deposited on the surface of the upper wall, which results in a clogging on the liquid surface. This affects the liquid level in the evaporation section to be lower than the liquid level in the condensation section. The lack of liquid in the upper heat source section resulted in an increase in thermal resistance as shown in Figure 10. When the concentration of graphene nanofluid was increased from 0.5 wt% to 1 wt%, the thermal resistance was significantly higher compared to the graphene nanofluid with a concentration of 0.5 wt% due to clogging as shown in Figure 11, despite the fact that more bubbles could be generated compared to pure water.

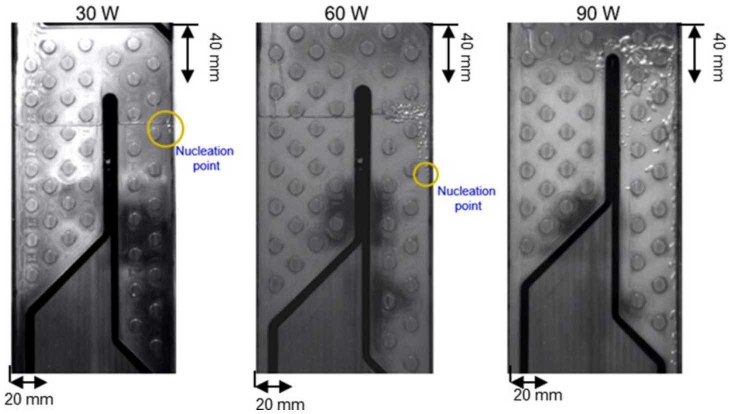

Fig. 9. (a) Pure water fluid visualisation for 30 W (b) 60 W (c) 90 W input power [36]

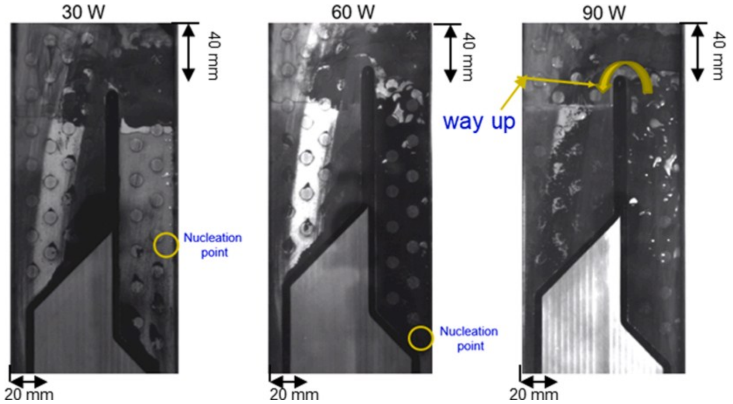

Fig. 10. (a) Visualisation of graphene nanofluid with a concentration of 0.5 wt% graphene nanofluid at 30 W (b) 60 W (c) 90 W input power [36]

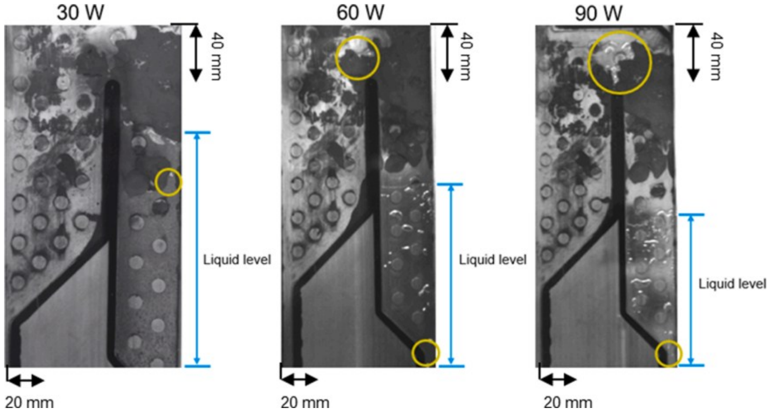

Fig. 11. (a) Visualisation of graphene nanofluid with 1 wt% graphene nanofluid concentration at 30 W (b) 60 W (c) 90 W input power [36]

Grooved Heat Pipe

Grooved Heat Pipe (GHP) is a heat pipe with suction core by capillary action of the groove structure on its inner wall surface, which makes the work mass flow spontaneously to the evaporation section. As shown in Figure 12, the rectangular grooved heat pipe cross-section is schematic, where δ is the heat pipe wall thickness and σ is the depth of the groove. Due to the existence of the slot channel structure, the heat transfer area inside the tube is increased, which greatly reduces the heat pipe thermal resistance. And because the vapor flows in the core of the tube, the liquid returns through the channel. The gas-liquid two phases basically do not have a carrying effect; it is more favorable to the heat pipe work than the gravity heat pipe.

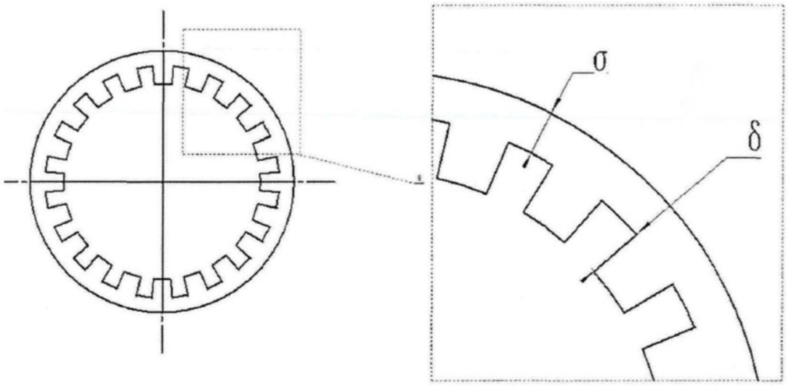

Fig. 12. Section Diagram of Channel Heat Pipe

Pandya *et al.* [37] investigated the heat transfer performance of axial fluted heat pipe with CeO_2-MWCNT hybrid nanofluid using numerical modeling method. The results showed that the best heat transfer performance of the fluted heat pipe was achieved when 1.25 vol% of hybrid nanofluid was used, with an enhancement of about 61.27% and a reduction in maximum thermal resistance of about 30% as compared to the base fluid. Liu *et al.* [38] investigated the heat transfer performance of a cylindrical micro fluted heat pipe using different types of nanofluids. The results showed that copper (Cu) nanofluids and copper oxide (CuO) nanofluids improved the heat transfer performance of the slot heat pipe. However, silicon oxide (SiO) nanofluid deteriorates the heat transfer performance. It was shown to be due to the different surface structure of the nanoparticles forming a coating on the inner surface of the evaporation section thereby weakening the boiling heat transfer performance of the evaporation section. As shown in Figure 13, the coating structure of Cu and CuO nanofluids is a compact porous structure formed by tightly aggregated nanoparticles, which is not easy to come off. However, the coating of SiO nanofluid appears to be a slurry layer without any porous reorganization layer and the coating is easily removed by water flushing. It can be seen that the surface structure formed by Cu and CuO nanoparticles provides a better capillary structure, while the slurry surface structure formed by SiO nanoparticles reduces its heat transfer performance.

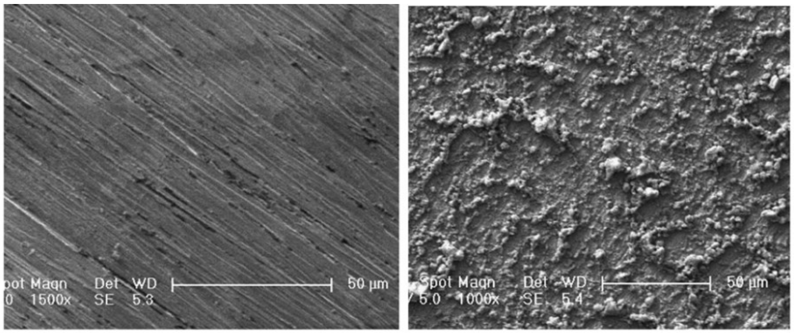

a water **b** 30 nm-SiO

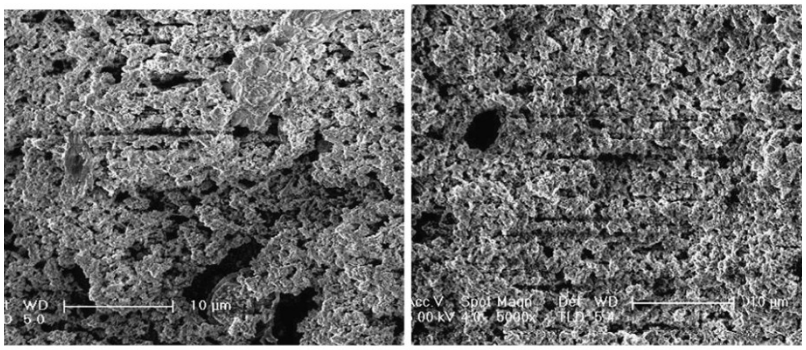

c 40 nm-Cu **d** 50 nm-CuO

Fig. 13. TEM of the coating layer after the test using CuO nanoflfluid [38]

Pulsating Heat Pipe

Pulsating heat pipe (PHP) (also known as oscillating heat pipe, self-excited oscillating flow heat pipe) is a unique new type of heat transfer element improved on the basis of ordinary heat pipe. Pulsating heat pipe is usually made of a long capillary tube bent into multiple elbows, which can be divided into closed, open and valve-closed pulsating heat pipes by observing the presence or absence of loop formation and one-way valves inside the pulsating heat pipe [39], and its structure is shown in Figure 14. The pulsating heat pipe has no capillary structure, and it is driven by the unbalanced pressure difference between the air plugs to return the liquid to form a loop.

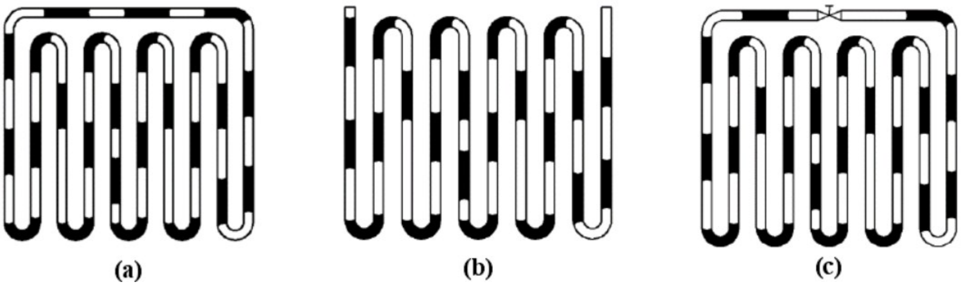

Fig. 14. (a) Closed pulsating heat pipe (b) Open pulsating heat pipe (c) Closed pulsating heat pipe with valve

Zhang *et al.* [40] used SiO_2-H_2O nanofluids with mass concentrations of 0.5%, 1.0%, 1.5% and 2.0%, respectively, to visualize the pulsating heat pipe employing the nanofluids using a high-speed camera. The results show that the addition of nanoparticles increases the transient driving force of the workpiece, promotes the phase change of the workpiece of the pulsating heat pipe, facilitates the condensate reflux, and the performance of the heat pipe is improved. As shown in Figure 15, the maximum heat transfer efficiency enhancement of the heat pipe can reach 40.1% at a heating power of 50 W and a concentration of 1.0 wt%.

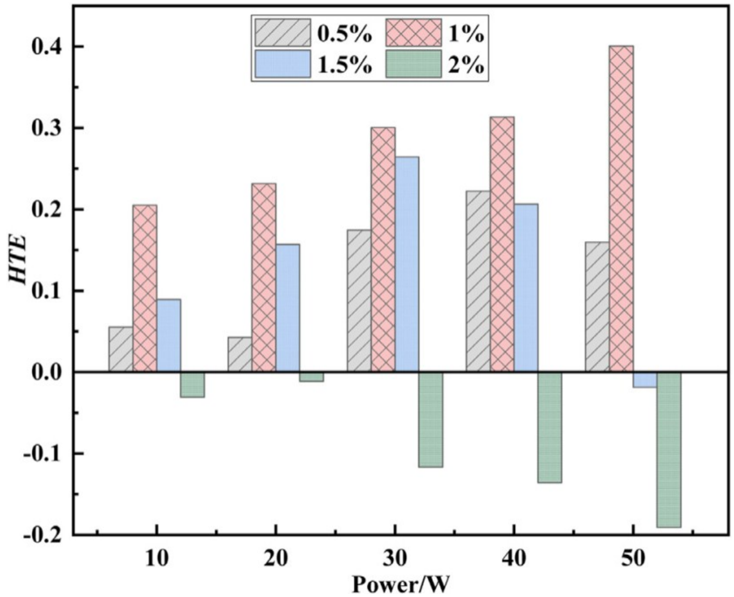

Fig. 15. The HTE Variation of PHP with different concentration [40]

Zhou *et al.* [41] used an ethanol-water solution of carbon nanotubes as the working fluid of an oscillating heat pipe and investigated the thermal resistance and heat transfer performance of the heat pipe. The results showed that the vertically oscillating heat pipe using carbon nanofluid had better startup and heat transfer performance compared to the oscillating heat pipe using ethanol-water mixture, and the wall temperature and thermal resistance were reduced by about 18.5% and 80.8%, respectively, by using 2 wt% carbon nanotube nanofluid in the heat pipe. From the transmission electron microscope image of the carbon nanotube nanofluid and the deposition of carbon nanotubes on the inner surface of the evaporator section (Figure 16), it can be seen that the thermal resistance of the heat pipe is reduced and the heat transfer performance is improved mainly due to the increase in thermal conductivity and the deposition of the carbon nanotube fibers on the surface of the evaporator, which increases the nucleation sites and enhances the boiling heat transfer.

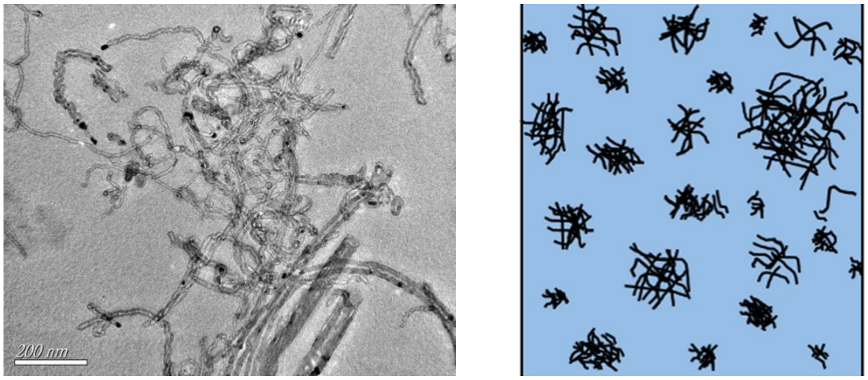

Fig. 16. (a) Schematic of CNT fibre deposition on the inner surface of the oscillating heat pipe

evaporator (b) Transmission electron microscopy image of a carbon nanotube nanofluid [41]

CONCLUSIONS

Heat pipe is an efficient heat transfer device, the high thermal conductivity of the heat pipe makes it possible to transfer higher heat compared to traditional materials, which has a wide range of application fields and great application potential. This paper provides a relevant review on the classification, working principle, application cases and nanofluid-enhanced boiling heat transfer and enhanced heat transfer performance of heat pipes. The open literature suggests that nanofluids show great potential for enhancing heat transfer in heat pipes.

Meanwhile, the research on nanofluid heat pipes has made great progress in recent years, but there is still much room for improvement, and many key problems need to be solved: 1. The measurement results of the thermal conductivity of nanofluids by different researchers lack consistency, so it is necessary to improve the corresponding research program and test system to facilitate more accurate measurement of the heat transfer coefficient of nanofluids. 2. The research on the heat transfer performance of heat pipes by nanofluids is mainly based on experiments, and the research on the mechanism of enhanced heat transfer after nanofluids are applied to heat pipes is not deep enough, and the theoretical analysis needs to be improved. 3. The current research on heat pipes with nanofluids is mainly focused on a single nanofluid, and the research on the application of mixed nanofluids to heat pipes is relatively small. 4. The cost of nanofluid preparation is high, and it is a priority to promote the research on nanofluids in the future to make nanofluid cheaper or to find the preparation method that saves the cost. 5. research on nanofluids is a priority.

CONFLICTS OF INTEREST

The authors declare that they have no known competing financial interests or personal relationships that could have appeared to influence the work reported in this paper.

REFERENCES

[1] Gaugler, R.S. (1942). *Heat transfer device*. U.S. Patent 2350348.

[2] Grover, G. M., Cotter, T. P., & Erickson, G. F. (1964). Structures of Very High Thermal Conductance. *Journal of Applied Physics, 35*(6), 1990-1991. doi: https://doi.org/10.1063/1.1713792

[3] Cotter, T. P. (1965). *THEORY OF HEAT PIPES*. Retrieved from United States: https://www.osti.gov/biblio/4619147. doi:https://doi.org/10.2172/4619147

[4] Tien, C. L., & Sun, K. H. (1971). Minimum meniscus radius of heat pipe wicking materials. *International Journal of Heat and Mass Transfer, 14*(11), 1853-1855. doi:https://doi.org/10.1016/0017-9310(71)90052-4

[5] Akachi, H. (1990). *Structure of a heat pipe*. U.S. Patent 4921041.

[6] Wang, C., Zhang, L., Liu, X., Tang, S., Qiu, S., & Su, G. H. (2020). Experimental study on startup performance of high temperature potassium heat pipe at different inclination angles and input powers for nuclear reactor application. *Annals of Nuclear Energy, 136*, 107051. doi:https://doi.org/10.1016/j.anucene.2019.107051

[7] Li, Y., He, H.-f., & Zeng, Z.-x. (2013). Evaporation and condensation heat transfer in a heat pipe with a sintered-grooved composite wick. *Applied Thermal Engineering, 50*(1), 342-351. doi:https://doi.org/10.1016/j.applthermaleng.2012.07.042

[8] Tang, H., Tang, Y., Wan, Z., Li, J., Yuan, W., Lu, L., . . . Tang, K. (2018). Review of applications and developments of ultra-thin micro heat pipes for electronic cooling. *Applied Energy, 223*, 383-400. doi:https://doi.org/10.1016/j.apenergy.2018.04.072

[9] Chen, J., Li, Z., Huang, W., Ma, Q., Li, A., Wang, B., . . . Jiang, F. (2024). Super-long gravity heat pipe geothermal space heating system: A practical case in Taiyuan, China. *Energy, 299*, 131521. doi:https://doi.org/10.1016/j.energy.2024.131521

[10] Li, D., Zhang, G. Q., Pan, K., Ma, X., Liu, L., & Cao, J. (2009). *Numerical simulation on heat pipe for high power LED multi-chip module packaging.* Paper presented at the 2009 International Conference on Electronic Packaging Technology & High Density Packaging.

[11] Alrowaili, Z. A., Ezzeldien, M., Shaaalan, N. M., Hussein, E., & Sharafeldin, M. A. (2022). Investigation of the effect of hybrid CuO-Cu/water nanofluid on the solar thermal energy storage system. *Journal of Energy Storage, 50*, 104675. doi:https://doi.org/10.1016/j.est.2022.104675

[12] Kanti, P. K., & Maiya, M. P. (2022). Rheology and thermal conductivity of graphene oxide and coal fly ash hybrid nanofluids for various particle mixture ratios for heat transfer applications: Experimental study. *International Communications in Heat and Mass Transfer, 138*, 106408. doi:https://doi.org/10.1016/j.icheatmasstransfer.2022.106408

[13] Zhou, L., Zhu, J., Zhao, Y., & Ma, H. (2022). A molecular dynamics study on thermal conductivity enhancement mechanism of nanofluids – Effect of nanoparticle aggregation. *International Journal of Heat and Mass Transfer, 183*, 122124. doi:https://doi.org/10.1016/j.ijheatmasstransfer.2021.122124

[14] Nazari, M. A., Ahmadi, M. H., Sadeghzadeh, M., Shafii, M. B., & Goodarzi, M. (2019). A review on application of nanofluid in various types of heat pipes. *Journal of Central South University*, *26*(5), 1021-1041.

[15] Ghorabaee, H., Emami, M. R. S., Moosakazemi, F., Karimi, N., Cheraghian, G., & Afrand, M. (2021). The use of nanofluids in thermosyphon heat pipe: A comprehensive review. *Powder Technology, 394*, 250-269. doi:https://doi.org/10.1016/j.powtec.2021.08.045

[16] Chu, H., Yu, X., Jiang, H., Wang, D., & Xu, N. (2023). Progress in enhanced pool boiling heat transfer on macro- and micro-structured surfaces. *International Journal of Heat and Mass Transfer, 200*, 123530. doi:https://doi.org/10.1016/j.ijheatmasstransfer.2022.123530

[17] Xu, N., Jiang, H., Peng, L., Wang, D., & Chu, H. (2021). Dynamic Analysis of Bubble Attachment and Sweeping on Microwire in Subcooled Nucleate Pool Boiling. *Journal of Thermal Science, 30*(5), 1842-1858. doi: https://doi.org/10.1007/s11630-021-1512-6

[18] Zhang, P., Wang, T., Jiang, Y., & Guo, C. (2023). Measurement of transient liquid film and its effect on flow boiling heat transfer in non-circular microchannels. *International Journal of Thermal Sciences, 184*, 108004. doi:https://doi.org/10.1016/j.ijthermalsci.2022.108004

[19] Jamialahmadi, M., Müller-Steinhagen, H., Abdollahi, H., & Shariati, A. (2008). Experimental and theoretical studies on subcooled flow boiling of pure liquids and multicomponent mixtures. *International Journal of Heat and Mass Transfer, 51*(9), 2482-2493. doi:https://doi.org/10.1016/j.ijheatmasstransfer.2007.07.052

[20] Pare, A., & Kumar Ghosh, S. (2022). The chronological study on parametric evolution of pool boiling with nanofluids: An experimental review. *Thermal Science and Engineering Progress, 34*, 101420. doi:https://doi.org/10.1016/j.tsep.2022.101420

[21] He, Y., Li, H., Hu, Y., Wang, X., & Zhu, J. (2016). Boiling heat transfer characteristics of ethylene glycol and water mixture based ZnO nanofluids in a cylindrical vessel. *International Journal of Heat and Mass Transfer, 98*, 611-615. doi: https://doi.org/10.1016/j.ijheatmasstransfer.2016.03.052

[22] Sharma, P. O., & Unune, D. R. (2022). Augmentation of pool boiling performance using Ag/ZnO hybrid nanofluid over EDM assisted robust heater surface modification. *Colloids and Surfaces A: Physicochemical and Engineering Aspects, 655*, 130150. doi: https://doi.org/10.1016/j.colsurfa.2022.130150

[23] Hegde, R. N., Rao, S. S., & Reddy, R. P. (2012). Investigations on heat transfer enhancement in pool boiling with water-CuO nano-fluids. *Journal of Thermal Science, 21*(2), 179-183. doi: https://doi.org/10.1007/s11630-012-0533-6

[24] Karimzadehkhouei, M., Shojaeian, M., Şendur, K., Mengüç, M. P., & Koşar, A. (2017). The effect of nanoparticle type and nanoparticle mass fraction on heat transfer enhancement in pool boiling. *International Journal of Heat and Mass Transfer, 109*, 157-166. doi:https://doi.org/10.1016/j.ijheatmasstransfer.2017.01.116

[25] Xing, M., Yu, J., & Wang, R. (2016). Effects of surface modification on the pool boiling heat transfer of MWNTs/water nanofluids. *International Journal of Heat and Mass Transfer, 103*, 914-919. doi:https://doi.org/10.1016/j.ijheatmasstransfer.2016.07.053

[26] Manetti, L. L., Stephen, M. T., Beck, P. A., & Cardoso, E. M. (2017). Evaluation of the heat transfer enhancement during pool boiling using low concentrations of Al2O3-water based nanofluid. *Experimental Thermal and Fluid Science, 87*, 191-200. doi:https://doi.org/10.1016/j.expthermflusci.2017.04.018

[27] Suriyawong, A., & Wongwises, S. (2010). Nucleate pool boiling heat transfer characteristics of TiO2–water nanofluids at very low concentrations. *Experimental Thermal and Fluid Science, 34*(8), 992-999. doi: https://doi.org/10.1016/j.expthermflusci.2010.03.002.

[28] Peng, H., Ding, G., Jiang, W., Hu, H., & Gao, Y. (2009). Heat transfer characteristics of refrigerant-based nanofluid flow boiling inside a horizontal smooth tube. *International Journal of Refrigeration, 32*(6), 1259-1270. doi:https://doi.org/10.1016/j.ijrefrig.2009.01.025

[29] Kim, J. H., Kim, J. M., Jerng, D. W., Kim, E. Y., & Ahn, H. S. (2018). Effect of aluminum oxide and reduced graphene oxide mixtures on critical heat flux enhancement. *International Journal of Heat and Mass Transfer, 116*, 858-870. doi:https://doi.org/10.1016/j.ijheatmasstransfer.2017.09.063

[30] Wang, Y., & Su, G. H. (2016). Experimental investigation on nanofluid flow boiling heat transfer in a vertical tube under different pressure conditions. *Experimental Thermal and Fluid Science, 77*, 116-123. doi:https://doi.org/10.1016/j.expthermflusci.2016.04.014

[31] Anand, R. S., Jawahar, C. P., Solomon, A. B., & Bellos, E. (2020). A review of experimental studies on cylindrical two-phase closed thermosyphon using refrigerant for low-temperature applications. *International Journal of Refrigeration, 120*, 296-313. doi:https://doi.org/10.1016/j.ijrefrig.2020.08.011

[32] Riehl, R. R., & Murshed, S. M. S. (2022). Performance evaluation of nanofluids in loop heat pipes and oscillating heat pipes. *International Journal of Thermofluids, 14*, 100147. doi:https://doi.org/10.1016/j.ijft.2022.100147

[33] Tharayil, T., Asirvatham, L. G., Dau, M. J., & Wongwises, S. (2017). Entropy generation analysis of a miniature loop heat pipe with graphene–water nanofluid: Thermodynamics model and experimental study. *International Journal of Heat and Mass Transfer, 106*, 407-421. doi:https://doi.org/10.1016/j.ijheatmasstransfer.2016.08.035

[34] Veeramachaneni, S., Pisipaty, S. K., Vedula, D. R., Solomon, A. B., & Harsha, V. S. (2022). Effect of copper–graphene hybrid nanoplatelets in a miniature loop heat pipe. *Journal of Thermal Analysis and Calorimetry, 147*(10), 5985-5999. doi: https://doi.org/10.1007/s10973-021-10873-5

[35] Çiftçi, E. (2021). Distilled Water-Based AlN + ZnO Binary Hybrid Nanofluid Utilization in a Heat Pipe and Investigation of Its Effects on Performance. *International Journal of Thermophysics, 42*(3), 38. doi: https://doi.org/10.1007/s10765-021-02792-2

[36] Herrera, B., Gallego, A., & Cacua, K. (2021). Experimental evaluation of a thermosyphon-based heat exchanger working with a graphene oxide (GO) nanofluid in a cogeneration system. *Thermal Science and Engineering Progress, 24*, 100949. doi:https://doi.org/10.1016/j.tsep.2021.100949

[37] Pandya, N. S., Desai, A. N., Kumar Tiwari, A., & Said, Z. (2021). Influence of the geometrical parameters and particle concentration levels of hybrid nanofluid on the thermal performance of axial grooved heat pipe. *Thermal Science and Engineering Progress, 21*, 100762. doi:https://doi.org/10.1016/j.tsep.2020.100762

[38] Liu, Z.-H., Li, Y.-Y., & Bao, R. (2011). Compositive effect of nanoparticle parameter on thermal performance of cylindrical micro-grooved heat pipe using nanofluids. *International Journal of Thermal Sciences, 50*(4), 558-568. doi:https://doi.org/10.1016/j.ijthermalsci.2010.11.013

[39] Han, X., Wang, X., Zheng, H., Xu, X., & Chen, G. (2016). Review of the development of pulsating heat pipe for heat dissipation. *Renewable and Sustainable Energy Reviews, 59*, 692-709. doi:https://doi.org/10.1016/j.rser.2015.12.350

[40] Zhang, D., He, Z., Guan, J., Tang, S., & Shen, C. (2022). Heat transfer and flow visualization of pulsating heat pipe with silica nanofluid: An experimental study. *International Journal of Heat and Mass Transfer, 183*, 122100. doi:https://doi.org/10.1016/j.ijheatmasstransfer.2021.122100

[41] Zhou, Z., Lv, Y., Qu, J., Sun, Q., & Grachev, D. (2021). Performance evaluation of hybrid oscillating heat pipe with carbon nanotube nanofluids for electric vehicle battery cooling. *Applied Thermal Engineering, 196*, 117300. doi:https://doi.org/10.1016/j.applthermaleng.2021.117300

Trends in Renewable Energy
OPEN ACCESS ISSN: 2376-2144
Peer-Reviewed Review Article
futureenergysp.com/index.php/tre

Application and Characteristics of Hydrogen in Alternative Fuels for Internal Combustion Engines

Mengfei Liu

North China University of Water Resources and Electric Power, Zhengzhou City, No. 36, Beihuan Road, Henan, China

Received May 8, 2024; Accepted June 3, 2024; Published June 22, 2024

Petroleum has been used as the power source for internal combustion engines for hundreds of years. Nowadays, the problems of fossil energy shortage and environmental pollution are becoming increasingly serious. In response to China's carbon neutrality strategy, it is urgent to seek alternative fuels that can replace petroleum as the power source of internal combustion engines. The challenges of alternative fuels include reducing post-combustion pollutant emissions and being able to recycle them while maintaining the original engine performance. Using hydrogen as fuel can reduce automobile exhaust emissions, promote the development of hydrogen internal combustion engines, and achieve sustainable social and economic development. This article reviews the ideality of hydrogen as an alternative fuel for internal combustion engines and the combustion characteristics of hydrogen internal combustion engines. The bottleneck problems (such as abnormal combustion, NO_x emission control and power recovery) that need to be solved urgently in the development of hydrogen internal combustion engines are pointed out. It's found that these problems can be solved by the combination of software simulation and experimental verification in practice.

Keywords: *Hydrogen energy; Internal combustion engine; Substitute fuels; Combustion characteristics; Emission characteristics*

Introduction

China is a country rich in coal but poor in oil, and also a country with an increasing number of motor vehicles. With the rapid development of the automobile industry and the widespread use of internal combustion engines, fossil fuels have been consumed in large quantities, and the world is facing serious energy shortages and environmental pollution problems. China is in a period of rapid economic development, and the automobile industry, as a strong industry driving China's economic growth, is developing particularly rapidly. However, traditional cars mainly use gasoline, diesel and other fossil fuels, which greatly increases China's oil consumption [1]. While consuming a large amount of oil resources, it also emits a large amount of harmful substances such as carbon monoxide, nitrogen oxides, and hydrides, seriously polluting the environment. To meet the needs of the energy sector and reduce pollution, China's carbon neutrality strategic goal is to peak carbon dioxide emissions before 2030 and achieve carbon neutrality before 2060. Researchers from all over the world are actively looking for substitutes for oil, and the development and utilization of alternative fuels has become a research hotspot. In order to alleviate the contradiction between the shortage of oil

**Corresponding author:* a2593567927@163.com

Tr Ren Energy, 2024, Vol.10, No.2, 229-238. doi: 10.17737/tre.2024.10.2.00173

resources and the growing demand for internal combustion engines and to ensure the long-term stable and sustainable development of China and the world's economy, it is necessary to find clean alternative fuels for internal combustion engines to replace petroleum-based fuels.

Alternative fuels must meet the requirements of high efficiency, cleanliness, low environmental impact, and recyclability. Hydrogen has become one of the ideal alternative fuels for internal combustion engines due to its clean, efficient combustion and almost zero emissions [2].

Physicochemical Properties of Hydrogen

Hydrogen is easy to diffuse and burn. The hydrogen diffusion in air is in the range of 0.756~1.747 $\times 10^{-4}$ m^2/s and the lower calorific value of combustion is about 120 MJ/kg. The minimum ignition energy (MIE) of hydrogen is only 0.02 mJ, the spontaneous combustion temperature is 858 K, the octane number is 130, the ignition limit range is 4~75 %, and the flame propagation speed is extremely fast which is about 1.85 m/s. At room temperature, hydrogen is very stable. Hydrogen generally does not react easily with other substances unless conditions are changed, such as ignition, heating, use of catalysts, etc. Since hydrogen is gaseous at room temperature, its portability and safety are poor. Hydrogen becomes highly reactive when adsorbed by metals such as palladium or platinum. Although hydrogen is non-toxic and physiologically inert to the human body, if the hydrogen content in the air increases, it will cause hypoxic asphyxia. As with all cryogenic liquids, direct contact with liquid hydrogen can cause frostbite. Hydrogen burns completely in oxygen to produce water, with almost no impact on the environment. There are many ways to produce hydrogen, including water electrolysis, natural gas reforming, biohydrogen, solar energy, wind energy, etc. It has a wide range of sources and meets the requirements for sustainable regeneration of alternative fuels for vehicles [3].

Hydrogen has extremely high requirements for sealing during its production, transportation and storage, and faces great safety challenges during its use. Many scholars have conducted in-depth research on its safety. Shivaprasad *et al.* [4] tested the performance and emission characteristics of a high-speed single-cylinder SI engine using different hydrogen-gasoline blends. They selected different hydrogen enrichment levels to study the effect of hydrogen addition on the engine brake mean effective pressure (BMEP), brake thermal efficiency, volumetric efficiency and emission characteristics. The results indicated that hydrogen enrichment improved combustion performance, fuel consumption, and brake mean effective pressure. The experimental results also showed that the brake thermal efficiency was higher than that of the pure gasoline condition. Additionally, the emissions of HC and CO were reduced with hydrogen enrichment.

When the engine uses hydrogen, only NO and H_2O are produced. In spark-ignition engines, hydrogen has the following outstanding physical and chemical properties compared to the 7-H gasoline used: First, the octane number is high. Hydrogen can achieve a larger ignition advance angle at low load, which is beneficial to improving the compression ratio and thermal efficiency. Second, the flame speed is high and flows horizontally, hydrogen and air mix faster and have higher thermal efficiency. Third, the ignition energy is low, hydrogen is not easy to ignite, and it is easy to achieve lean combustion, improve thermal efficiency, and reduce emissions. Fourth, wide ignition limit and wide hydrogen ignition range, which is conducive to working under partial load. Fifth, the high spontaneous combustion temperature of hydrogen is high, which is 1.6 times that of gasoline, and it is not easy to cause explosion hazards.

Combustion Characteristics of Hydrogen

Hydrogen is colorless and odorless, and its flame is transparent when it burns, so its presence is not easily detected by the senses. Generally, ethyl mercaptan is added to hydrogen for sensory detection and coloration of the flame. Hydrogen has strong self-ignition properties and the spontaneous combustion temperature is 850K under standard atmospheric pressure. It is easy to ignite, has excellent flame propagation characteristics, and can easily achieve lean combustion. Hydrogen can be mixed with air quickly to form a homogeneous mixture.

The chemical equation of hydrogen and air mixed combustion is

$$2H_2 + O_2 \rightarrow 2H_2O$$

A large amount of heat is released during this combustion process, which is three times that of gasoline combustion. Hydrogen is a high-energy fuel. Although the product of hydrogen-air mixed combustion is water and pollution-free, the high heat released during the combustion process promotes the chemical reaction of nitrogen and oxygen in the air.

$$\frac{1}{2}N_2+\frac{x}{2}O_2\rightarrow NO_x$$

NO_x is an air pollutant. The water produced by the combustion of hydrogen and air can be converted back into hydrogen by electrolysis. The chemical reaction formula of water electrolysis is

$$H_2O\rightarrow H_2+\frac{1}{2}O_2$$

Therefore, hydrogen energy has the characteristics of circularity and sustainability in the process of use. Because hydrogen is prone to spontaneous combustion, if the volume of hydrogen mixed in the air reaches 4.0~74.2 % of the total volume, an explosion will occur when it is ignited. Therefore, the purity of hydrogen must be tested during the use of hydrogen [6].

Study on the Application of Hydrogen in Internal Combustion Engines

Ideality of Hydrogen as an Alternative Fuel for Internal Combustion Engines

Hydrogen is an ideal alternative fuel for internal combustion engines due to its efficient and clean combustion characteristics. Hydrogen is a carbon-free fuel, which produces H_2O after combustion. It does not emit CO_2, CO, HC and sulfides. Hydrogen production resources are abundant and can be obtained through electrolysis using water as raw material. Water resources are much more abundant on Earth than the major fuel oil and coal. The mass fuel calorific value of hydrogen is the highest among all kinds of fuels. It is measured to be 140 MJ/kg, which is about 3 times that of gasoline, but the theoretical air-fuel ratio is 2.5 times that of gasoline [6]. The minimum ignition energy of hydrogen is 1/3 of that of gasoline, and the flame propagation characteristics are very good. The flame propagation speed of hydrogen is 2.91 m/s, which is 7.7 times that of gasoline. The ignition limit is wide (4.1~75%), the combustion adjustment is flexible, and it is easy to achieve lean combustion. It has the advantages of good economy, more complete combustion, and low combustion temperature. Hydrogen fuel is easy to ignite and has good starting performance. The spontaneous combustion temperature under atmospheric pressure is lower than that of diesel (625K) and gasoline (770K), and the density is small, which is conducive to improving the compression ratio and the thermal efficiency of hydrogen internal combustion engines [7]. The diffusion coefficient of hydrogen in the atmosphere is 8 times that of gasoline, which can quickly form a combustible mixture. It has low requirements on the inlet structure and combustion chamber shape of the internal combustion engine, and the combustion speed and the combustion temperature are high. Hydrogen has a high flame propagation speed at the theoretical air-fuel ratio, which is close to constant volume combustion. The hydrogen internal combustion engine cycle is closer to the ideal cycle, the pumping loss is small, and the thermal efficiency is higher than that of the gasoline engine.

Hydrogen has a shorter quenching distance of 0.64 mm during combustion, which is 1/3 of gasoline. A smaller quenching distance allows the flame to propagate to the cylinder wall and even reach the piston clearance, making the combustion more complete. Hydrogen has a higher spontaneous combustion temperature, a shorter ignition delay, a faster flame propagation speed, a higher octane number, and is less likely to produce knock. Hydrogen can be used in many forms, such as gas, liquid, or solid hydride. Solid hydride is the ideal form of hydrogen, because of its safety and convenience [8, 9]. There are generally two ways to use hydrogen as an internal combustion engine fuel: One is the electrochemical method, which converts the chemical energy of hydrogen into electrical energy and thermal energy in a fuel cell. The other is the thermochemical method, that is, combustion, which converts the chemical energy of hydrogen into heat or kinetic energy. There are two main forms of hydrogen as an internal combustion engine fuel, namely pure hydrogen and mixed hydrogen.

Pure Hydrogen

There are two ways to use hydrogen as a fuel, namely fuel cells and hydrogen internal combustion engines. The product of fuel cells is water, with zero emissions, they are not limited by the Carnot cycle efficiency, and have high energy conversion efficiency. Because there are no moving parts in the battery, the noise is low. Hydrogen fuel cells have strong overload capacity and convenient design. However, the high cost of batteries and the lack of infrastructure and maintenance have limited its development. Compared with fuel cells, hydrogen internal combustion engines are easier to implement. The combustion products of hydrogen internal combustion engine are only H_2O and NO_x, and the emission of NO_x is very small at low load. Only at full load or near full load, there is a little more NO_x emission than gasoline engine. But measures can be taken to reduce it. The hydrogen internal combustion engine does not have HC, CO, CO_2 and soot emissions. It can achieve full combustion in lean combustion, high system efficiency, and long engine life [10, 11].

Mixed Hydrogen

Blending hydrogen with other fuels (such as natural gas, gasoline, diesel, etc.), that is, hydrogen blending, can compensate for the power loss caused by other fuels due to low energy density or lean combustion, and improve the fuel economy. The amount of hydrogen required for a hydrogen-blended fuel engine is not large. It is mainly used as a fuel additive to improve the thermal efficiency of the engine and reduce fossil fuel consumption and emissions. Currently, hybrid hydrogen fuel engines are easier to implement in cars than pure hydrogen fuel engines.

Hydrogen-Natural Gas

As a vehicle fuel, natural gas can reduce the emissions of pollutants such as CO, SO, Pb and particulate PM2.5. However, since methane, the main component of natural gas, has a high calorific value of 36,000 kJ/m3, and its combustion temperature can reach 2,300°C under high temperature and high pressure, it is easy to generate NO_x. Therefore, in actual use, compared with gasoline engines and diesel engines, natural gas internal combustion engines do not reduce NO_x emissions. Blending hydrogen into natural gas can effectively reduce the combustion temperature, thereby reducing NO_x emissions. Hydrogen is easy to diffuse and can be easily mixed with natural gas in any proportion, and both can be stored in the same container. Adding a certain amount of hydrogen to natural gas can extend the lean combustion limit of the mixture, shorten the ignition delay period and combustion duration, improve thermal efficiency, and reduce HC, CO, CO_2 emissions. NOx emissions are also lower than pure hydrogen engines. Experiments have shown that the mixed combustion of 5~7 % mass or 15~20 % volume of hydrogen and natural gas has the lowest NO_x emission [13]. Liu *et al.* [12] studied natural gas mixed with hydrogen. When the ignition timing can be changed in time with the hydrogenation rate, a higher compression ratio can improve the thermal efficiency under high and low loads. In particular, when 20% volume hydrogen is added, the performance of the internal combustion engine is significantly improved. The research results of Subramanian *et al.* [13] on the combustion of natural gas mixed with hydrogen show that the emissions of NO_x, HC and CO produced by the combustion of natural gas mixed with hydrogen are lower than those of natural gas. Xu, *et al.* [14] used hydrogen-natural gas mixed fuel on large buses. The results show that the performance of the internal combustion engine is almost the same as that of the pure natural gas internal combustion engine.

Hydrogen-Gasoline

Since hydrogen plays a promoting role in combustion, the main purpose of gasoline-hydrogen mixed combustion is to improve thermal efficiency and reduce fuel consumption. The ignition energy of hydrogen is low, the diffusion coefficient is large, and the ignition delay period of the mixture is shortened. The ignition delay period of gasoline mixed with hydrogen will be shortened and the flame propagation speed will be accelerated. The actual cycle is closer to the constant volume cycle than that of the gasoline engine, which can achieve lean and fast combustion and improve the economy of the engine. The chain combustion reaction of hydrogen produces a large number of activation centers, which is conducive to the full reaction of HC and CO components in the cylinder, greatly reducing their emissions. CO emissions are reduced to less than 1/4 of the original gasoline engine, and HC emissions are reduced to less than 3/4 of the original gasoline engine. Active ions such as OH, H, and O produced during the combustion of gasoline-mixed hydrogen play a role in accelerating combustion, suppressing deflagration, and improving the compression ratio and thermal efficiency of the internal combustion engine. There is an optimum value for the hydrogen content in gasoline. If the amount of hydrogen is too little, the advantages of hydrogen in optimizing combustion cannot be fully utilized. If the amount of hydrogen is too much, flashback is likely to occur. The specific optimal amount of hydrogen is determined by the speed and load of the internal combustion engine.

Hydrogen-Diesel

Diesel engines are widely used as power sources for agricultural machinery due to their high thermal efficiency, strong reliability, long service life, good power performance and fuel economy. However, one of the biggest defects of diesel engines is that NO_x and particulate emissions are high, and it is difficult to effectively reduce both emissions at the same time due to the limitation of the compromise curve. Therefore, how to effectively reduce the emission of pollutants under the premise of ensuring the power and economy of diesel engines is an urgent problem to be solved. It has been found that almost all NO_x emitted by diesel engines is generated within 20 °CA after the start of combustion, and delaying fuel injection is a simple and effective way to reduce its emissions. However, delaying fuel injection will lead to an increase in fuel consumption and exhaust smoke. At present, diesel engines mainly use exhaust gas recirculation (EGR) technology to reduce NO_x emissions. But high EGR rates mean less fresh air and worse combustion in the cylinder, which reduces the economy of diesel engines and increases soot emissions.

The conditions of soot formation are high temperature and hypoxia. The high compression ratio of diesel engine structure and the inhomogeneity of combustion make two conditions of high temperature and hypoxia always exist in the combustion process. In order to reduce soot and NO_x emissions at the same time. Many researchers [15] took advantage of the combustion characteristics of hydrogen and mixed an appropriate amount of hydrogen into the diesel combustion process to optimize combustion. When a diesel engine uses hydrogen diesel fuel, it can not only maintain the high compression ratio and high thermal efficiency of the diesel engine, but also ensure stable ignition (diesel ignition). It does not require high ignition timing and can easily achieve lean combustion, thereby reducing NO_x and particulate matter emissions.

According to measurements, the amount of hydrogen added has an optimal value or optimal range. If too little hydrogen is added, it will not optimize combustion, but too much will worsen combustion. Studies have shown that when the hydrogen content is 5%, soot emissions reach a minimum, and 5% hydrogen content has little effect on the excess air coefficient. Dinesh & Kumar [16] added hydrogen into the intake air of a ZS195 diesel engine and then used EGR technology to reduce the emissions. Through research, it was found that under high load conditions, when the EGR rate is constant, as the hydrogen blending rate increases, the peak pressure and pressure rise rate in the cylinder of the ZS195 diesel engine will increase. This is due to the high combustion rate and diffusion rate of hydrogen. Under hydrogen-rich conditions, HC, CO and soot emissions are reduced. The reason is that hydrogen optimizes combustion, and technology breaks through the limitations of the NO_x-soot trade-off curve and can reduce emissions of both. The thermal efficiency and NO_x emission of the ZS195 diesel engine are increased by fixing EGR rate and increasing hydrogen mixing amount. The peak pressure and temperature in cylinder are increased, which is beneficial to NO_x generation. NO_x emission can be reduced by lean combustion and delaying fuel injection. Qian *et al.*

[17] found that when the EGR rate of the ZS195 diesel engine is low, the combustion of hydrogen is optimized and the thermal efficiency of diesel engine is improved. At high EGR rates, the effect of hydrogen optimizing combustion is not enough to offset the impact of deteriorated in-cylinder combustion caused by high EGR rates, and the thermal efficiency of the diesel engine is basically not improved. Therefore, there is an optimal value or optimal range of EGR rate [15]. The hydrogen-rich gas produced by diesel reforming technology is mixed with air and enters the cylinder for combustion, which can effectively improve the performance of the diesel engine and reduce various emissions of the diesel engine to varying degrees.

Problems to be Solved in the Development of Hydrogen Internal Combustion Engine

Hydrogen exists in gaseous form at room temperature, with low ignition energy, fast diffusion speed and easy leakage. Its safe storage, transportation, packaging and on-board installation are all difficult. As a result, diesel engines need to be able to produce hydrogen (such as diesel reforming to produce hydrogen) to implement HEGR technology. At the same time, the cost of hydrogen production is high and the technology is relatively complex. Therefore, it will take a long time to achieve large-scale application and commercialization of hydrogen fuel in internal combustion engines. In the hydrogen-air mixture, the concentration of oxygen atoms is high, and the cycle temperature is relatively high during hydrogen combustion, and the NO_x emission concentration is high. Therefore, the hydrogen internal combustion engine needs to solve the problem of reducing NO_x emissions and restoring power. For the former, water injection, EGR, N_2 and CO_2 can be used to reduce it. For the latter, the conventional power improvement method is limited by the combustion characteristics of hydrogen, so the power recovery is more difficult. For example, increasing the compression ratio will cause premature combustion or backfire, increasing the equivalent fuel-air ratio will cause the increase of NO_x emissions and incomplete combustion, and the use of pressurized intercooling will increase the probability of premature combustion and NO_x emissions.

Although hydrogen can make the internal combustion engine easy to cold start, it can lead to abnormal combustion problems such as pre-ignition, flashback, deflagration and knock. Premature combustion leads to low efficiency and rough work of internal combustion engine, increases the mechanical load and thermal load of internal combustion engine, increases the exhaust temperature, and even stops the hydrogen internal combustion engine. Tempering causes the hydrogen internal combustion engine to produce strong noise, which is easy to damage the internal combustion engine. Cylinder knocking will cause the hydrogen internal combustion engine to work unstably, generate vibration and noise, and even cause misfire, damage the intake pipe and hydrogen supply system. Deflagration is a sharp combustion phenomenon of the end mixture. Mild deflagration is conducive to combustion in the cylinder. Moderate or above deflagration may lead to a sharp increase in gas pressure, rough combustion, knocking on the cylinder, early termination of combustion, decrease of output power and thermal efficiency of the internal combustion engine, increase of fuel consumption, overheating of the cylinder, increase of stress of parts, accelerated wear of parts, and deterioration of emission performance of the internal combustion engine. The abnormal combustion problem of hydrogen internal combustion engine is the bottleneck problem in its development and application.

When using hydrogen-gasoline fuel, it is necessary to install a hydrogen supply system on gasoline vehicles. Although this is technically feasible, it is not economical. At the same time, gasoline hydrogen blending combustion needs to solve the problem of coordination between factors such as output power, combustion thermal efficiency, fuel economy, emission quality and abnormal combustion based on different working conditions of the engine.

Direct injection hydrogen internal combustion engine can improve the excess air coefficient and compression ratio, effectively avoid premature combustion, eliminate backfire, increase output power and improve thermal efficiency. However, the structure of its hydrogen injection system is complex, the reliability of components needs to be solved, the uniformity of mixture formation needs to be improved, the difficulty of ignition organization needs to be reduced, the time and quantity of hydrogen injection and the ignition time need to be accurately controlled, and the cyclic variation at the initial stage of combustion needs to be controlled.

The structure of the hydrogen injection system of the intake pipe injection hydrogen internal combustion engine is not complex, and the mixture formation and combustion are easy to organize. The structure is not changed much when the traditional internal combustion engine is modified. However, the hydrogen internal combustion engine is prone to abnormal combustion phenomena such as pre-ignition, knocking and tempering. At present, it can be avoided by accurately controlling the ignition timing.

In general, hydrogen internal combustion engine can mainly use technologies (such as compound intake, lean combustion, electronically controlled high pressure direct injection, supercharging, intercooling, increasing compression ratio, EGR, reducing intake temperature, and catalytic post-processing) to solve the problems of pre-ignition, tempering, low output power density, high NO_x emissions. But the best solution is to numerically simulate the working process of the internal combustion engine, establish various calculation models, and realize the comprehensive optimization control of hydrogen injection timing, ignition timing, combustion process, starting, idle speed, variable speed and other working conditions, so as to realize the optimal combination of combustion and emission of hydrogen internal combustion engine. This is an issue that needs further study [18, 19].

CONCLUSIONS

Hydrogen has been considered as one of the best alternative fuels for internal combustion engines due to its high efficiency and clean combustion. Effectively solving the problems existing in the development of hydrogen internal combustion engines can promote their development and application, ultimately leading to industrialization, solving the environmental pollution problem in the current automobile era, and promoting sustainable social and economic development. However, in order to welcome the arrival of a true "hydrogen economy", hydrogen internal combustion engines still need to carry out a large amount of continuous basic research, such as how to improve combustion thermal efficiency and output power density and achieve optimal control of composite modes, how to optimize the structural design of internal combustion engines and improve material performance and optimize solutions.

CONFLICTS OF INTEREST

The author declares that there is no conflict of interests regarding the publication of this paper.

REFERENCES

[1] Zhang, X., Diao, Z., Ma, H., Xie, X., Wang, Y., Liu, X., ... & Zhu, F. (2023). Multi-class organic pollutants in PM2. 5 in mixed area of Shanghai: Levels, sources and health risk assessment. *Science of The Total Environment, 903*, 166352. doi:https://doi.org/10.1016/j.scitotenv.2023.166352

[2] Li, X., & Nam, K. M. (2022). Environmental regulations as industrial policy: Vehicle emission standards and automotive industry performance. *Environmental Science & Policy, 131*, 68-83. doi:https://doi.org/10.1016/j.envsci.2022.01.015

[3] Shahzad, K., & Cheema, I. I. (2024). Low-carbon technologies in automotive industry and decarbonizing transport. *Journal of Power Sources, 591*, 233888. doi:https://doi.org/10.1016/j.jpowsour.2023.233888

[4] Shivaprasad, K. V., Raviteja, S., Chitragar, P., & Kumar, G. N. (2014). Experimental Investigation of the Effect of Hydrogen Addition on Combustion Performance and Emissions Characteristics of a Spark Ignition High Speed Gasoline Engine. *Procedia Technology, 14*, 141-148. doi:https://doi.org/10.1016/j.protcy.2014.08.019

[5] Peng, J., Shi, X., & Tong, X. (2023). Extended producer responsibility for low carbon transition in automobile industry. *Circular Economy, 2*(2), 100036. doi: https://doi.org/10.1016/j.cec.2023.100036

[6] Algayyim, S. J. M., Saleh, K., Wandel, A. P., Fattah, I. M. R., Yusaf, T., & Alrazen, H. A. (2024). Influence of natural gas and hydrogen properties on internal combustion engine performance, combustion, and emissions: A review. *Fuel, 362*, 130844. doi:https://doi.org/10.1016/j.fuel.2023.130844

[7] Zhou, F., Yu, J., Wu, C., Fu, J., Liu, J., & Duan, X. (2024). The application prospect and challenge of the alternative methanol fuel in the internal combustion engine. *Science of The Total Environment, 913*, 169708. doi:https://doi.org/10.1016/j.scitotenv.2023.169708

[8] Wang, J., & Azam, W. (2024). Natural resource scarcity, fossil fuel energy consumption, and total greenhouse gas emissions in top emitting countries. *Geoscience Frontiers, 15*(2), 101757. doi:https://doi.org/10.1016/j.gsf.2023.101757

[9] Kovač, A., Paranos, M., & Marciuš, D. (2021). Hydrogen in energy transition: A review. *International Journal of Hydrogen Energy, 46*(16), 10016-10035. doi:https://doi.org/10.1016/j.ijhydene.2020.11.256

[10] Chien, F., Kamran, H. W., Albashar, G., & Iqbal, W. (2021). Dynamic planning, conversion, and management strategy of different renewable energy sources: a sustainable solution for severe energy crises in emerging economies. *International Journal of Hydrogen Energy, 46*(11), 7745-7758. doi:https://doi.org/10.1016/j.ijhydene.2020.12.004

[11] Rubio, F., Llopis-Albert, C., Valero, F., & Besa, A. J. (2020). Sustainability and optimization in the automotive sector for adaptation to government vehicle pollutant

emission regulations. *Journal of Business Research, 112*, 561-566. doi:https://doi.org/10.1016/j.jbusres.2019.10.050
[12] Liu, W., Wan, Y., Xiong, Y., & Gao, P. (2022). Green hydrogen standard in China: Standard and evaluation of low-carbon hydrogen, clean hydrogen, and renewable hydrogen. *International Journal of Hydrogen Energy, 47*(58), 24584-24591. doi:https://doi.org/10.1016/j.ijhydene.2021.10.193
[13] Subramanian, V., Mallikarjuna, J. M., & Ramesh, A. (2017). Intake charge dilution effects on control of nitric oxide emission in a hydrogen fueled SI engine. *International Journal of Hydrogen Energy, 32*(12), 2043-2056. doi:https://doi.org/10.1016/j.ijhydene.2016.09.039
[14] Xu, P., Ji, C., Wang, S., Bai, X., Cong, X., Su, T., & Shi, L. (2018). Realizing low NOx emissions on a hydrogen-fuel spark ignition engine at the cold start period through excess air ratios control. *International Journal of Hydrogen Energy, 43*(46), 21617-21626. doi:https://doi.org/10.1016/j.ijhydene.2018.09.136
[15] Rubio, F., Llopis-Albert, C., Valero, F., & Besa, A. J. (2020). Sustainability and optimization in the automotive sector for adaptation to government vehicle pollutant emission regulations. *Journal of Business Research, 112*, 561-566. doi:https://doi.org/10.1016/j.jbusres.2019.10.050
[16] Dinesh, M. H., & Kumar, G. N. (2023). Experimental investigation of variable compression ratio and ignition timing effects on performance, combustion, and Nox emission of an ammonia/hydrogen-fuelled Si engine. *International Journal of Hydrogen Energy, 48*(90), 35139-35152. doi:https://doi.org/10.1016/j.ijhydene.2023.05.219
[17] Qian, Y. J., Zuo, C., Xu, T., & Lu, S. (2009). The effect of EGR rate on the performance and emissions of ZS195 diesel engine. *Journal of Hefei University of Technology: Natural Science Edition, 32* (9), 1361-1364.
[18] Badawy, T., Panithasan, M. S., Turner, J. W., Kim, J., Han, D., Lee, J., ... & Chang, J. (2024). Performance and emissions evaluation of a multi-cylinder research engine fueled with ethanol, methanol, gasoline Euro-6, E85, and iso-stoichiometric ternary GEM mixtures operated at lean conditions. *Fuel, 363*, 130962. doi:https://doi.org/10.1016/j.fuel.2024.130962
[19] Baek, S., Lee, S., Shin, M., Lee, J., & Lee, K. (2022). Analysis of combustion and exhaust characteristics according to changes in the propane content of LPG. *Energy, 239*, 122297. doi:https://doi.org/10.1016/j.energy.2021.122297

Trends in Renewable Energy
OPEN ACCESS ISSN: 2376-2144
Peer-Reviewed Article futureenergysp.com/index.php/tre

Mechanical Study of a Solar Central Air Conditioning Duct Cleaning Robot

Li Sun*

School of Mechanical Engineering, North China University of Water Resources and Electric Power, Zhengzhou, Henan 450045, CHINA

Received May 30, 2024; Accepted June 29, 2024; Published July 10, 2024

With the rapid economic development and the depletion of fossil fuels, the use of renewable energy such as solar energy can help alleviate energy supply pressure and carbon emissions. There have been many studies on solar energy powered robots. In this paper, a solar-powered duct-cleaning robot is used as the basis for the design of its mechanism. The robot is designed to clean vertical ducts with a length of 5~10 meters, a width of more than 400 mm and a height of 500~800 mm. The design of the robot is based on four aspects: solar energy, drive, camera and cleaning device. AutoCAD was used for 2D drawing of each part, while SolidWorks was used for modeling and assembling the parts of the vertical duct cleaning robot. The solar duct cleaning robot is characterized by high adaptability, low cost, and smooth and fast movement within the allowed size range.

Keywords: Vertical ventilation ducts; Solar energy; Cleaning robot; AutoCAD; SolidWorks

Introduction

Since entering the 21st century, the demand for energy has increased dramatically. However, with the gradual reduction of fossil energy reserves and the current deterioration of the environment, finding new energy sources and energy conservation and emission reduction have become urgent issues that need to be addressed by all countries. Taking several current new energy sources into consideration, solar energy has more prominent advantages. It is not only abundant in resources and widely distributed, but also has zero emissions. The installed capacity is increasing year by year, and it is the mainstream of current new energy development [1]. In the development of the photovoltaic (PV) industry, with the continuous advancement of global industrialization, the photovoltaic industry has gradually gained good market and economic support. It is predicted that by around 2050, photovoltaic power generation is expected to reach 10% to 20% of the electricity supply, becoming an indispensable part of the human energy structure [2]. Since 1970, a global upsurge in photovoltaic power generation technology research has emerged, and corresponding industrial planning has been formulated. Through various promotions, the rapid development of the photovoltaic industry has been promoted [3]. As one of the fastest growing industries today, the photovoltaic industry has immeasurable potential for future development.

The formal research on solar cars began in the UK. In 1978, the world's first solar car was born in the UK, with a speed of up to 13 km/h. In 1982, Mexico's three-wheeled

*Corresponding author: 2362911483@qq.com

Tr Ren Energy, 2024, Vol.10, No.2, 239-256. doi: 10.17737/tre.2024.10.2.00175

solar car could reach a speed of 40 km/h, but its range was only 40 minutes. Ahmed *et al.* [4] analyzed lightweight solar vehicles from an economic perspective and the results showed that the total cost of lightweight solar vehicles over their service life is much lower than that of traditional vehicles. Alhammad *et al.* [5] investigated ways to improve the conversion efficiency of PV modules and used it as an auxiliary power source for a light-storage hybrid solar car. Tang *et al.* [6] analyzed the feasibility of photovoltaic electric vehicles from both technical and economic perspectives. The research results show that the energy cost of photovoltaic electric vehicles is USD$0.204/kWh to $0.372/kWh, which is higher than that of grid-connected electric vehicles ($0.150/kWh), but greenhouse gas emissions can be reduced by 47%-78%. Photovoltaic electric vehicles are considered to be the most promising model in the near future. Selin *et al.* [7] conducted in-depth research on the energy usage of solar racing cars on fixed routes and implemented it in the SPbPUStrat software solution, which greatly improved the utilization rate of solar energy and increased the chances of success. This study combines solar energy with a cleaning robot, and the design can have many advantages such as energy saving and environmental protection, long driving range, relatively mature technology, simple transformation, short development cycle, and superior performance.

The central air conditioning system dominates the air circulation and exchange within the building, so it is also known as the “lungs of the building” [8]. However, its own “health” is not optimistic. The central air conditioner that has not been cleaned for a long time is much dirtier than you think: Studies have shown that an air conditioner heat exchanger that has not been cleaned for three years contains 230 g of dust, 56 g of flakes, and 15 g of oil smoke. The number of bacteria can be up to 60 times that of a toilet bowl [9]. If the inner wall of the duct is only cleaned by ordinary means, it is difficult to clean it thoroughly [10]. As the epidemic has become normalized, it is also required to disinfect the inner walls of air-conditioning ducts. However, the cleaning and maintenance of central air-conditioning is very inconvenient for people, whether it is household air-conditioning or air-conditioning in public buildings [11]. There are three main hazards of not cleaning the central air conditioner for a long time: First, due to the lack of ventilation and gas exchange with the outside world for a long time, the dust accumulated indoors will increase, causing people working indoors to be infected with viruses; Second, dust and foul-smelling gases will remain in the air; Third, people will suffer from "Legionnaires' disease" (Figure 1). Therefore, the cleaning and disinfection of central air-conditioning ventilation ducts requires sufficiently advanced cleaning and disinfection equipment, and the invention and manufacture of duct cleaning robots is a historical choice.

The cleaning of ventilation ducts is to divide the ducts into several sections, open a window in each section, and use the high-speed rotation of the cleaning mechanism to drive the brush on the telescopic arm to brush off the dust adhering to the inner wall. After brushing, use a vacuum cleaner to suck out the stubborn dust, thereby achieving the purpose of cleaning the inner wall of the duct. The cleaning process is shown in Figure 2 [12].

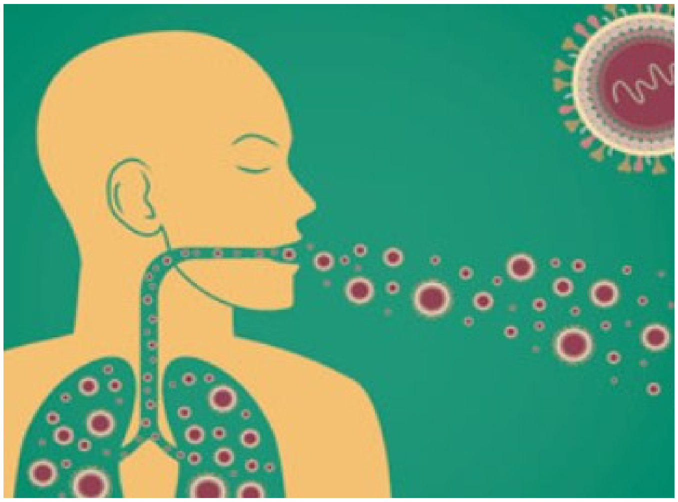

Fig. 1. Schematic diagram of the respiratory system infected with Legionella

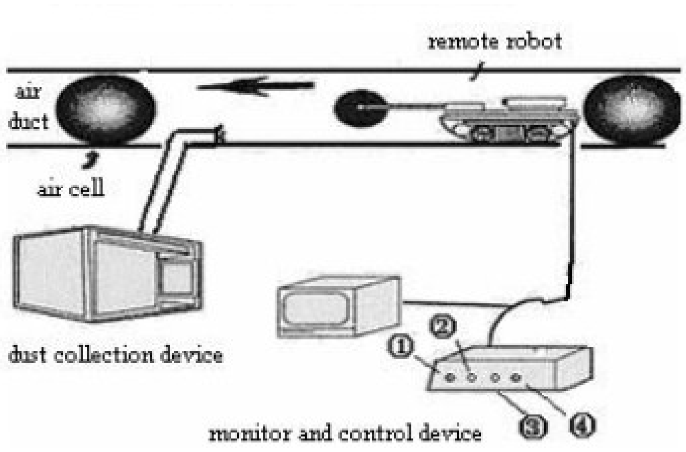

Fig. 2. Workflow diagram of duct cleaning robot [12]

The traditional cleaning robot does not realize the function of intelligent work, and is not very targeted, and there is no special device for a specific working environment. The cleaning robot designed in this paper has a simple structure and light weight, which is conducive to the subsequent addition of solar energy devices. It mainly cleans the vertical direction of the central air-conditioning ventilation duct and related structural design to achieve efficient cleaning of the vertical duct.

Overall Design of Duct Cleaning Robot

The design of the central air conditioning vertical duct cleaning robot in this paper is divided into four main parts: wheeled mobile mechanism design, flexible arm cleaning mechanism design, camera lighting device and solar power generation system design.

(1) The cleaning robot adopts a wheeled moving mechanism, which has stronger adaptability than other mechanisms. It uses the suction cup on the body for positioning when moving, and the positioning of the cleaning robot on the inner wall of the duct is achieved by evacuating the air between the suction cup and the inner wall of the duct.

(2) As for the cleaning mechanism of the cleaning robot, it mainly drives the cleaning mechanism with bristles of different sizes through a driving motor to complete the cleaning work of the vertical ventilation duct at high speed.

(3) During the cleaning operation, it is impossible to complete the cleaning task successfully every time, so the operator needs to develop corresponding solutions according to different working conditions. Therefore, it is necessary to equip a CCD camera and lighting equipment. The CCD camera transmits the signal to the display in front of the operator through a matching cable so that the operator can make corresponding solutions [13].

(4) Solar cells convert solar energy into the electricity needed by the machine, ensuring the robot's battery life and making work more environmentally friendly.

Selection of Drive Motors for Mobile Mechanisms

The selected motor should have the following characteristics: fast response, multi-stage speed regulation, small torque fluctuation, small size and light weight. DC motors have the advantages of a wide speed regulation range, good smoothness, and strong overload capacity. Therefore, this robot chooses DC reduction motors (Figure 3) as the driving mode of the mobile mechanism [14].

Fig. 3. Schematic diagram of DC geared motor

The resistance F encountered by the duct cleaning robot when cleaning in a vertical duct is:

$$F = aG + G + F_1 \qquad \text{Eq. 1}$$

where a is the rolling resistance coefficient between the ducts, which is taken as 0.014; the self-weight of the robot is G, and the resistance generated by the load carried is F_1; and the gravitational acceleration $g=10\ m/s^2$.

The total resistance F_2 is:

$$F_2 = K \times F \qquad \text{Eq. 2}$$

where K is the resistance correction factor; k = 1.2.

Assuming that the self-weight of the duct cleaning robot is 10 kg and the resistance generated by the load it carries is 3 kg, the resistance F of the duct cleaning robot as it proceeds through the vertical duct is:

$$F = 1.014G + F_1 = 131.4N \qquad \text{Eq. 3}$$

Total resistance is:

$\mathrm{F}_2 = \mathrm{K} \times \mathrm{F} = 158\mathrm{N}$ Eq. 4

The drag force on each drive wheel is:

$\mathrm{F}_3 = \frac{\mathrm{F}_2}{2} = 79N$ Eq. 5

Let the maximum speed of the duct cleaning robot be 12 m/min then:

$P = F \times V = 15.8W$ Eq. 6

Check the table to take the working condition factor $K_a = 1.6$:

$P = K_a \times P = 25.28W$ Eq. 7

The maximum speed of the wheel is:

$n = \frac{V}{\pi} \times d = 12/3.14 \times 0.13$ Eq. 8

Drive motor: According to the calculated power and speed, select a DC gear motor with a rated power of 30 W and a rated voltage of 24 V.

Wheel Strength Check

The wheels are the most stressed part of the entire mechanism and are the guarantee for the robot to work properly. Therefore, we need to consider the material of the wheel and whether the strength of the wheel is sufficient for the work of this project. Considering both economic and strength requirements, 45 steel is selected as the wheel material. At the same time, in order to reduce the risk of the robot slipping during work, the roller surface is knurled to increase the friction during processing.

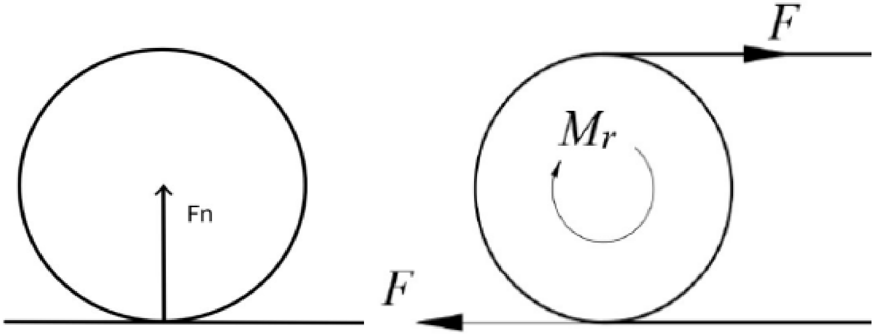

Fig. 4. Sketch of the forces on the wheels

In Figure 4, $M\mathbf{r}$ is the output torque of the motor, and F is the force imparted to the wheel by the rotation of the motor, which offsets the torque:

Rated torque of the motor: $0.4N \cdot \mathbf{m}$

Reducer reduction ratio: i=100

Transmission efficiency: $\boldsymbol{\eta}$ =0.7

$M\mathbf{r} = \mathbf{i} \times \boldsymbol{\eta} \times M = \mathbf{100} \times \mathbf{0}.7 \times \mathbf{0.4} = \mathbf{28}N \cdot \mathbf{m}$ Eq. 9

From moment equilibrium:

$M\mathbf{r} = \mathbf{2F} \times d/2$ Eq. 10

Then the magnitude of the force on the wheel in the horizontal direction is:

$F = \frac{M\mathbf{r}}{\mathbf{d}} = \mathbf{215N}$ Eq. 11

The magnitude of the force on the wheel in the vertical direction is:

$F_n = G + \mathrm{F}_1 = 130N$ Eq. 12

The force in the vertical direction on each wheel is:

$$F = \frac{F_n}{4} = 32.5N \qquad \text{Eq. 13}$$

As the diameter of the designed wheel is 130 mm, the strength of the whole mobile mechanism part is very large. According to the vertical direction of the wheel force and the horizontal direction of the force size, it can be seen that this wheel can fully meet the design requirements.

Selection of Robot's Positioning Device on the Inner Wall of a Vertical Duct

There are three main types of positioning for vertical duct cleaning robots: vacuum adsorption, magnetic adsorption, and negative airflow adsorption [15]. Negative pressure airflow adsorption will cause dust to be generated during the cleaning operation, affecting the observation of the camera device, and is not suitable for cleaning the inner wall of central air conditioning ducts. Therefore, the following focuses on the analysis of vacuum adsorption and magnetic adsorption.

Magnetic adsorption is the process of allowing the robot to adhere to the inner wall of the duct through magnetic force. However, magnetic adsorption has great limitations on the materials of the usage environment. This article focuses on the vertical air duct wall of central air conditioners. Since there is no unified material standard for domestically produced air ducts, the scope of application is not as large as vacuum adsorption, and the manufacturing price is higher than that of suction cups, so suction cups are chosen as the positioning device of the cleaning robot in this article.

Most vacuum adsorption uses a suction cup as an adsorption device, and the air inside the suction cup is expelled by squeezing or pumping to achieve the adsorption function. Among them, vacuum adsorption is the most widely used, and has little restriction on the materials used, and can adapt to most working environments. Therefore, this paper selects the suction cup as the adsorption and positioning device of the cleaning robot, and Figure 5 is a wheel suction cup assembly.

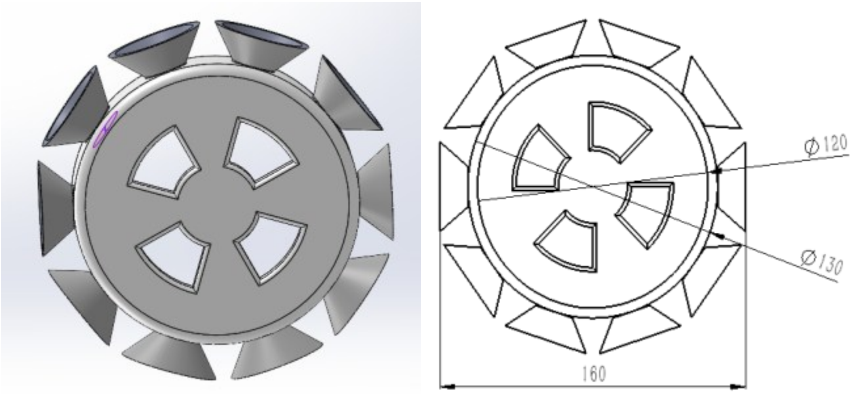

Fig. 5. Wheel suction cups

Design of the Cleaning Mechanism

The cleaning mechanism mainly consists of a mechanical arm, a flexible arm, and a brush connected to the flexible arm. When working, as the robot moves forward, the flexible arm starts to rotate at high speed, and the brush connected to the arm also rotates with the rotation of the flexible arm. As the mechanical arm gradually adjusts to the working height, the robot begins to clean the inner wall.

Rotary Brush Drive Motor Selection

When the robot is working, the high-speed rotation of the cleaning mechanism causes friction between the bristles and the inner wall, thus generating a large resistance torque. Therefore, we need to select a suitable drive motor in the cleaning mechanism. Figure 6 shows the schematic diagram of the rotating brush.

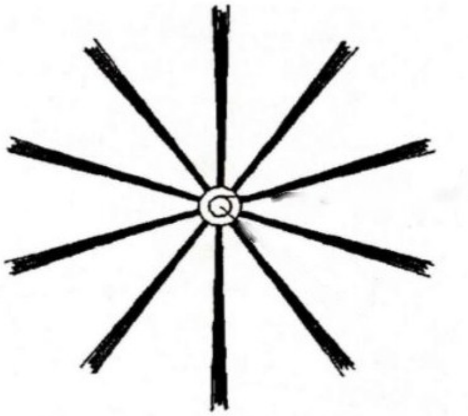

Fig. 6. Schematic diagram of rotating brush

Brush rotation torque Ma: (F is the stabilized drive wheel during operation, R is the radius of the brush shaft)

$$\boldsymbol{Ma = F \times R = Ta} \quad \text{Eq. 14}$$

Drive motor output torque Ta:

$$\boldsymbol{Ta = F \times R = 0.5\, N \cdot \mathrm{m}} \quad \text{Eq. 15}$$

In order to ensure that the cleaning requirements, according to the actual situation to choose the speed of n=1000r/min drive motor, then the motor power is:

$$\boldsymbol{P = \frac{Ta}{9550} = 52.4W} \quad \text{Eq. 16}$$

In actual situations, due to the influence of the working environment, the motor will lose some power during the transmission process. Therefore, the power of the motor should be greater than 52.4 W to meet the work of the cleaning brush. After checking the table, a DC motor with a rated voltage of 24 V, a rated speed of 3000 r/min, and a rated power of 63 W was selected as the driving motor of the cleaning brush head.

Selection of Bristle Material

(1) Vegetable type: Not wear-resistant and easily broken, short life span, need frequent replacement, difficult to clean.

(2) Animal: Bristles made from the ends of animal hairs have good stiffness and good water resistance and service life. However, for the cleaning robot proposed in this article, this material is expensive, which is not conducive to the popularization and promotion of the robot.

(3) Metal: Bristles made of steel, copper and other materials are prone to falling off, breaking and even being greatly deformed by high temperatures during use, affecting their normal working state.

(4) Engineering plastics: With the continuous advancement of technology, engineering plastic products have become more and more advantageous in terms of

performance and price. For example, nylon material is a commonly used cleaning material [16].

Table 1. Comparison Table of Bristle Material Properties

Material name	Temperature resistance	Water resistance	Chemical stability	Dissociation	Rigidity
Nylon 6	weak	usual	usual	usual	favorable
Nylon 66	usual	weak	favorable	usual	favorable
Nylon 610	usual	talented	weak	favorable	favorable
Nylon 1010	weak	usual	usual	favorable	usual
MC Nylon	usual	favorable	favorable	favorable	talented

The bristle material chosen for the cleaning robot in this paper is MC nylon material, which is also known as cast nylon (Table 1). MC nylon has good overall advantages among nylon materials.

Design of Camera Lighting Device for Cleaning Robot

The interior of the central air conditioning system is dimly lit, and additional lighting and video equipment must be installed to facilitate operators to adjust the movements of the cleaning robot in a timely manner (Figure 7). Before cleaning, the angle of the camera and the height of the camera are adjusted to ensure that there is the best observation angle between the width range of > 400mm and the height range of 50 to 800 mm [17].

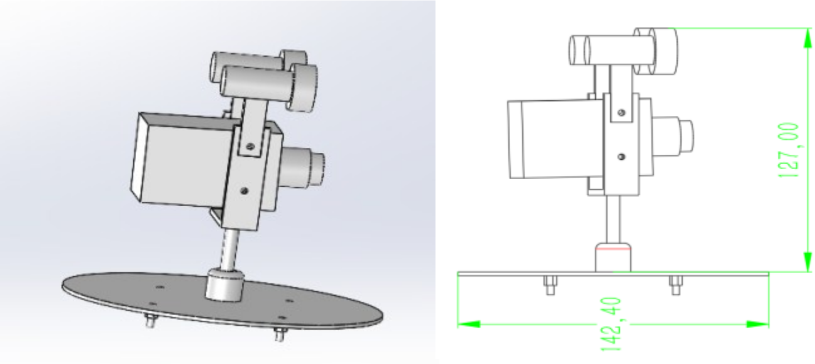

Fig. 7. Camera-illuminated device

Solar Power Plant Design

Solar panels are a type of power generation element that utilizes the photovoltaic effect. They are composed of multiple P-type semiconductors and N-type semiconductors. When sunlight shines on a semiconductor, photons excite the electron energy state inside the semiconductor into electrons and holes. Under the influence of the internal electric field, holes move toward the P-type semiconductor and electrons move toward the N-type semiconductor. In this way, the P-type semiconductor generates positive electricity and the N-type semiconductor generates negative electricity. Connecting the P-type semiconductor and the N-type semiconductor can generate direct current (DC). Figure 8 is a schematic diagram of a solar cell.

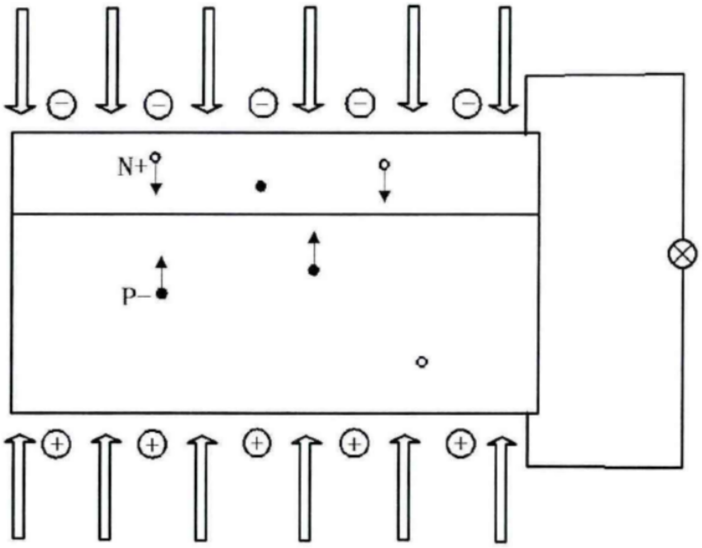

Fig. 8. Solar cell schematic diagram

2D Mapping of Cleaning Robots

Suction Pads

AutoCAD 2020 was used to draw the suction cup part (Figure 9). The suction cup part is an important element to ensure that the cleaning robot can move forward and position itself properly in the vertical duct, which is a core part of the design. Vacuum adsorption is used to achieve the positioning of the vertical duct cleaning robot when it moves in the vertical duct.

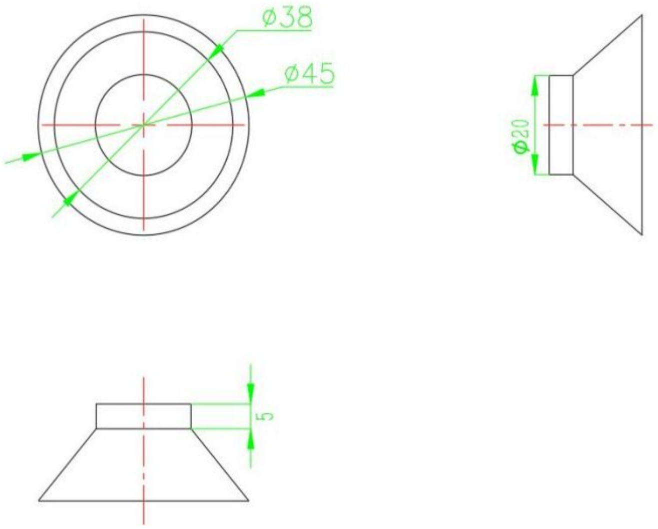

Fig. 9. 2D view of suction cup parts

Bottom Support Plate

AutoCAD 2020 was used to draw the bottom support plate with an overall size of 211 mm × 35 mm × 3 mm (Figure 10). The bottom support plate is one of the most basic components of the mobile mechanism. Together with other connecting plates and supports, it constitutes the mobile bearing part of the cleaning robot.

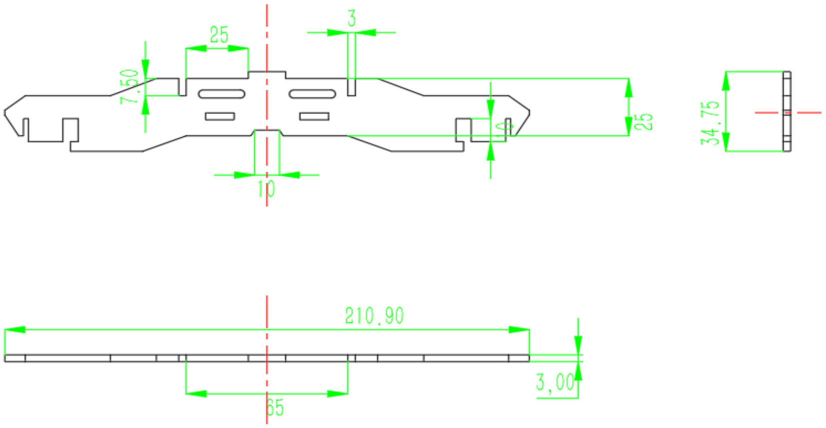

Fig. 10. 2D view of bottom support plate

Wheel

AutoCAD 2020 was used to draw the wheel parts with a radius of 75 mm and a width of 50 mm (Figure 11). The wheels of the vertical duct cleaning robot serve many purposes to beautify the appearance and make the cleaning robot more ornamental, while the suction cup positioning device of the vertical duct is also embodied in the wheels.

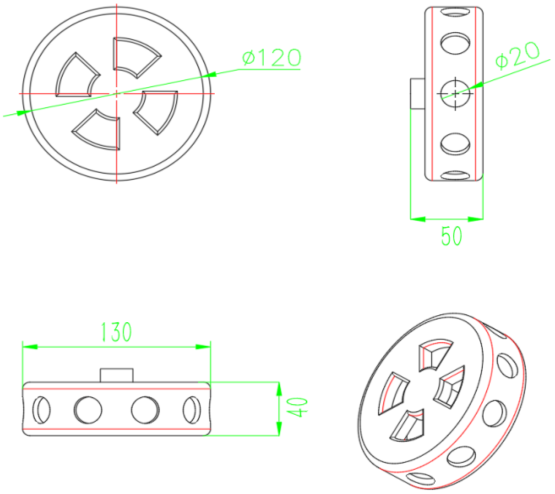

Fig. 11. Wheel 2D drawing

Cleaning Mechanism Connection

Use AutoCAD 2020 to draw a 2D drawing of the cleaning mechanism connection with a diameter of 40 mm (Figure 12). The connecting knot is crucial in the cleaning mechanism as it connects the flexible arm and the brush extending from the flexible arm.

The connection knot can make the flexible arm move more stably and complete the cleaning task more effectively.

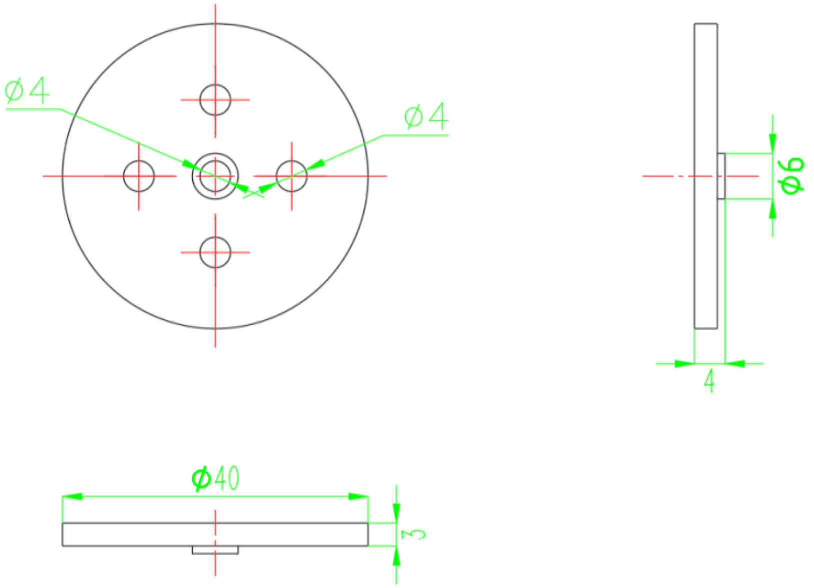

Fig. 12. 2D diagram of the connection junction of the cleaning mechanism

Cleaning Mechanism Swivel Connector

Use AutoCAD 2020 to draw a 2D drawing of the rotary connector of the cleaning mechanism with dimensions of 30 mm × 30 mm × 4 mm (Figure 13). The rotary connector is an important part of the cleaning mechanism that connects the motor to rotate the cleaning flexible arm.

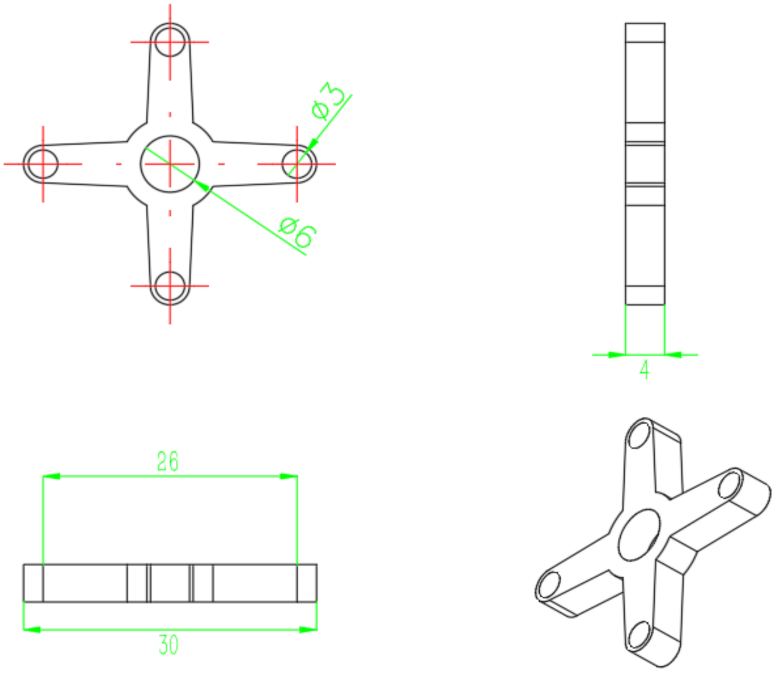

Fig. 13. 2D drawing of rotary joints

2D Drawing of the Mobile Mechanism

The 2D drawing of the mobile part of the cleaning robot with dimensions of 380mm×300mm×160mm using AutoCAD 2020 is shown in Figure 14. The mobile mechanism plays an important role in the whole cleaning robot to support the cleaning robot to complete the work and provide power to the cleaning robot.

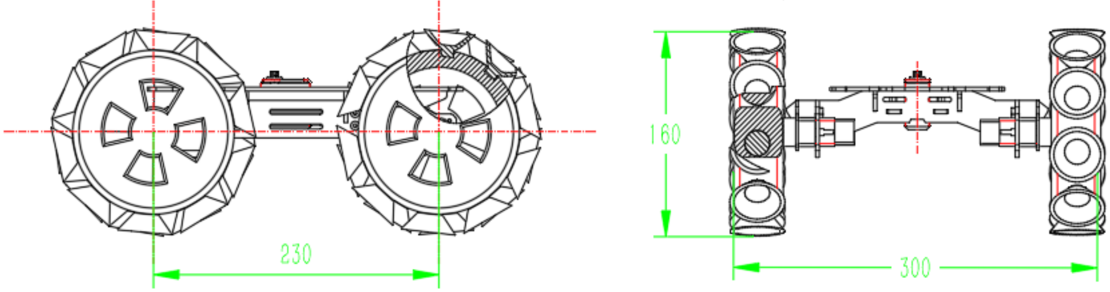

Fig. 14. Moving mechanism partially assembled

2D Drawing of the Cleaning Mechanism

AutoCAD2020 was used to draw a two-dimensional drawing of the cleaning mechanism with dimensions of 205 mm × 40 mm × 40 mm as shown in Figure 15. The cleaning mechanism is driven by a DC motor, which drives the connected steel wire rope to rotate the bristles at high speed to achieve the purpose of cleaning the inner wall of the air duct.

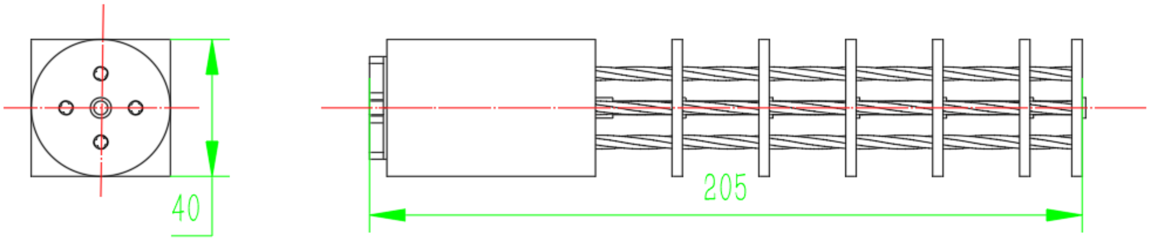

Fig. 15. Cleaning mechanism partially assembled

2D Drawing of a Solar Installation

AutoCAD 2020 was utilized to draw a two-dimensional drawing of the solar device with dimensions of 150 mm × 112 mm × 152 mm, as shown in Figure 16.

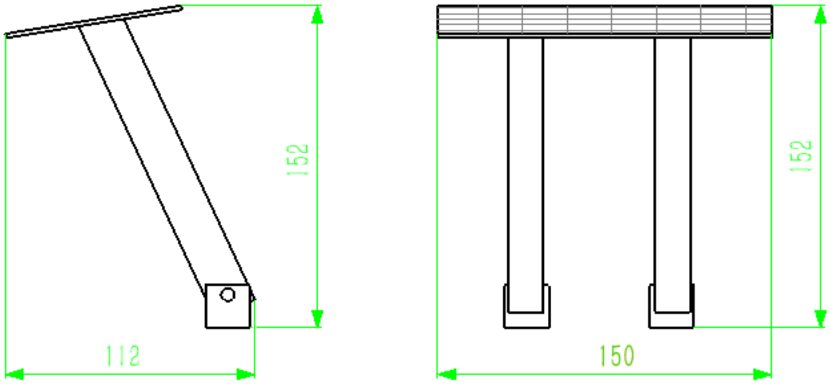

Fig. 16. Partial Installation Diagram of Solar System

General Assembly Drawing of Cleaning Robot

AutoCAD 2020 was used to draw the two-dimensional assembly drawing of the cleaning robot, with an overall dimension of 562 mm × 296 mm × 427 mm, as shown in Figure 17. The overall cleaning robot is composed of four main parts: the mobile plate, cleaning plate, camera, support plate and arm connection plate. The plate thickness is basically 2mm or 3mm, and the material is No. 45 steel. The cleaning mechanism is MC nylon bristles, and the camera device is a CCD camera device. Before working, adjust the height of the camera to have the best working field. Then, driven by the mobile device, the cleaning robot moves forward, and the high-speed rotating cleaning brush is used to clean the central air-conditioning vertical ventilation ducts with a size range of 400mm wide and a height range of 500 mm to 800 mm.

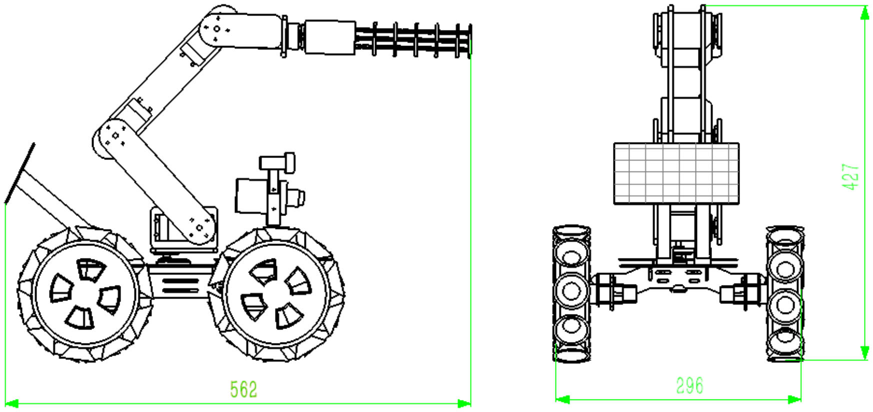

Fig. 17. General assembly diagram of cleaning robot

3D Parts Modeling

Suction Cup

The suction cup part was modeled using SolidWorks 2021 and the modeling result is shown in Figure 18.

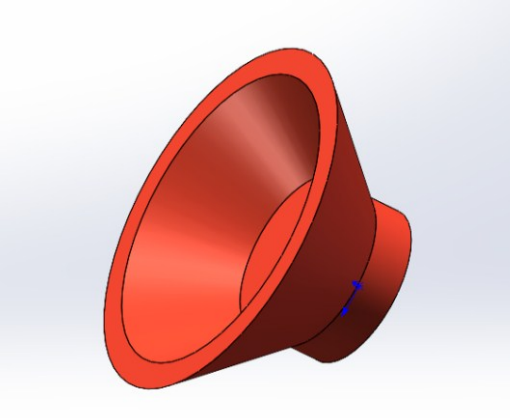

Fig. 18. 3D model of suction cup parts

Wheel Modeling

The wheel part was modeled using SolidWorks 2021 and the modeling result is shown in Figure 19.

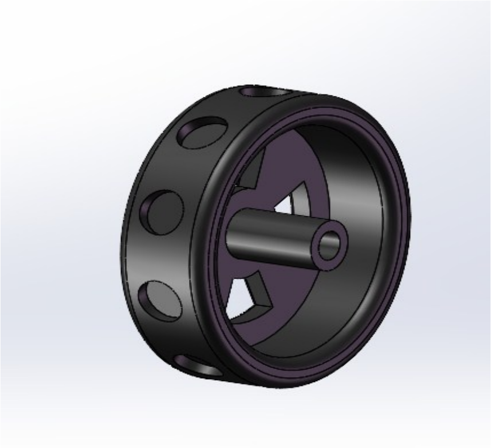

Fig. 19. 3D model of wheel parts

Cleaning Mechanism Wire Rope Modeling

The cleaning mechanism wire rope was modeled using SolidWorks 2021 and the result is shown in Figure 20.

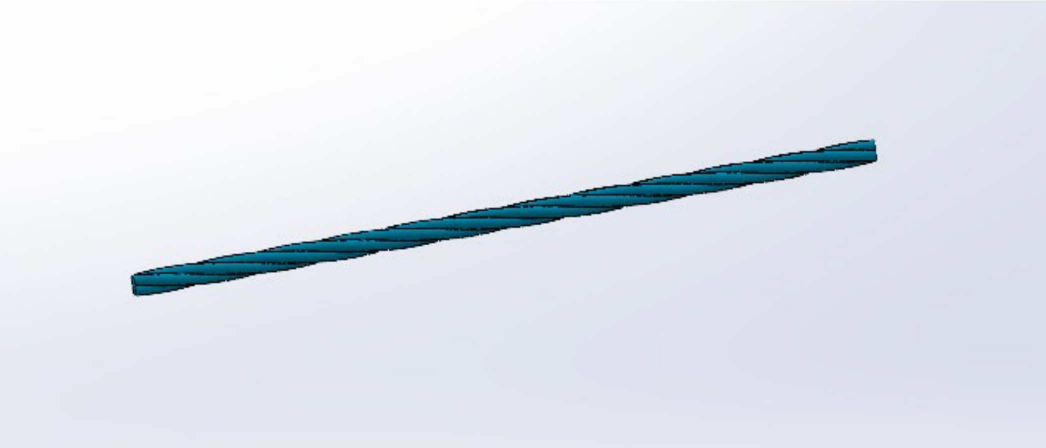

Fig. 20. 3D model of a wire rope

Assembly Drawing of Moving Mechanism

The moving mechanism was assembled using SolidWorks 2021 and the results are shown in Figure 21.

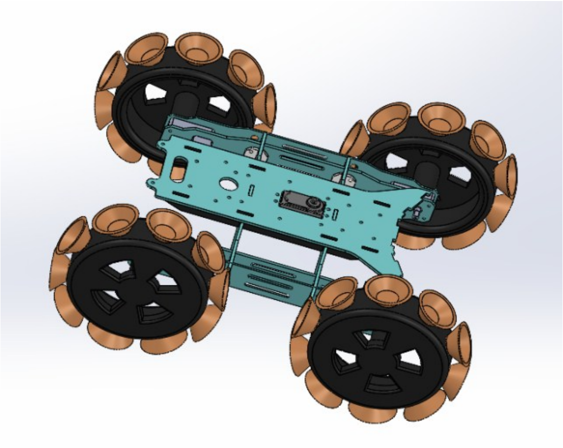

Fig. 21. Mobile mechanism assembly drawing

Cleaning Mechanism Assembly Diagram

The cleaning mechanism was assembled using SolidWorks 2021 and the results are shown in Figure 22.

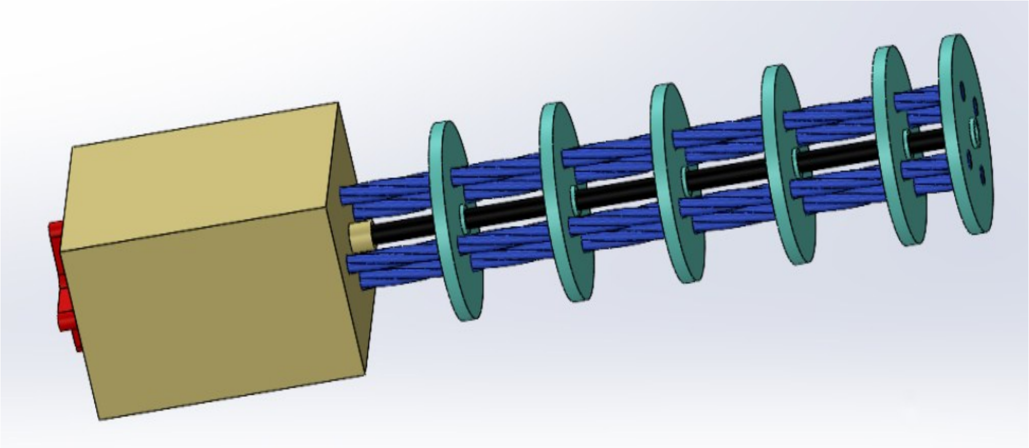

Fig. 22. General assembly drawing of the cleaning mechanism

Camera Lighting Unit Assembly Diagram

The camera lighting unit was assembled using SolidWorks 2021 and the results are shown in Figure 23.

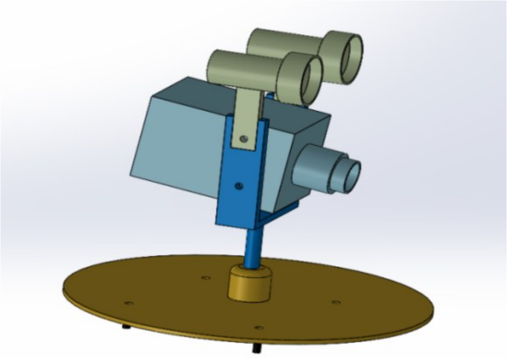

Fig. 23. Camera lighting unit general assembly drawing

Solar Unit Assembly Diagram

The solar unit was assembled using SolidWorks 2021 and the results are shown in Figure 24.

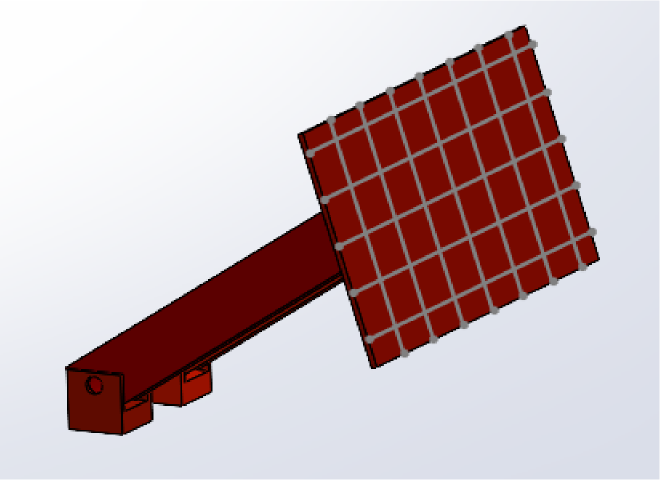

Fig. 24. Solar Unit Assembly Diagram

General Assembly Diagram of Vertical Duct Cleaning Robot

Using SolidWorks 2021, the moving, cleaning, camera parts and solar unit were assembled, resulting in an overall assembly drawing of the cleaning robot (Figure 25)

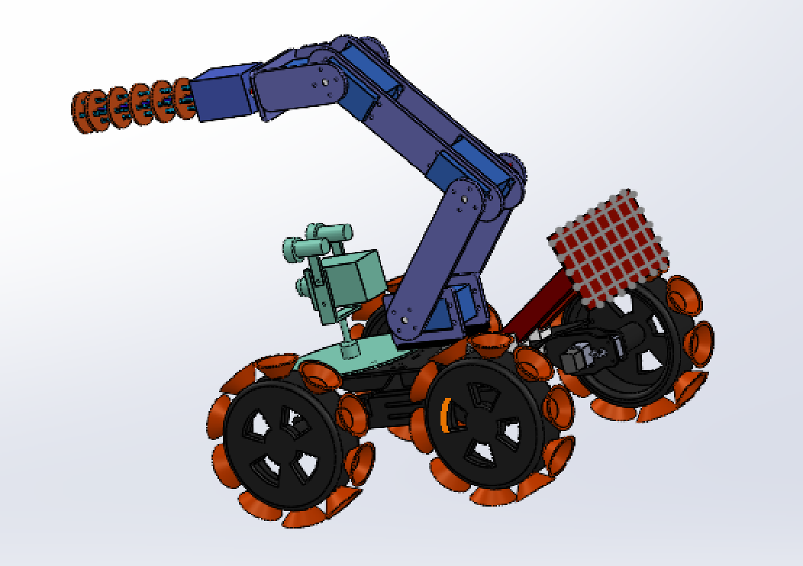

Fig. 25. General assembly drawing of cleaning robot

CONCLUSIONS

This paper mainly carries out the selection of driving mode and the calculation of driving motor types for the cleaning mechanism and the moving mechanism, and selects 63 W, 24 V and 30 W, 24 V DC motors, respectively. The cleaning brush type and the camera lighting device type are selected as MC nylon brush and CCD camera device respectively, and a three-dimensional configuration diagram of the solar device is attached. Finally, the dimensions of each part of the cleaning robot are determined according to the range of vertical ducts to be cleaned. AutoCAD 2020 was used to draw the 2D drawings and assembly drawings of the important components, while SolidWorks 2021 was used for 3D modeling and assembly of the designed vertical duct cleaning robot.

Based on the literature, the following suggestions are made for future research on cleaning robots: 1. The current cleaning robots need to be further optimized in terms of obstacle avoidance ability and adaptability to the cleaning environment. 2. The current cleaning robot cleaning method is too single, need to be optimized accordingly. 3. The control system of the cleaning robot still needs to be developed.

CONFLICTS OF INTEREST

The author declares that there is no conflict of interests regarding the publication of this paper.

REFERENCES

[1] Sawadogo, W., Abiodun, B. J., & Okogbue, E. C. (2020). Impacts of global warming on photovoltaic power generation over West Africa. *Renewable Energy, 151*, 263-277. doi: https://doi.org/10.1016/j.renene.2019.11.032

[2] Baloch, M. H., Tahir Chauhdary, S., Ishak, D., Kaloi, G. S., Nadeem, M. H., Wattoo, W. A., Younas, T., & Hamid, H. T. (2019). Hybrid energy sources status of Pakistan: An optimal technical proposal to solve the power crises issues. *Energy Strategy Reviews, 24*, 132-153. doi: https://doi.org/10.1016/j.esr.2019.02.001

[3] Gorjian, S., Minaei, S., MalehMirchegini, L., Trommsdorff, M., & Shamshiri, R. R. (2020). Chapter 7 - Applications of solar PV systems in agricultural automation and robotics. In S. Gorjian & A. Shukla (Eds.), *Photovoltaic Solar Energy Conversion* (pp. 191-235): Academic Press

[4] Ahmed, S., Zenan, A. H., & Rahman, M. (2014). *A two-seater light-weight solar powered clean car: Preliminary design and economic analysis.* Paper presented at the 2014 3rd International Conference on the Developments in Renewable Energy Technology (ICDRET). doi: https://doi.org/10.1109/ICDRET.2014.6861646

[5] Alhammad, Y. A., & Al-Azzawi, W. F. (2015, 8-10 Dec. 2015). *Exploitation the waste energy in hybrid cars to improve the efficiency of solar cell panel as an auxiliary power supply.* Paper presented at the 2015 10th International Symposium on Mechatronics and its Applications (ISMA). doi: https://doi.org/10.1109/ISMA.2015.7373466

[6] Tang, J., Ye, B., Lu, Q., Wang, D., & Li, J. (2013). Economic Analysis of Photovoltaic Electricity Supply for an Electric Vehicle Fleet in Shenzhen, China. *International Journal of Sustainable Transportation,* 8(3), 202–224. doi: https://doi.org/10.1080/15568318.2012.665980.

[7] Selin, I. A. (2023). New methods for efficient energy management of a solar vehicle on a fixed route. *Информатика, телекоммуникации и управление*, *16*(4), 18-27. doi: https://doi.org/10.18721/JCSTCS.16402

[8] Yao, Y., & Chen, J. (2010). Global optimization of a central air-conditioning system using decomposition–coordination method. *Energy and Buildings, 42*(5), 570-583. doi: https://doi.org/10.1016/j.enbuild.2009.10.027

[9] Absar Alam, M., Kumar, R., Yadav, A. S., Arya, R. K., & Singh, V. P. (2023). Recent developments trends in HVAC (heating, ventilation, and air-conditioning) systems: A comprehensive review. *Materials Today: Proceedings*. doi: https://doi.org/10.1016/j.matpr.2023.01.357

[10] Dai, M., Li, H., & Wang, S. (2023). A reinforcement learning-enabled iterative learning control strategy of air-conditioning systems for building energy saving by shortening the morning start period. *Applied Energy, 334*, 120650. doi: https://doi.org/10.1016/j.apenergy.2023.120650

[11] Ismail, M., Zahra, W. K., & Hassan, H. (2023). Numerical investigation of the air conditioning system performance assisted with energy storage of capsulated concave/convex phase change material. *Journal of Energy Storage, 68*, 107651. doi: https://doi.org/10.1016/j.est.2023.107651

[12] Wang, Y., & Zhang, J. (2006, 6-9 Aug. 2006). *Autonomous Air Duct Cleaning Robot System.* Paper presented at the 2006 49th IEEE International Midwest Symposium on Circuits and Systems. doi: https://doi.org/10.1109/MWSCAS.2006.382110

[13] Yan, H., Niu, H., Chang, Q., Zhao, P., & He, B. (2024). Study on Dynamic Characteristics of Pipeline Jet Cleaning Robot. *13*(2), 49. doi: https://doi.org/10.3390/act13020049

[14] Li, Y., Ye, S., Cui, R., & Shou, Z. (2024). The Design and Analysis of a Tunnel Retro-Reflective Ring Climbing and Cleaning Robot. *13*(6), 197. doi: https://doi.org/10.3390/act13060197

[15] Li, X. P., Wang, X., & Feng, B. (2021). Modeling and control of a novel facade cleaning robot with four-ducted fan drive. *International Journal of Advanced Robotic Systems, 18(*3), 1729881420985721. doi: https://doi.org/10.1177/1729881420985721

[16] Ballini, A., Di Cosola, M., Saini, R., Benincasa, C., Aiello, E., Marrelli, B., Rajiv Saini, S., Ceruso, F. M., Nocini, R., Topi, S., Bottalico, L., Pettini, F., & Cantore, S. (2021). A Comparison of Manual Nylon Bristle Toothbrushes versus Thermoplastic Elastomer Toothbrushes in Terms of Cleaning Efficacy and the Biological Potential Role on Gingival Health. *11*(16), 7180. doi: https://doi.org/10.3390/app11167180

[17] Duan, K., Suen, C. W. K., & Zou, Z. (2023). Robot morphology evolution for automated HVAC system inspections using graph heuristic search and reinforcement learning. *Automation in Construction, 153*, 104956. doi: https://doi.org/10.1016/j.autcon.2023.104956

CALL FOR PAPERS

Trends in Renewable Energy

ISSN Print: 2376-2136 ISSN online: 2376-2144
http://futureenergysp.com/index.php/tre/

Trends in Renewable Energy (TRE) is an open accessed, peer-reviewed semi-annual journal publishing reviews and research papers in the field of renewable energy technology and science. The aim of this journal is to provide a communication platform that is run exclusively by scientists. This journal publishes original papers including but not limited to the following fields:

- Renewable energy technologies
- Catalysis for energy generation, Green chemistry, Green energy
- Bioenergy: Biofuel, Biomass, Biorefinery, Bioprocessing, Feedstock utilization, Biological waste treatment,
- Energy issues: Energy conservation, Energy delivery, Energy resources, Energy storage, Energy transformation, Smart Grid
- Environmental issues: Environmental impacts, Pollution
- Bioproducts
- Policy, etc.

We publish the following article types: peer-reviewed reviews, mini-reviews, technical notes, short-form research papers, and original research papers.

The article processing charge (APC), also known as a publication fee, is fully waived for the Trends in Renewable Energy.

Call for Editorial Board Members

We are seeking scholars active in a field of renewable energy interested in serving as volunteer Editorial Board Members.

Qualifications

Ph.D. degree in related areas, or Master's degree with a minimum of 5 years of experience. All members must have a strong record of publications or other proofs to show activities in the energy related field.

If you are interested in serving on the editorial board, please email CV to editor@futureenergysp.com.